7-19-2023

High Resolution Intracavity Laser Absorption Spectroscopy of Transition Metal-containing Diatomic Molecules

Kristin Bales
University of Missouri-St. Louis, knbp77@mail.umsl.edu

High Resolution Intracavity Laser Absorption Spectroscopy of Transition Metal-containing Diatomic Molecules

Kristin N. Bales

M.S. Chemistry, University of Missouri - St. Louis, 2020
B.S. Chemistry, University of Missouri - St. Louis, 2017
A.A. Chemistry, Mineral Area College, 2015
B.S. Equestrian Science, William Woods University, 2008

A Dissertation Submitted to The Graduate School at the
University of Missouri - St. Louis
in partial fulfillment of the requirements for the degree
Doctor of Philosophy in Chemistry
with an emphasis in
Physical Chemistry

August 2023

Advisory Committee

James J. O'Brien, Ph.D.
Chairperson

Leah C. O'Brien, Ph.D. (SIUE)

Cynthia M. Dupureur, Ph.D.

Lynda M. McDowell, Ph.D.

Abstract

Three transition metal-containing diatomic molecules have been studied using intracavity laser spectroscopy. Many of the transitions were recorded using a Fourier-transform spectrometer for detection, allowing collection at Doppler-limited resolution for the gas phase molecules. Several vibrational bands in two electronic transition systems of tantalum fluoride (TaF) have been analyzed, and new molecular constants provided. Transitions involving six electronic states of tungsten sulfide (WS) have been analyzed, with new and updated constants provided, including a deperturbation analysis of three vibrational bands in two of the states. Finally, a fresh perspective on two electronic states of tungsten oxide (WO) included a deperturbation analysis to support decades of speculation regarding the nature of the two interacting states.

Acknowledgements

I would like to first thank my family who have been so incredibly supportive throughout the completion of my graduate program and even attended my dissertation defense. Thanks to my mom for always being willing to lend an ear and provide encouragement when the (figurative) road was bumpy, and thanks to my dad for always fixing my car when he (literal) road to UMSL contained too many potholes. Special thanks also go to Nate, who kept me fed when I was too focused on work to consider attending to my own sustenance.

Next, I must thank my dissertation committee: Jim and Leah O'Brien for the countless hours spent teaching me to be a spectroscopist and guidance through the research, Lynda McDowell for being a wonderful mentor and friend since my first semester at UMSL, and Cindy Dupureur for first showing me what it takes to do publishable research during my undergraduate work. I will also include here Jack Harms, who was unable to complete his duties as a committee member, but was nonetheless a major contributor to this work through first showing me the ropes on the ILS system and giving me my first introduction to spectral analysis and PGOPHER.

Finally, thanks to UMSL, SIUE, and the NSF for funding this research.

Table of Contents

List of Figures

List of Tables

CHAPTER 1:
INTRODUCTION TO MOLECULAR SPECTROSCOPY

1.1 Absorption Spectroscopy

1.1.1 Introduction to Quantum Mechanics

The purpose of molecular spectroscopy is to study the interaction between light and matter as a means to gain a deeper understanding of the physical characteristics of the target molecule. A photon of a given wavelength has a specific amount of energy, and that photon can only be absorbed by a molecule if the molecule can attain a new stable state by acquiring exactly the amount of energy in the photon needed to make the transition. The move to a new energy level may involve a change in the configuration of electrons within molecular orbitals, a change in vibrational energy, a change in rotational energy, or all three, with changes in electron configuration requiring the most energy, and changes in rotational energy requiring the least, as illustrated in Figure 1.1. In a diatomic molecule, two atoms are connected by a bond that rhythmically stretches, with an increase in vibrational energy causing an increase in magnitude of the stretch. Similarly, an increase in rotational energy causes the two connected atoms to rotate around one another more quickly. These motions of vibration and rotation are illustrated in Figure 1.2.

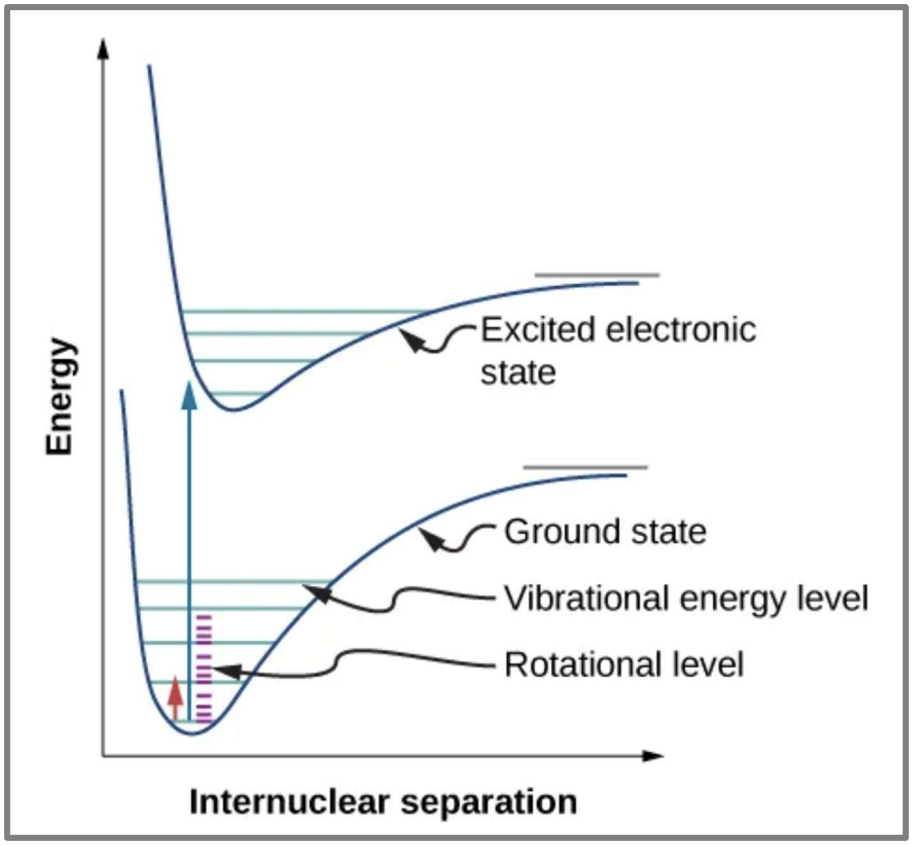

Figure 1.1: Energy level diagram depicting the relative magnitudes of electronic, vibrational, and rotational energy levels. Reprinted from Ref [1]. (CC BY 4.0; OpenStax)

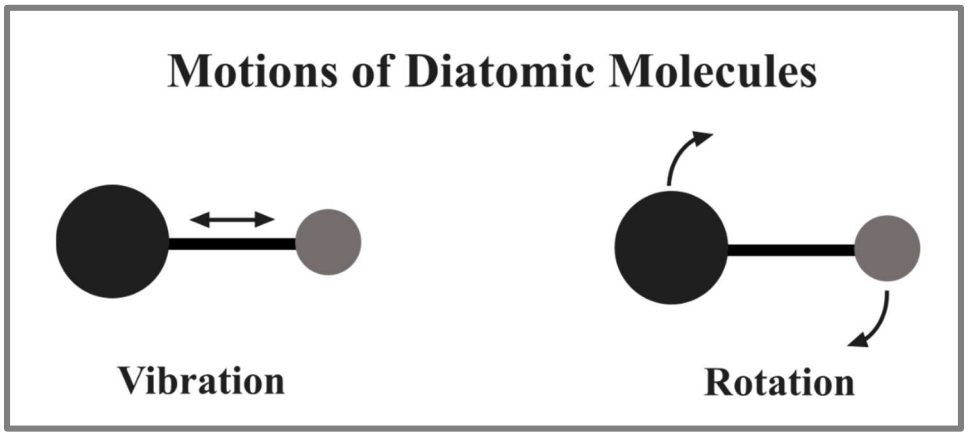

Figure 1.2: Vibrational and rotational motions of diatomic molecules.

The absorption spectroscopy method employed in this work (discussed in detail in Chapter 2) is governed by Beer's Law, given as Equation 1.1.

$$A = -\log_{10}\left(\frac{I}{I_0}\right) = \varepsilon bc \tag{1.1}$$

Here, absorbance, A, is defined as the negative log of the intensity of light transmitted through the sample, I, divided by the intensity of incident light upon the sample, I_0. It is proportional to an absorption coefficient, ε, specific to the molecule and wavelength, the pathlength, b, and concentration, c, of the sample through which the light travels. The experimentally obtained absorption spectra fall in the visible and near-infrared region, shown in Figure 1.3, and correspond to electronic transitions comprised of multiple vibrational bands, which can be further resolved to the detail of their rotational lines.

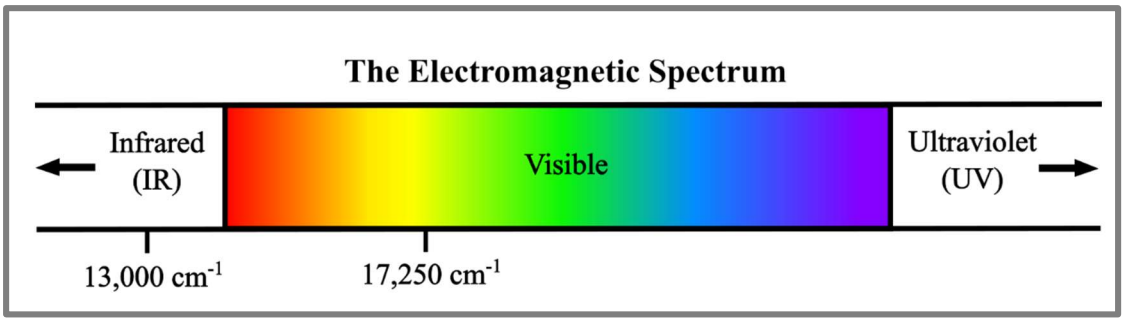

Figure 1.3: The electromagnetic spectrum. Absorption spectra within this work lie in the indicated region of 13,000 cm^{-1} – 17,250 cm^{-1}.

The simplicity of the diatomic molecules which are the focus of this study limits the degrees of freedom available for rotation and vibration, as they have only one stretching vibration and, by symmetry, one mode of rotation, as shown above in Figure 1.2. This results in spectra that are simpler and easier to analyze than those of larger and more complex molecules. The observed spectral lines must be interpreted using

quantum mechanical models for the electronic, rotational, and vibrational energy levels. The use of quantum mechanics is required due to the dual wave-particle nature of light and matter, and a wavefunction, Ψ, is used in quantum mechanics to describe a system as a wave. The total energy of the molecule is given through the Schrödinger equation in Equation 1.2,[2] where the Hamiltonian operator, $\hat{H}$, is detailed in brackets. Within the brackets, the potential energy is represented by V, and the kinetic energy is given by the first term, where $\hbar$ is Planck's constant divided by 2π and μ is the reduced mass of the molecule, given as Equation 1.3. In Equation 1.3, m_1 and m_2 refer to the masses of each of the two atoms in the molecule.

$$\hat{H}\Psi = \left[-\frac{\hbar^2}{2\mu}\left(\frac{\partial^2}{\partial x^2}+\frac{\partial^2}{\partial y^2}+\frac{\partial^2}{\partial z^2}\right)+V\right]\Psi = E\Psi \tag{1.2}$$

$$\mu = \frac{m_1 m_2}{m_1 + m_2} \tag{1.3}$$

The total energy, E, in Equation 1.2 is a discrete value which must be an eigenvalue of the Hamiltonian operator. Thus, the energy levels are quantized, rather than having a continuous range of allowed values. The specific wavelength of absorption for a spectral line then corresponds to a photon whose energy matches exactly the difference in energy between a lower-energy "ground" state, and a higher-energy "excited" state, and by recording and analyzing spectra with high resolution, these specific, discrete energy levels may be distinguished.

1.1.2 Vibrational Energy

In quantum mechanics, operators are frequently derived from classical mechanical principles. Vibrational energy in a diatomic molecule is approximated using a harmonic oscillator model,[3] where two masses connected by a spring move toward and

away from one another with consistent amplitude and frequency. The potential energy, V, associated with this system is given by Equation 1.4,[3] where k is the force constant, and x is the distance the spring has been stretched or compressed. The Schrödinger equation for this approximation is given by Equation 1.5,[3] and is derived by replacing the potential energy term of the Hamiltonian in Equation 1.2 with the harmonic oscillator model of potential energy from Equation 1.4,[3] and replacing the particle mass, m, with the reduced mass, μ. Solutions to Equation 1.5[2] follow the form in Equation 1.6,[3] in which v is the vibrational quantum number, and ν is the vibrational frequency in Hz.

$$V = \frac{1}{2}kx^2 \tag{1.4}$$

$$\left[-\frac{\hbar^2}{2\mu}\frac{d^2}{dx^2} + \frac{1}{2}kx^2\right]\Psi = E\Psi \tag{1.5}$$

$$E(v) = \frac{h}{2\pi}\sqrt{\frac{k}{\mu}}\left(v + \frac{1}{2}\right) = h\nu\left(v + \frac{1}{2}\right) \tag{1.6}$$

Frequently, in the field of spectroscopy, the vibrational frequency is expressed in the unit of wavenumbers, cm^{-1}, obtained by dividing the frequency by the speed of light, c. In this case, the vibrational frequency is denoted by ω_e, and values for vibrational frequency provided within this work are given in this form.

While the harmonic oscillator model provides a reasonable estimate of the vibrational energy of a molecule, particularly for small values of x, the vibrating molecule is actually anharmonic.[2] In an anharmonic oscillation, the potential energy does not increase equally with positive and negative deviations from the equilibrium

internuclear distance. As the bond is compressed, repulsion between the two positively charged nuclei results in a sharper increase in potential energy with decreasing bond length than would be expected from a harmonic oscillator. As the bond is stretched, the restoring force decreases until the bond is broken. The anharmonic potential energy curves are illustrated above in Figure 1.1 as the blue curves representing the excited and ground electronic states. The energy of a given vibrational level, G(v), is modeled by the Taylor series shown in Equation 1.7.[4]

$$G(v) = \omega_e\left(v+\frac{1}{2}\right) - \omega_e x_e\left(v+\frac{1}{2}\right)^2 + \omega_e y_e\left(v+\frac{1}{2}\right)^3 + \cdots \quad (1.7)$$

Here, $\omega_e x_e$ and $\omega_e y_e$ are anharmonicity constants used to correct for the electrostatic interaction of the two atoms, and $\omega_e y_e$ should be much smaller than $\omega_e x_e$, which should be much smaller than ω_e in a well-modeled system.

A spectroscopic transition between two specific vibrational levels is referred to as a vibrational band. Vibrational bands are designated using the notation (v′,v″), where v′ is the excited state vibrational level, and v″ is the ground state vibrational level.[2] For example, a (1,0) vibrational band denotes a transition between a ground state v = 0 and an excited state v = 1.

1.1.3 Rotational Energy

Much like vibrational energy, the rotational energy of a molecule is estimated by applying a classical mechanical model: the rigid rotor. The rigid rotor consists of two masses separated by a fixed distance as opposed to the stretchable spring of the harmonic oscillator, and its kinetic energy can be expressed as shown in Equation 1.8,[3] where r is the bond length and ω is the angular velocity. Solving the kinetic energy

portion of the Schrödinger equation for rotation, since potential energy in this model is 0, gives the eigenvalues expressed in Equation 1.9,[4] in terms of the rotational quantum number, J. The rotational energy value from Equation 1.9 is again converted from units of Joules to wavenumbers to give the rotational constant, B, in Equation 1.10,[4] in the form which will be used throughout this work.

$$E = \frac{1}{2}\mu r^2 \omega^2 \tag{1.8}$$

$$E = \frac{h^2}{8\pi^2 \mu r^2} J(J+1) \tag{1.9}$$

$$B = \frac{h^2}{8\pi^2 c \mu r^2} \tag{1.10}$$

Again, the classical model only provides an approximation to the total rotational energy, this time due to the non-rigid nature of the molecular bond. As the rotational energy increases, r increases, leading to a reduction in the effective value of B with larger values of J. Rotational energy, F(J), can be thus expressed using Equation 1.11.[4] Here, D is the centrifugal distortion constant which corrects for the change in apparent B value due to stretching of the molecular bond at higher rotational energies. The magnitude of D is estimated by the Kratzer relationship,[2] provided as Equation 1.12.

$$F(J) = BJ(J+1) - D[J(J+1)]^2 + \cdots \tag{1.11}$$

$$D = \frac{4B^3}{{\omega_e}^2} \tag{1.12}$$

As with the Taylor series used to describe the vibrational energy, the magnitude of D should be much smaller than B, with higher order rotational terms continuing to decrease sharply in magnitude.

Rotational levels are observed spectroscopically as a series of related absorption lines called branches. Transitions between two states follow the selection rule $\Delta J = 0$, or $\Delta J = \pm 1$.[2] A transition from a given lower state J, noted as J″, must go to an excited state J, noted as J′, of the same J, J+1, or J–1. Lines with $\Delta J = 0$ are referred to as the Q-branch, while lines with $\Delta J = +1$ comprise the R-branch, and those with $\Delta J = -1$ form the P-branch. Lines within the branches are identified according to their branch letter, with the lower state J in parenthesis. For example, R(20) would be the absorption line between J″ = 20 and J′ = 21, and P(20) would suggest J″ = 20 and J′ = 19. The rotational branch structure can be used to verify that two vibrational bands share a common upper or lower state through the method of combination differences. As illustrated in Figure 1.4, a pair of lines, R(J–1) and P(J+1) share a common upper state, with J′ = J. The difference in energy between the two lines is due to the energy difference between J″ = J–1 and J″ = J+1. This energy difference is termed $\Delta_2F''(J)$. A similar comparison can be made between lines R(J) and P(J) to obtain $\Delta_2F'(J)$ for the upper state. If the Δ_2F'' values for two vibrational bands match within experimental error, the two bands share a ground state, and matching Δ_2F' levels would confirm a shared excited state.[2]

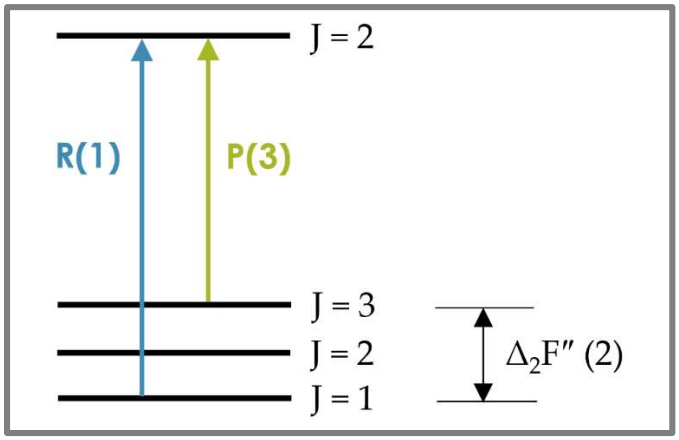

Figure 1.4: Illustration of the energy difference, Δ_2F'', for two rotational lines which share a common upper state J′=2. Matching Δ_2F'' values between two vibrational bands indicates a shared lower vibrational level via the method of combination differences.

The pattern of rotational branches within a spectrum may be more easily visualized using a Fortrat diagram, as shown in Figure 1.5, where the wavenumber positions of rotational lines are plotted on the x-axis against J″ on the Y-axis. In the example diagram, the origin of the vibrational band lies near 16,030 cm^{-1}, with the R-branch first extending to higher energy before turning back to lower energy, and the P-branch extending to lower energy. This branch structure is common for spectra of metal-containing diatomics. The turning toward lower energy of the R-branch occurs when the lower electronic state of the transition has a smaller B value than the upper state, and results in the appearance of a red-degraded bandhead.[2] The bandhead appears as a portion of greater absorbance where several R-branch lines overlap, and remaining transition lines for the band continue “to the red” or to lower energy.

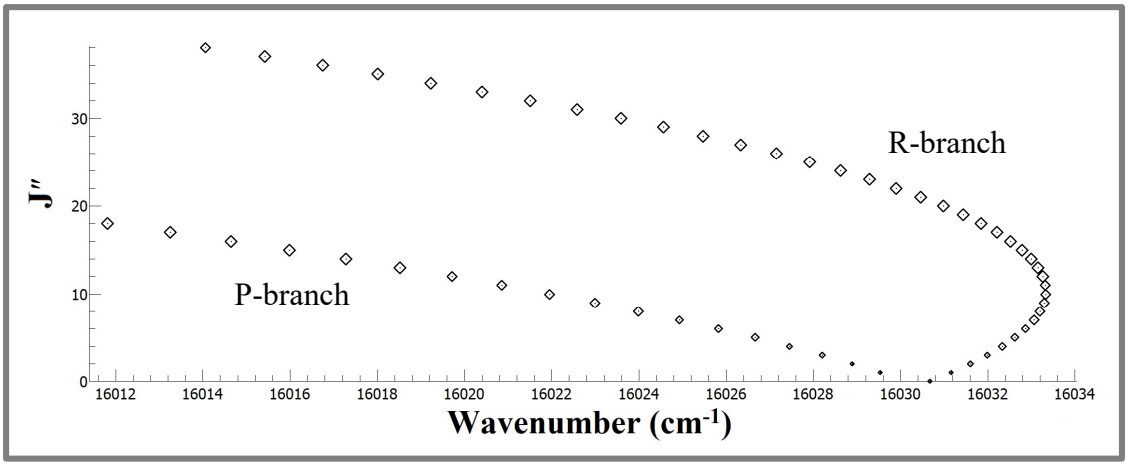

Figure 1.5: Example Fortrat diagram illustrating rotational branch structure as J″ vs. Wavenumber (cm^{-1}).

1.2 The Dunham Model and Mass Dependence

The rotational energy coefficients discussed in the previous section are dependent on bond length, as shown above in Equations 1.10 and 1.12. In addition, the potential energy of a diatomic molecule is anharmonic, so increases in vibrational energy bring about an increase in bond length. Thus, rotational constants will vary among vibrational energy levels. Rotational and vibrational constants are also both dependent on the reduced mass of the molecule. Atoms which have multiple abundant isotopes, which differ by the number of neutrons in the nucleus, and thus mass, can form molecules with multiple isotopologues which are identical in structure, but vary in isotopic composition. These isotopologues will also have slightly different rotational and vibrational parameters due to the dependence on reduced mass. In 1932, J. L. Dunham[5] provided a model to describe the dependence and merge the rotational and vibrational parameters into one equation, given as Equation 1.13.

$$E(v,J) = \sum_{l,m} Y_{l,m}\left(v+\frac{1}{2}\right)^{l}[J(J+1)]^{m} \tag{1.13}$$

Here, the total energy, E, is in terms of both the vibrational quantum number, v, and the rotational quantum number, J. The subscripts *l* and *m* refer to the power of the vibrational quantum number and the rotational quantum number, respectively, such that in comparison with Equation 1.7, $Y_{10} \approx \omega_e$ and $Y_{20} \approx \omega_e x_e$, and from Equation 1.11, $Y_{01} \approx B$ and $Y_{02} \approx D$.

It also has been shown in sections 1.1.2 and 1.1.3 that both the rotation and vibration of a molecule are influenced by the molecule's reduced mass such that the mass difference caused by inclusion of different isotopes of a species will in turn affect both the rotational and vibrational coefficients. Dunham[5] proposed the following mass correction to the $Y_{l,m}$ terms:

$$Y_{l,m}^{i} = Y_{l,m}^{p}\left(\frac{\mu_p}{\mu_i}\right)^{\frac{l}{2}+m} \tag{1.14}$$

where the superscripts *i* and *p* refer to the individual isotopologue and the primary isotopologue, respectively.

1.3 Electronic States and Transition Notation

The largest and vastly more complicated component to the overall energy of a molecule is the electronic energy. The electronic energy cannot be described with a simple model from classical mechanics, as can the vibrational and rotational portions, as it is a result of a complex combination of electron-electron interactions, placement of electrons in molecular orbitals of various energy levels, and the spin of unpaired

electrons. Understanding of molecular orbitals comes from early quantum mechanical models of the energy levels of the Bohr atom, which give atomic orbitals.[3] Linear combinations of the atomic orbitals then give rise to the molecular orbitals which are relevant to the spectroscopy of diatomic molecules. Within this work, a set of quantum numbers is used to describe different electronic states of the molecules, including the electronic orbital angular momentum, L, the axial component of the precession of L, Λ, the electron spin, S, and the axial component of the precession of S, Σ. The total angular momentum is J, and the axial component of the total angular momentum, Ω, is equal to $\Lambda+\Sigma$.[2]

In a dynamic molecule, rotational, vibrational, and electronic motions interact. Interactions between rotational and vibrational motions were discussed in the previous section. Rotational and electronic motions similarly influence one another. Hund's five coupling cases describe the different modes of coupling and are labeled as case (a), (b), (c), (d), or (e).[2] Cases (a) and (c) are the two which are relevant to this work. Hund's case (a) arises in electronic states where the electronic motion interacts weakly with rotational motion, but is strongly coupled to the internuclear axis. The good quantum numbers in Hund's case (a) are Λ, S, Σ, J and Ω.[4] In case (c), L and S interact in very strong spin-orbit coupling, and result in mixing of the wavefunctions of closely packed electronic states of similar Ω. Here, only J and Ω are good quantum numbers. Case (c) arises frequently in heavy molecules, and a case (c) model is used for fitting the electronic states of the transition metal-containing species in this work. The notation for a case (c) state is [X.X]Ω, where the number in brackets is the energy of the state in 10^3 cm^{-1}. When Ω=0, a superscript + or – gives the symmetry of the state, as either

$[X.X]0^+$ or $[X.X]0^-$. While no electronic states are fit using Hund's case (a) within this work, it is common for the ground state of a species to be given in the case (a) notation of $^{2S+1}\Lambda(\Omega)$ when a case (c) model is otherwise appropriate. With the $^{2S+1}\Lambda$ notation, the value of the quantum number Λ for the state is given by a capital Greek letter, where $\Lambda=0$ is given by Σ, $\Lambda=1$ is given by Π, and so on. Taking the example which will be frequently seen in later chapters, $^3\Sigma^-(0^+)$ and $^3\Sigma^-(1)$ are two components of the ground state which is primarily $^3\Sigma^-$ ($S=1$, $\Lambda=0$) in character, with spin-spin coupling which results in one component having $\Omega=0^+$ symmetry, while the other has $\Omega=1$ symmetry.

1.4 Matrix Elements and Perturbations

Because the wave equations for the electronic states of heavy diatomic molecules are extremely complex, they are typically solved using a diagonalized matrix representation with some interactions neglected. Additional off-diagonal matrix elements can then be added to the base representation as needed to include neglected interactions and obtain a more accurate result. For example, consider a $^1\Pi$ state and the Hund's case (a) basis set, $|n\Lambda S\Sigma J\Omega\rangle$, where n represents all neglected quantum numbers not considered in the Hund's coupling scheme. Since for $^1\Pi$, $S=0$ and $\Omega = \Lambda\pm\Sigma$, we can exclude S and Σ from being specified and write the Hamiltonian matrix as shown in Table 1.1. Here, the off-diagonal matrix elements, q and q_D, in the upper right quadrant, split the state into two components designated by + for *e*-levels with parity $+(-1)^J$ and – for *f*-levels with parity $-(-1)^J$.[4]

Table 1.1: Hamiltonian matrix for a $^1\Pi$ state, showing Λ-doubling via the parameters q and q_D.

	$\|J, \Lambda = -1, \Omega = -1\rangle$	$\|J, \Lambda = +1, \Omega = +1\rangle$
$\|J, \Lambda = -1, \Omega = -1\rangle$	B[J(J+1)] +D[-J^2(J+1)^2]	q[±J(J+1)/2] +q_D[±J^2(J+1)^2/2
$\|J, \Lambda = +1, \Omega = +1\rangle$		B[J(J+1)] +D[-J^2(J+1)^2]

This type of representation becomes important in the discussion of perturbations between two electronic states, a prominent topic in this work, as these perturbations are modeled using appropriate matrix elements to couple the two discrete electronic states involved.

There are two main categories of perturbations: homogeneous, between two states with ΔΩ=0, and heterogeneous, between states with ΔΩ=1.[6] In both cases, the interaction causes the energy levels of the two states to repel one another such that the state with greater energy is pushed to higher energy than would be expected for an unperturbed state, while the opposite is true for the lower energy state. Heterogeneous perturbations, ΔΩ=±1, are J-dependent,[7] with the magnitude of the interaction increasing sharply for J where the energy levels of the two states are close, and thus called rotational perturbations.[6] They produce a localized effect within a spectrum, as shown by the energy level diagram in Figure 1.6. The heterogeneous perturbation operator of relevance to this work is the L-uncoupling operator, J^+L^-, with the selection rules ΔΩ=±1 and ΔΛ=±1, and ΔΣ=ΔS=0. The matrix element which couples the two electronic states is $\langle J,\Lambda=0,\Omega=0|J^+L^-|J,\Lambda=1,\Omega=1\rangle = \sqrt{J(J+1)}$.

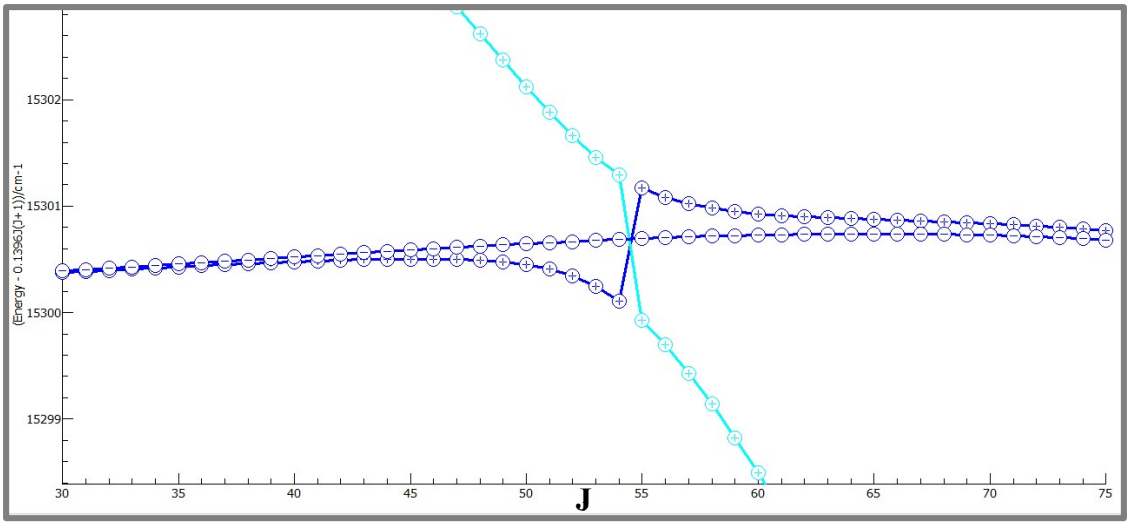

Figure 1.6: Reduced energy level diagram illustrating the effects of a heterogeneous perturbation. Subtracted from the energy on the y-axis is an approximate BJ(J+1) to facilitate easier viewing. The nearly straight dark blue trace marked with (-) represents unperturbed energy levels for the state represented by dark blue. The pale blue represents the perturbing state's energy levels, pushing the dark blue energy levels to lower energy before the levels cross near J=55, and to higher energy at higher J.

Homogeneous perturbation interactions, on the other hand, have a fairly consistent magnitude with increasing J and are called vibrational perturbations since the entire vibrational level is displaced.[2] The homogeneous perturbation follows the selection rules $\Delta\Omega=\Delta\Lambda=\Delta\Sigma=\Delta S=0$. Here, the matrix element is given by $\langle J,\Lambda=1,\Omega=1 \,||\, J,\Lambda=1,\Omega=1\rangle = 1$ for an interaction between two states with $\Lambda=1$ and $\Omega=1$. For both types of interactions, a deperturbation analysis can be used to model the perturbation interaction and determine the characteristics each involved state would have had if the perturbation interaction were not present.

1.5 Fitting with PGOPHER

The publicly available software program, PGOPHER,[8] was used for the rotational and deperturbation analyses of all spectra in this work, as well as some spectra

processing applications including wavenumber calibration using the Calibrate function, and baseline correction and conversion of transmission spectra to absorbance via options in the Baseline/Peaks window. In some cases, multiple vibrational bands were fit in the conventional manner, where line positions for rotational branches input into the software and fit parameters such as Origin, B, and D were determined on a band-by-band basis with each vibrational band and each isotopologue fit independently. In analyses involving multiple vibrational levels of an electronic state, enabling a Dunham[5]-type fit, a constrained variables approach introduced by Breier and colleagues[9] was used. In this method, the Dunham parameters are added to PGOPHER[8] as variables which are related to the PGOPHER[8] fitting parameters through constraints programmed into the input file. The mass relationship in Equation 1.14 is also programmed into the PGOPHER[8] input file to ensure appropriate mass scaling of the Dunham[5] parameters among isotopologues. In a similar way, other analyses which did not incorporate sufficient vibrational levels for a Dunham[5] model to be instructive were also mass-constrained, with the PGOPHER[8] fit parameters for multiple isotopologues directly constrained to expected mass relationships. Details regarding specific fitting methods will be given in each relevant chapter.

1.6 Intracavity Laser Absorption Spectroscopy (ILS)

First introduced in the 1970s,[10] Intracavity Laser Absorption Spectroscopy (ILS) is one of the most sensitive spectroscopic techniques, allowing detection of species in relatively low concentration or with low absorption coefficients.[11] O'Brien *et al.* determined absorption coefficients for methane below 0.1 km^{-1} am^{-1}.[12] Given the

approximation of 1 am (amagat) being equal to 44.6 mol/m^3,[13] the given absorption coefficient in a more widely familiar unit would be roughly 2×10^{-6} M^{-1} cm^{-1}. This high degree of sensitivity is obtained through the introduction of a target molecular species within the resonance cavity of a laser, which provides two advantages. Light which passes through the gaseous target species within the cavity is subject to absorption by that species, thus photons corresponding to the absorbed wavelengths are less abundantly available for stimulated emission and amplification. Additionally, a delay between onset of laser initiation and data recording means that as the laser is generated and light is reflected between the mirrors which define the cavity, the light makes many passes through the sample, increasing the effective Beer's Law pathlength in a manner similar to that of a multi-pass cell. Having confirmed in 1982 that the ILS method does follow Beer's Law,[14] Stoeckel, Melieres, and Chenevier later described the effective pathlength, L_{eff}, in an ILS system as given in Equation 1.15:[15]

$$L_{\text{eff}} = \left(\frac{l}{L}\right) ct_g, \tag{1.15}$$

where l refers to the distance the laser travels in a single pass through the absorbing species and L is the full length of the resonator cavity. As usual, c is the speed of light, and t_g is the generation time of the laser, or the time between laser onset and signal detection. For experiments described within this work, effective pathlength values of 1-2 km are typical. However, L_{eff} of tens of thousands of km have been achieved elsewhere.[11]

The ILS method requires that the spectral width of the laser's emission profile must be significantly larger than the linewidth of the absorber, as described in a review article by Campargue *et al*.[16] and illustrated in Figure 1.7. Because the profile intensity

of the laser converges toward a central wavelength position with increasing t_g,[17] becoming very narrow with continuous operation, intermittent interruption of the pump beam is required to periodically bring the system below the lasing threshold and re-initiate the cycle. The effect of t_g on the laser profile is illustrated in Figure 1.8. Also shown is the increase in absorptivity observed with larger t_g which results from an increase in L_{eff}. The entire ILS system used for the experiments described in this work has been detailed in the literature previously,[18-20] and a brief overview is provided in following sections.

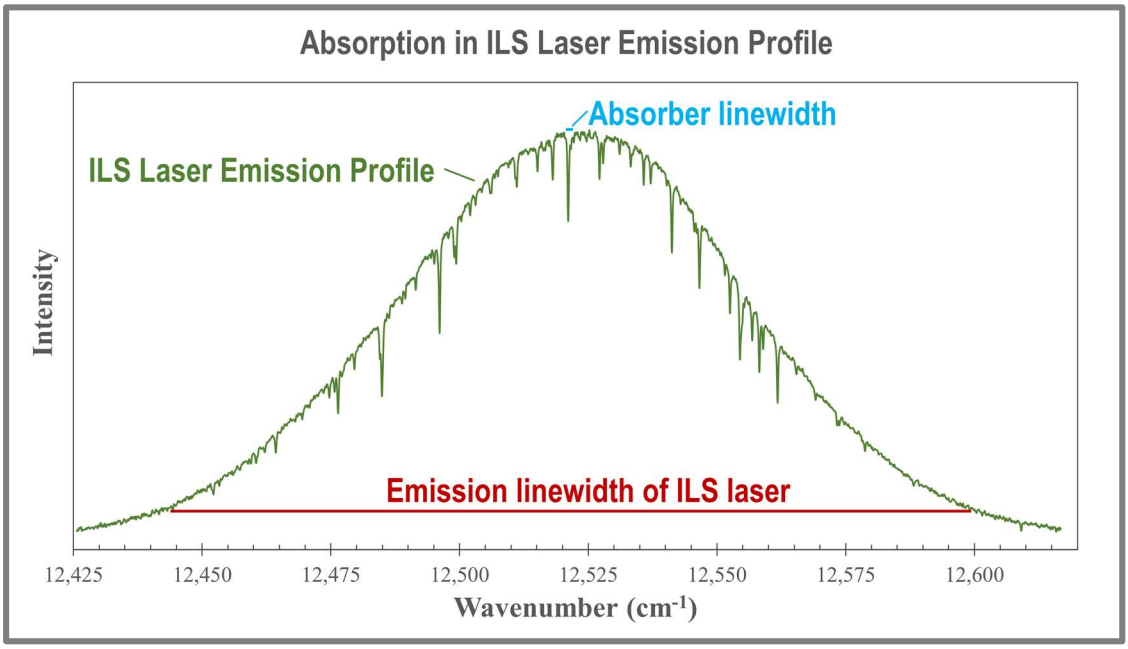

Figure 1.7: Absorption within the emission profile of an ILS laser.

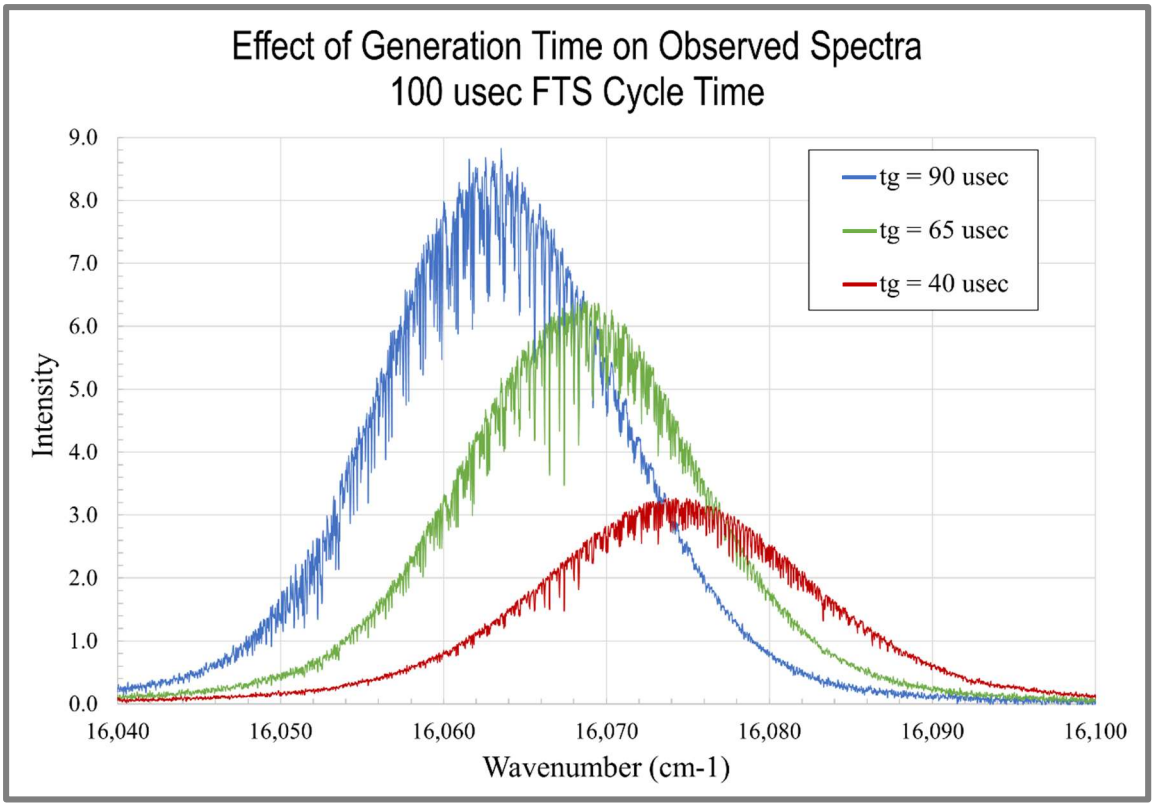

Figure 1.8: The effect of generation time on observed spectra. Decreasing t_g results in a less intense, but more broadband, laser output. A decrease in spectral line intensity is also observed with a decrease in t_g.

1.6.1 Previous Work with the ILS Method

Although the complexities involved in setting up an ILS system have resulted in relatively low use of the technique, the five decades since the first introduction of the theory of the approach[10] have provided a fair base of understanding for the challenges, benefits, and limitations of the ILS method. As noted previously, early experimental works verified the applicability of Beer's Law to ILS measurements,[14] but also investigated limitations in sensitivity of ILS measurements due to variations in t_g and pump power,[21] and detailed workable solutions to such problems as the introduction of noise by interference fringes.[22] Several review articles also have detailed technical aspects of the use of the method and suggested further applications for its use.[11,16,23] A

paper presented by Brink[24] in 1981 pointed out the suitability of the method for use in molecular spectroscopy using a plasma discharge for creation of target molecules, and described an experimental setup similar to that used for recent studies of metal-containing small molecules in the O'Brien lab group.

Works within the group have described vibrational levels within electronic states of nickel chloride (NiCl),[25] germanium hydride (GeH), [26] copper hydroxide (CuOH),[27] and copper oxide (CuO).[28] The analysis of CuO by J. Harms marked the beginning of the use, within the group, of a mass-independent Dunham model to analyze diatomic molecules with multiple abundant isotopologues. The aim of using this type of analysis was to investigate the deviation from expected mass relationships in the Dunham[5] parameters caused by breakdown of the Born-Oppenheimer approximation,[4] which assumes that due to the much greater mass of the nucleus in comparison to electrons, the motion of electrons can be decoupled from that of the nucleus. Also investigated using this method were field-shift effects, which are changes in electronic energy due to differences in the size and mass of different isotopes, and which vary based on the degree of electron density at the nucleus. These field shift effects were described in a number of works by Tiemann *et al.* [29-33] and were combined into a comprehensive Dunham[5] model presented by Le Roy in 1999.[34] The work on Born-Oppenheimer breakdown (BOB) and field-shift effects by J. Harms was continued with spectral analyses involving platinum fluoride (PtF),[35] platinum sulfide (PtS),[20,36] and platinum chloride (PtCl).[37] The final paper on PtCl also investigated periodic trends among bonding in NiF, NiCl, PtF, and PtCl. Because of the small relative magnitude of BOB parameters and field-shift effects, the final work on PtS[20] was aided by the enhanced

resolution offered by incorporation of a Fourier-transform spectrometer for detection of spectra, which will be discussed in section 2.5.

1.7 Purpose of the Work

The level of specificity offered by the rotational analysis of the high-resolution spectra of gas-phase diatomic molecules is of great value to computational chemists. The parameters determined through this work can also be used to calculate bond length (r_e), through the rotational constant, B, as well as vibrational frequency, $\omega_e x_e$. Computational works[20,38,39] often seek to predict the magnitudes of these types of parameters. Due to the complex electronic structure of transition metals and molecules that contain them, these species are inherently difficult to model, and calculations rely on many assumptions to simplify the equations and reduce computing time. The high accuracy and precision of the experimental data provided by the type of work detailed in the following chapters provide an excellent benchmark that allows these assumptions to be verified and improved upon.

In addition to the benefits to computational chemists, analysis of these types of molecules aids in understanding molecular bonding, and how a specific metal bonds with different types of ligands. This type of data can be instructive regarding electronic and catalytic uses of related bulk materials.

CHAPTER 2:
EXPERIMENTAL METHODS

2.1 ILS Systems and Laser Tuning

The spectra recorded for this work were collected using two ILS systems which are based on two different gain media, whose emitted light is amplified to form the ILS laser. The use of various gain media in ILS systems have been previously studied and reported in the literature, including the fluorescent dye[14,15] and titanium-doped sapphire[40] configurations used in experiments described in this work. The dye laser system (DL-ILS) operates in the visible region, and the titanium-doped sapphire (TS-ILS) system operates in the near infrared. In both cases, the gain medium is pumped by a Coherent® Verdi™ V-10 laser with an operating wavelength of 532 nm. Mirrors are used to direct the pump beam toward the gain medium within the resonator cavity of the desired system. Other extra-cavity portions of both systems are identical and will be described in later sections.

The DL-ILS system can be used with a multitude of laser dyes. In these experiments, the dyes DCM and Rhodamine-6G (R6G) were used to obtain spectral coverage across the region of roughly 14,500 – 17,250 cm^{-1} (690 – 580 nm). The spectral output of the dye laser is controlled by rotation as well as vertical and horizontal translation of an optical tuning wedge located within the resonator cavity.

The TS-ILS system operates from approximately 12,000 – 14,000 cm^{-1} (830 – 715 nm) and is tuned by passing the beam through two Brewster angle prisms located within the resonator cavity to horizontally disperse the light by wavelength. A movable

slit is then used to select the desired wavelength by allowing only the wavelengths that are able to pass through the slit to be transmitted and amplified.

2.2 ILS Laser Cycle

Both the DL-ILS and TS-ILS systems operate in a time-modulated manner to maintain the required broadband laser profile and to allow selection of the generation time (t_g). Initiation of the laser sequence occurs when the first of two acousto-optic modulators (AOM1) is switched off, directing the Verdi V-10 pump beam into the gain medium. At the end of a cycle, AOM1 switches on, ending the laser cycle by diverting the pump beam away from the gain medium and causing the medium to fall below the lasing threshold. In this way, the laser profile is unable to converge to a narrow output band, allowing observation of spectral lines over a wide range of wavelengths. A second AOM (AOM2) diverts the beam into the detector at a user-specified time interval after initiation of the cycle by AOM1. The length of time between cycle initiation by AOM1 and the beginning of data collection upon activation of AOM2 is the generation time, t_g. Before AOM1 switches off at the end of the laser cycle, AOM2 likewise switches off to end the detector's viewing window. Control of the AOM timing sequence is handled by a pulse-and-delay generator, with which settings for the laser cycle time, laser gate (t_g plus viewing window), t_g, and viewing window can be selected. The entire process is monitored via a photodiode and oscilloscope to ensure appropriate timing is maintained. An illustration of a typical oscilloscope reading of the photodiode signal is given as Figure 2.1.

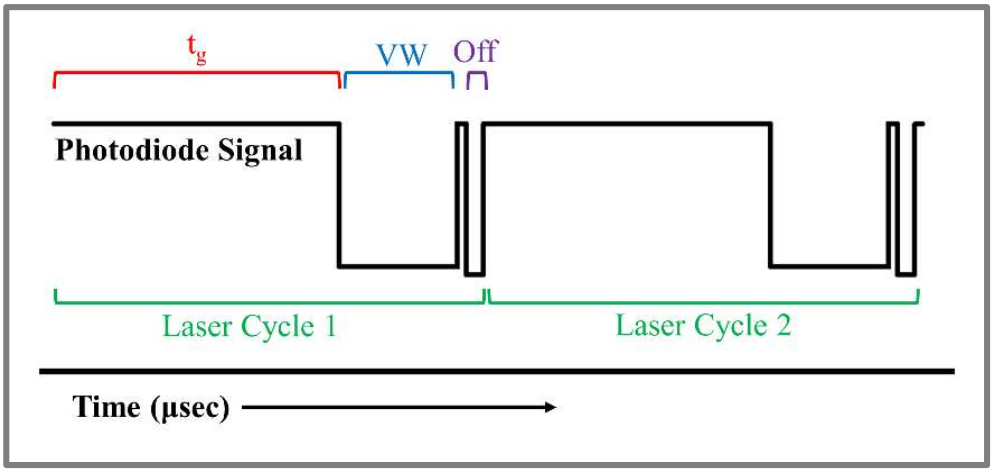

Figure 2.1: Timing sequence of the ILS method. Two laser cycles are depicted as a photodiode signal, where initiation of the cycle and t_g (red) is triggered by AOM1 switching on, the viewing window (VW, blue) is triggered by AOM2, and the beginning of the laser off period (purple), occurs when AOM1 switches off.

2.3 Dispersed ILS

The original ILS system (Dispersed ILS) incorporates a 2 m McPherson customized Model 2062 monochromator and 1024 channel EG&G diode array detector capable of recording data with a maximum resolution of ~0.035 cm^{-1}. Transmission spectra are recorded via the OMA88 software program, then processed to remove background interference and calibrated to achieve a more accurate wavenumber position for each line and is accomplished using the iodine reference spectra provided by Salami and Ross.[41] For each experimental spectrum collected, a corresponding background and iodine spectrum (via extra-cavity I_2 cell) also are collected. A dark current baseline is captured by blocking the ILS laser from entering the monochromator. A Visual Basic program developed in-house by J.J. O'Brien, AYES, is used for initial data processing. The dark current baseline is subtracted from each experimental, background, and iodine spectrum. Following division of the experimental and iodine spectra by the corresponding background, the transmission

spectra are then converted to an absorption format, and the data are exported as a text file. Each iodine spectrum is calibrated to the reference data provided by Salami and Ross[41] using a Visual Basic for Applications (VBA) macro-enabled Excel workbook developed by J. Harms.[42] The workbook, Pseudo-automated Iodine Calibration (PIC), imports data from the text files created by AYES, determines line positions in the ILS iodine spectrum using Savitzky-Golay 1st and 3rd derivatives, and matches the line positions to the reference linelist. The data are then calibrated by fitting to a second order polynomial with Excel's LINEST function. The user visually inspects the displayed experimental and reference iodine spectra and fit residuals, adding or removing lines if needed, and the approved calibration is copied to the corresponding experimental ILS spectrum before the next experimental iodine spectrum in the series is loaded. The estimated wavenumber accuracy for a well-resolved ILS line position calibrated in this manner is ±0.005 cm^{-1}.

Because spectra collected using the Dispersed ILS method are only 5-7 cm^{-1} wide for a given monochromator position, the calibrated experimental spectra are then concatenated into one single spectrum for a given transition band or region of interest to facilitate easier rotational branch assignment and analysis. The concatenation is accomplished using a second VBA macro-enabled Excel workbook.[42] Here, each calibrated plasma spectrum is plotted with the next spectrum in the series so that baseline and intensity adjustments can be made as necessary. The user then selects a point on the spectrum which overlaps smoothly with the next spectrum, and the text files for the two spectra are joined at the selected wavenumber position. The final output is a single absorption spectrum that may span >100 cm^{-1}.

2.4 ILS-FTS

2.4.1 ILS-FTS Overview

In 2019, the ILS system was integrated with a Bruker 125 M Fourier-transform spectrometer for detection (ILS-FTS),[20] increasing resolution capabilities by a full order of magnitude to 0.0035 cm^{-1}. This enhanced capability allows spectra for the transition metal diatomics studied here to be collected at Doppler-limited resolution, allowing for more detailed analyses of species with multiple abundant isotopologues. The resolution enhancement is illustrated in Figure 2.2.

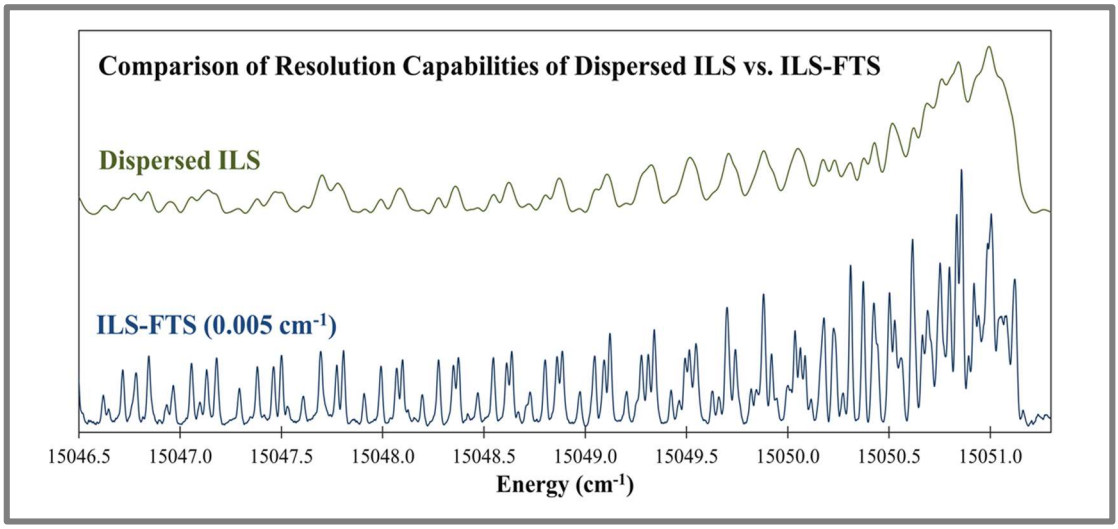

Figure 2.2: Illustration of enhanced resolution offered by ILS-FTS vs. Dispersed ILS with representative spectra for the (0,0) band of the $[15.05]0^{+} - X\ ^{3}\Sigma^{-}(0^{+})$ transition of WS.

An additional benefit of the ILS-FTS method is that the spectrum of the entire ILS laser profile (usually 50 – 100 cm^{-1}) can be collected at once, rather than requiring collection of many smaller portions. When multiple scans are required to collect a full transition band, spectra are added together before dividing by the coadded background spectra using the spectrum calculator function available in the Bruker-provided

software, OPUS. Calibration of the divided ILS-FTS spectra is accomplished using the Calibrate function in PGOPHER[8] with lines observed from atmospheric O_2 and H_2O[43] as well as atomic lines from the sputter gas, Ar,[44,45] within each experimental spectrum. These line positions are well-known and lead to a wavenumber accuracy near 0.0015 cm^{-1} for well-resolved ILS-FTS lines in a calibrated spectrum. When necessary, due to laser profile drift between collection of an experimental and corresponding background spectrum, a baseline correction can be applied in PGOPHER[8] using the Baseline/Peaks window before the transmission spectrum is converted to absorbance. Shown in Figure 2.3 is an experimental spectrum with corresponding background, and the resultant absorbance spectrum post processing.

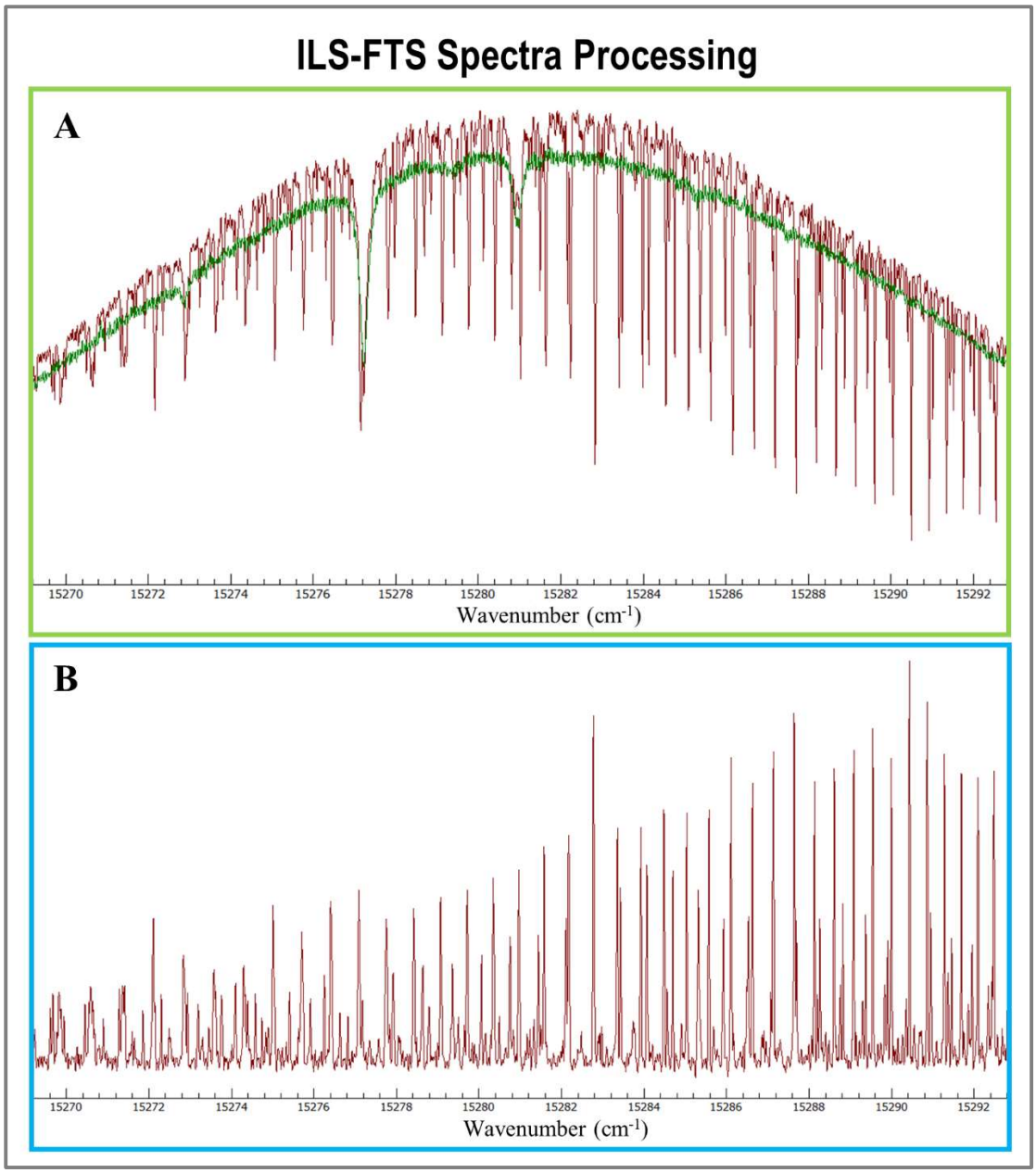

Figure 2.3: Processing of ILS-FTS spectra. (A) Outlined in lime are the overlaid experimental (burgundy) and background (green) transmission spectra. The experimental spectrum shows the laser profile with superimposed absorption. (B) Outlined in blue is the same experimental spectrum following background division and baseline correction.

A full schematic for the DL ILS-FTS system is provided below as Figure 2.4 (A), with panel (B) of the figure detailing the differences in the intracavity portion of the TS ILS-FTS system.

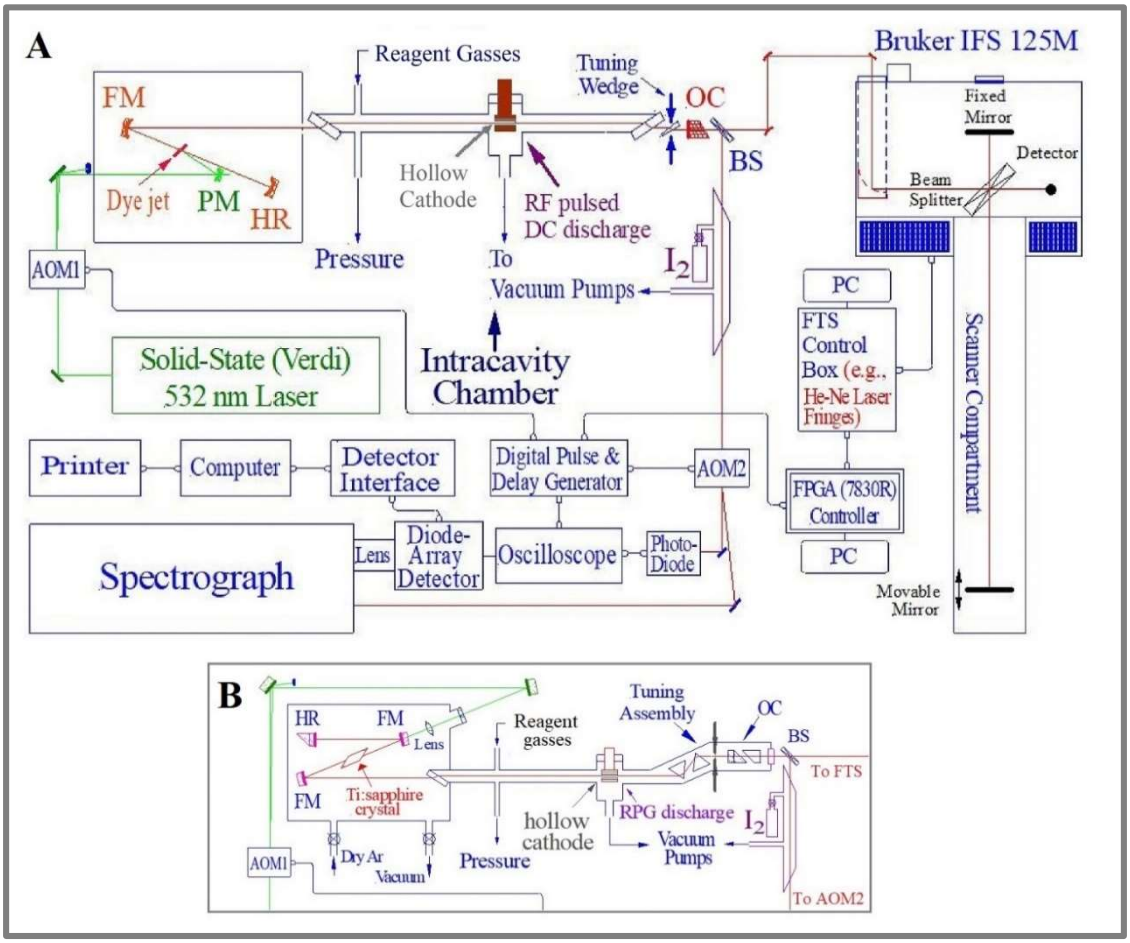

Figure 2.4: Schematic for the ILS-FTS system. (A) Full schematic of DL ILS-FTS system. (B) Intracavity portion of the TS ILS system. Extra-cavity components of both systems are the same.

2.4.2 ILS-FTS Timing and Generation Time

Because both the ILS and FTS methods are time-based, the timing of the two systems are synchronized through the use of a National Instruments Field Programmable Gate Array (FPGA) programmed by J. Harms using LabView software. While updates to the LabView software and timing processes have been recently attempted, a delay in the repair of a key component of the FTS has led to a delay in

troubleshooting and implementation of the new method. Thus, only the LabView programming used for projects within this work will be discussed here. Signal ports on the IFS 125M provide digital impulses for several specific timing events associated with FTS data collection, including XAOUT, which marks the FTS sampling points. These sampling points occur 250 ns after the LASXAF port signals the zero-crossing of the helium-neon (HeNe) laser. The LabView program monitors XAOUT for sampling point signals, and when one is detected, a signal is sent to the pulse-and-delay generator which initiates the ILS cycle via AOM1. The laser gate setting on the pulse-and-delay generator is used to set the time interval before AOM1 again diverts the pump beam away from the lasing medium, and the ILS laser is "off" until a signal from XAOUT begins a new ILS cycle. Because the XAOUT signal is tied to the HeNe zero crossing of the FTS, the ILS cycle time is thus tied to the FTS scan rate. A Triggering Interval option in the LabView program allows selection of an integer value to specify the number of XAOUT signals to be included in a single ILS cycle. For example, selecting a Triggering Interval of 2 would result in AOM1 initiating a new ILS cycle with every second XAOUT signal, doubling the ILS cycle time. The ILS cycle time, T_{ILS}, can be determined by Equation 2.1,

$$T_{ILS} = \frac{1}{Rate_{FTS}} \times \frac{n}{2} \tag{2.1}$$

where $Rate_{FTS}$ is the scan rate in kHz, and n is the set value of the Triggering Interval.

Difficulty arises when attempting to control generation time, t_g, using the integrated system. The strategy initially implemented was to include a timing offset such that the XAOUT sampling point occurred within the ILS cycle at the desired t_g.

Testing of this system proved that sampling does not occur exclusively at the marked sampling points, however, a change in effective t_g can be roughly implemented via the laser gate setting on the pulse-and-delay generator. As previously described, a decrease in t_g is expected to result in a lower maximum ILS laser intensity, broadening of the laser profile, a blue-shift in the central wavenumber of the profile, and decreased absorbance.[14] With a constant FTS scan rate and laser gate setting, the Triggering Interval was adjusted to place the XAOUT signal at various points within the ILS cycle, and an expected t_g was determined using an oscilloscope. Absorbance values were estimated from the resultant spectra as given in Equation 1.1. The oscilloscope readings and spectra of the laser profiles are shown as Figure 2.5. In Figure 2.6, a magnification of the central, highest intensity portion of the overlaid spectra is provided to show in detail the lines used to determine absorbance values. The determined absorbance values are given as Table 2.1. As demonstrated, this method resulted in insignificant change in any of the four metrics which should accompany a change in t_g.

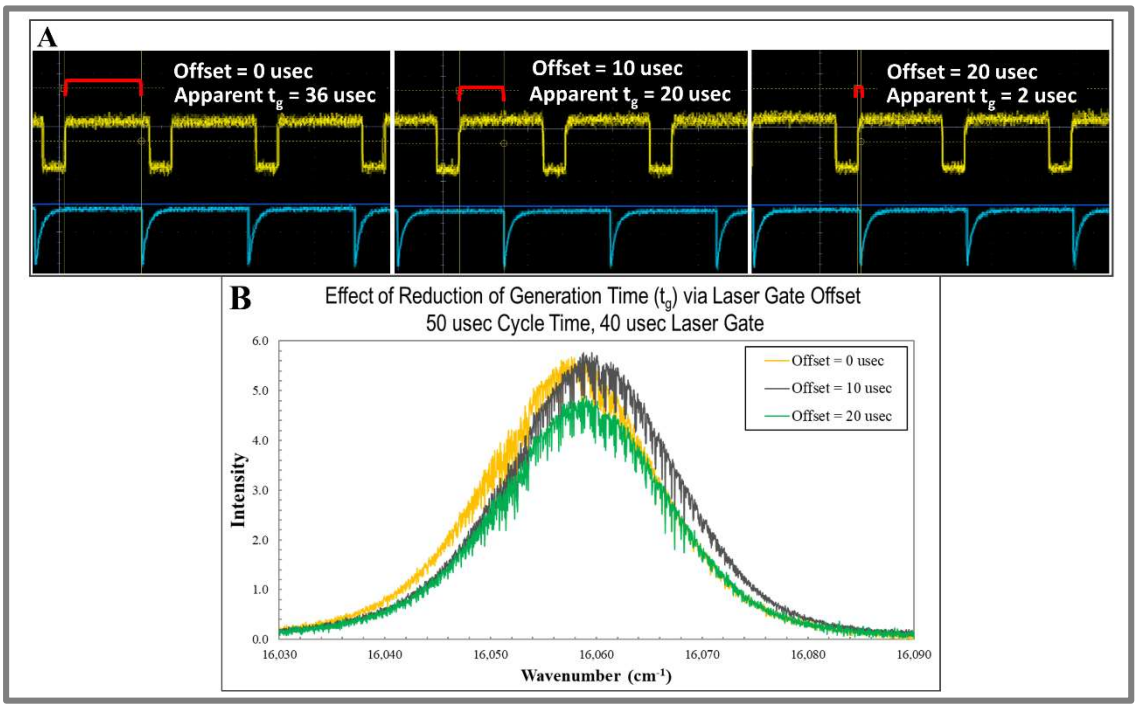

Figure 2.5: Results of the attempt to alter ILS generation time via Laser Gate offset. (A) Oscilloscope readings for each collection indicating the expected t_g. (B) Overlay of the three ILS laser profiles with absorption from CuO, indicating no significant change in intensity or shift in central wavenumber.

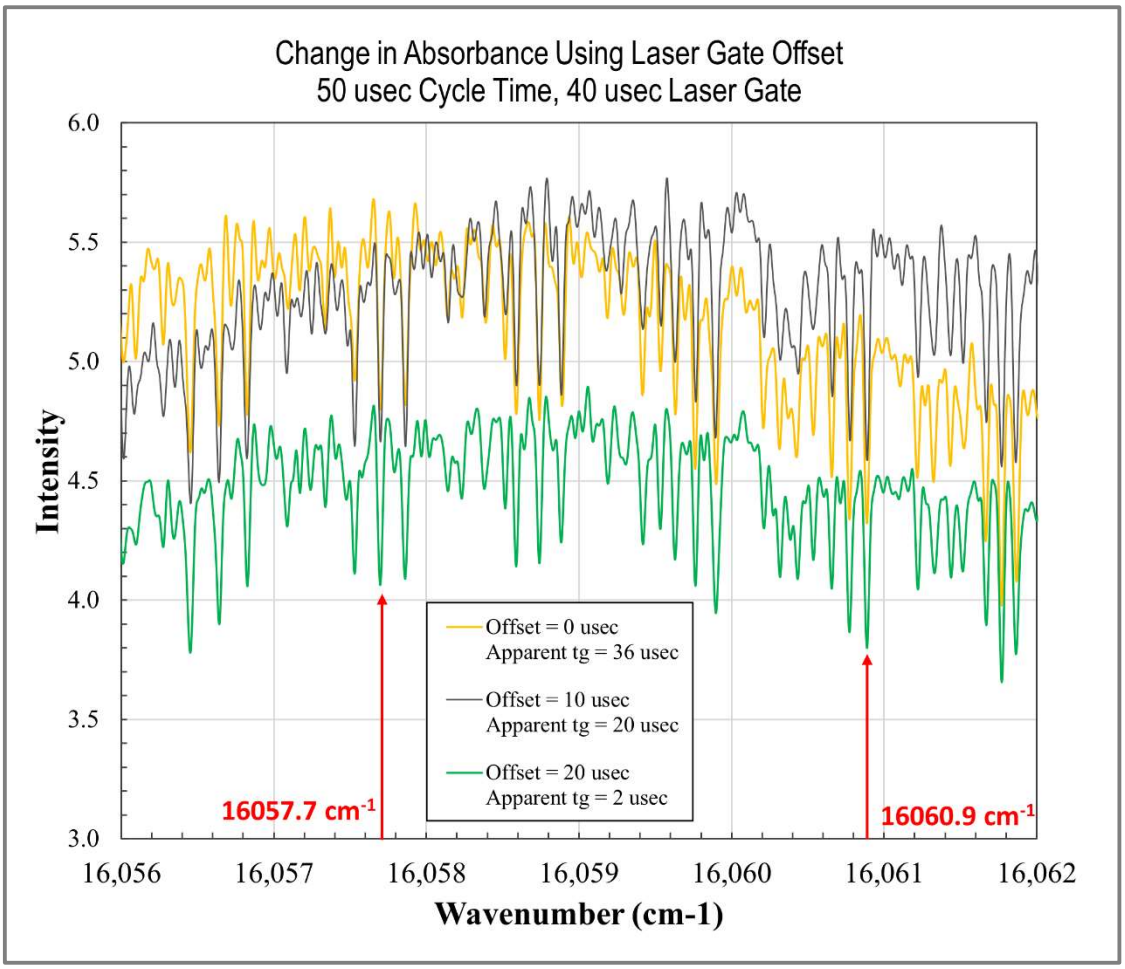

Figure 2.6: Magnification of central portion of Figure 2.5 (B) depicting lines used for measuring the change in absorbance observed when altering ILS generation time via Laser Gate offset. While there is a slight difference in overall intensity among the spectra, this is consistent with typical fluctuations in the instrument from one scan to the next, and calculated absorbance values are not significantly different among the three measurements.

Table 2.1: Calculated absorbance values for two lines in the CuO spectrum for three values of apparent generation time (t_g) adjusted using Laser Gate offset. No significant difference is observed between absorbance values of a given line at different apparent t_g, indicating t_g is not influenced by the Laser Gate offset setting.

Apparent t_g (µsec)	Abs at 16057.7 cm^{-1}	Abs at 16060.9 cm^{-1}
2	0.070	0.075
20	0.067	0.078
36	0.069	0.073

While the initial attempts to adjust t_g using the Laser Gate offset method were unsuccessful, it was determined through these experiments that sampling by the IFS 125M is not a series of finite, discrete occurrences as indicated by the XAOUT sampling point signals. A different approach was then taken: making adjustments to the apparent t_g using the Laser Gate setting on the pulse-and-delay generator directly. In this manner, instead of adjusting the temporal location of the data collection within the ILS laser cycle, the maximum t_g is limited by physically ending the "on" portion of the cycle. The efficacy of this method was demonstrated as shown in Figure 2.7 by maintaining a fixed FTS scan rate with no Laser Gate Offset in the LabView program, but different settings for the Laser Gate itself on the pulse-and-delay generator.

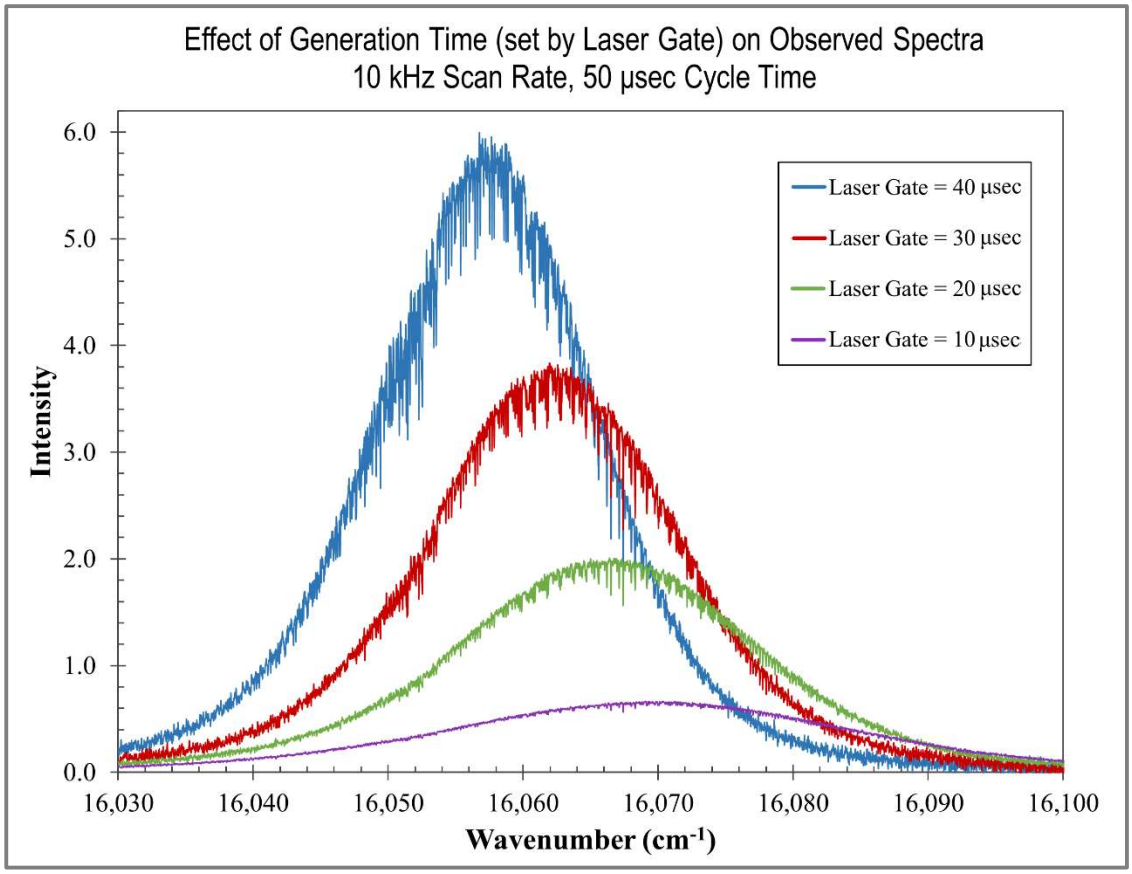

Figure 2.7: Effect of adjustment to Laser Gate setting on apparent generation times in CuO spectra.

Here, we see a significant decrease in overall intensity of the ILS laser profile with reduction in t_g as set by the Laser Gate, along with the characteristic broadening of the profile and shift to higher energy. Absorbance values were again estimated using the lines shown in Figure 2.8, and the calculated values are given in Table 2.2, with the linear regressions of the values depicted in Figure 2.9 (A) and (B).

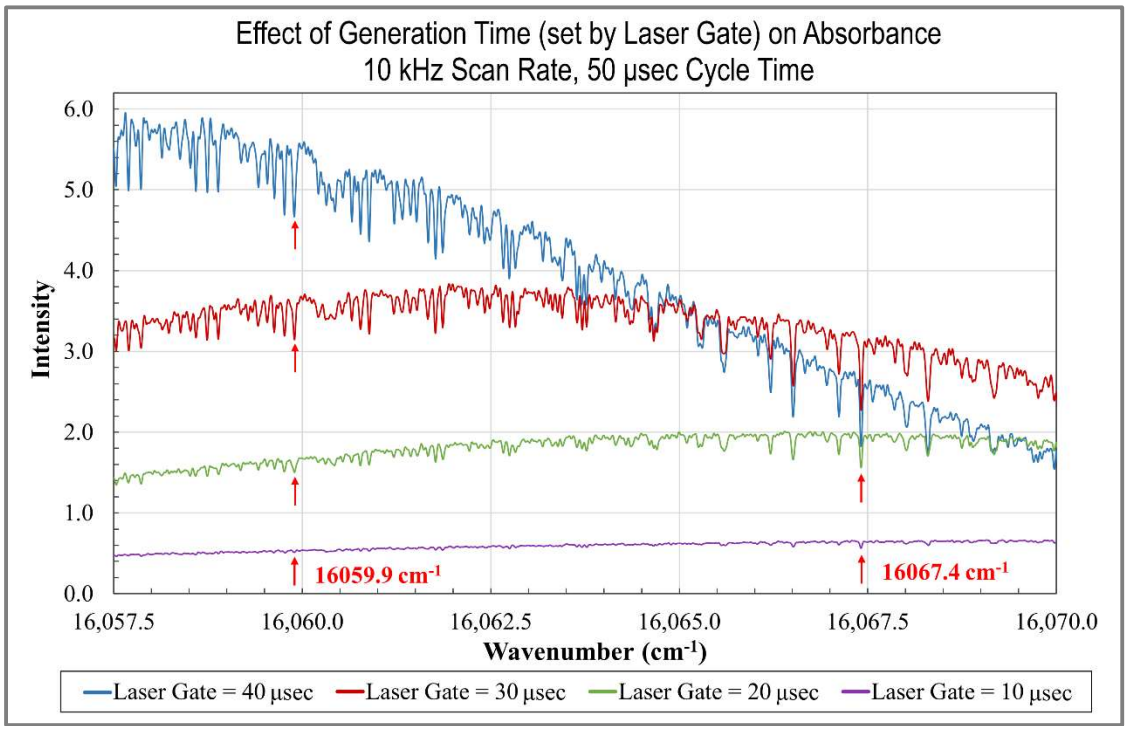

Figure 2.8: Magnification of Figure 2.7 depicting lines used for measuring the change in absorbance observed when generation time is set by the Laser Gate.

Table 2.2: Calculated absorbance values for two lines in the CuO spectrum for four values of generation time (t_g) set by adjusting the Laser Gate on the pulse-and-delay generator. As expected, absorbance values increase with t_g.

Laser Gate t_g (µsec)	Abs at 16059.9 cm^{-1}	Abs at 16067.4 cm^{-1}
10	0.023	0.062
20	0.045	0.101
30	0.064	0.142
40	0.075	0.167

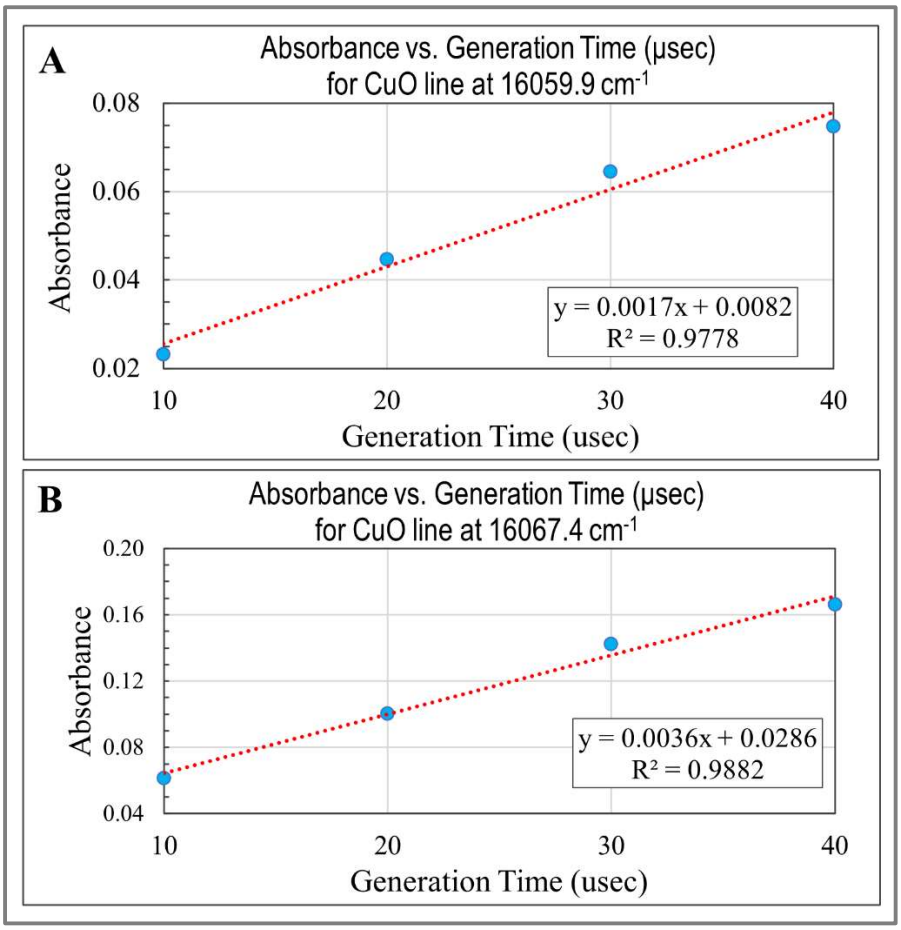

Figure 2.9: Absorbance vs. generation time (μsec) set via the Laser Gate on the pulse-and-delay generator for two lines in the CuO spectrum.

While the determined R^2 values for absorbance vs. t_g shown in Figure 2.9 are not sufficient for a rigorously quantitative method, the use of the Laser Gate setting does have enough of the desired effect on the spectra to be useful for the type of measurements used in this work, as the overall absorption may be increased or decreased to obtain sufficient signal-to-noise without saturating. Also, the analyses presented here are not dependent upon the absorbance values of the spectral lines, but on their wavenumber positions.

2.5 Synthesis of Target Molecules

Gas-phase diatomic molecules containing a transition metal are produced in an evacuated reaction chamber within the laser cavity. Inside the reaction chamber is a copper hollow cathode lined with the transition metal of interest. An RF-pulsed DC current is applied to the cathode, and target species are formed within the resulting plasma discharge. A flow of argon is added to the chamber to serve as a sputter gas, and reagent gas flows are added as necessary, dependent upon the desired target species. All gas flows are regulated via mass flow controllers. For each experiment, conditions must be optimized to the specific target species and electronic transition, with adjustments made to reagent gas composition, reaction chamber pressure, and discharge current. Speed of gas flow through the chamber can be roughly adjusted by increasing or decreasing gas flows and opening or closing the valves leading to the vacuum pumps. Reagent gasses used within this work include hydrogen (H_2), oxygen (O_2), carbon disulfide (CS_2), and sulfur hexafluoride (SF_6). Total pressure within the reaction chamber ranges from 0.5 – 2.0 torr, and discharge currents from 0.30 – 0.80 A were used. Specific details regarding synthesis of target molecules for collection of the various experimental spectra will be given in the chapters associated with each target species.

CHAPTER 3:
TANTALUM FLUORIDE (TaF)

3.1 Introduction to TaF

The electronic structure of tantalum fluoride has not been studied comprehensively, with the only published work on TaF provided by Ng *et al*. in 2017.[38] Laser Induced Fluorescence (LIF) in a molecular beam was used to examine 22 vibrational bands in seven electronic transitions in the visible region from 18,000–23,000 cm^{-1}. Molecular constants were determined for seven upper states, [18.6]0, [19.8]0, 19.9]0, [22.1]0, [22.9]0, and [18.1]1, and two lower states, X $^3\Sigma^-(0^+)$ and A $^3\Phi_2$. A computational analysis at the MRCISD + Q (internally contracted multi-reference configuration interaction with singles and doubles and Davidson's cluster correction) level of theory of several low-lying Λ-S states also was presented as part of the work. Potential energy curves for these states were shown as well as term energies, equilibrium bond lengths, and vibrational and rotational constants. Additionally, transition dipole moments were presented indicating the strength of various electronic transitions. In this work, we observed and analyzed eight additional bands belonging to two new electronic transitions of TaF, specifically the (1,0), (0,0), and (0,1) vibrational bands of the [16.0]0^+ – X $^3\Sigma^-$ (0^+) transition and the (2,1), (1,0), (0,0), (0,1), and (1,2) bands of the [16.3]1 – X $^3\Sigma^-$ (0^+) transition. The transitions were observed using intracavity laser spectroscopy (ILS), and the measured line positions were fit using PGOPHER[8] to obtain molecular constants, which are presented here with comparisons to the previous work by Ng *et al.*[38] The observed transitions are illustrated, in addition to those observed previously, in Figure 3.1. While our determined molecular constants

agree with those calculated, the observed $[16.0]0^+ - X(0^+)$ transition was predicted to have a very low transition dipole moment[38] and was expected to be weak. The results of the work described in this chapter have been published in the Journal of Molecular Spectroscopy.[46]

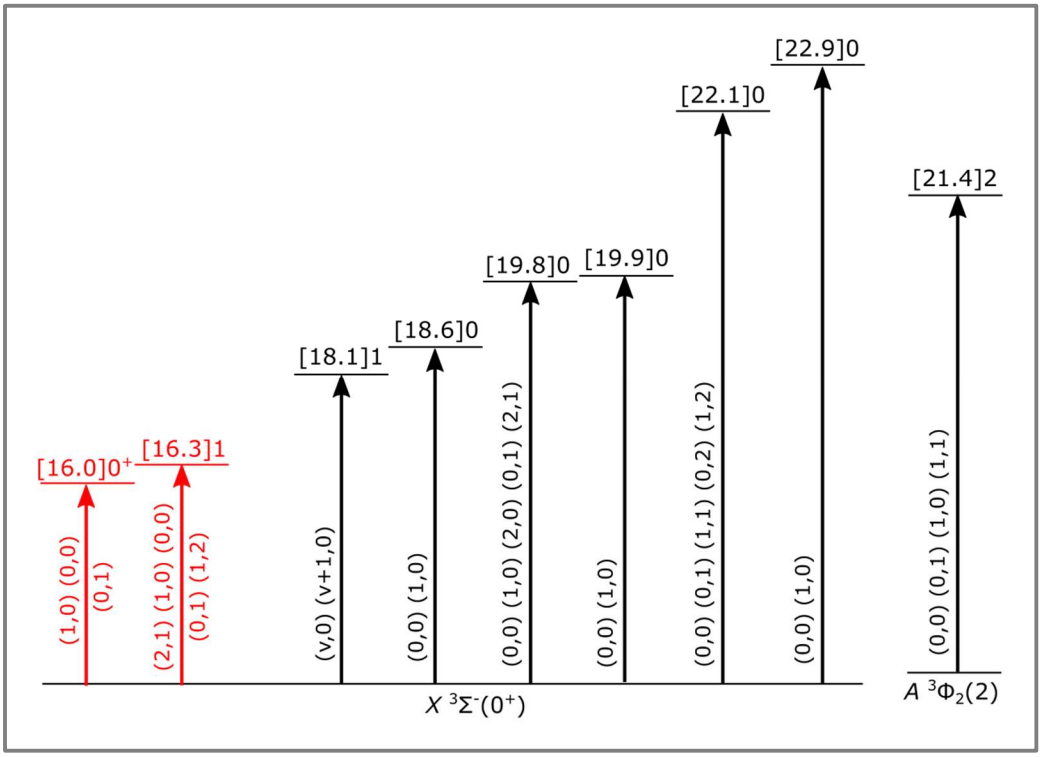

Figure 3.1: Illustration of observed transitions of TaF. The two new electronic transitions observed in this work are shown on the left (red), while the 7 previously described transitions[38] are on the right (black).

3.2 *Experimental Method*

The spectra were collected in the visible region using Dispersed DL-ILS.[18] TaF molecules were produced in the plasma discharge of a 50 mm long tantalum-lined copper hollow cathode as an RF-pulsed DC current of 0.30–0.60 A was applied. Approximately 1 torr of Ar was used as the sputter gas, and a trace of SF_6 (0.5%) used

as a reagent gas supplied the fluoride. It was found that including a trace amount of H_2. (1%) in the gas mixture increased the intensity of the observed transitions, though the exact cause of this increase is not known. The laser dyes used, DCM and R6G, allowed data collection over the range of 14,500–17,150 cm^{-1}. Generation times of 50–200 μs were used, giving an effective pathlength of 0.75–3.0 km for the 50 mm hollow cathode in a 1.01 m resonator cavity. As previously described, each plasma spectrum was divided by a background spectrum taken in the absence of the plasma and measured soon after the plasma spectrum was recorded at the same monochromator location. An I_2 spectrum from a heated extra-cavity cell was recorded immediately following each TaF spectrum to allow calibration using reference data from Salami and Ross.[41] Isolated lines are estimated to have an accuracy of ±0.005 cm^{-1}.

3.3 Analysis Results and Discussion

The work published by Ng *et al*.[38] included a computational analysis that predicted several observable transitions in the visible region accessible by the ILS system when used in conjunction with the R6G and DCM laser dyes. In this work, eight bands were observed and recorded at rotational resolution between 14,850 and 16,950 cm^{-1}. These were identified as the (1,0), (0,0), and (0,1) vibrational bands of the $[16.0]0^+ – X\ ^3\Sigma^-(0^+)$ transition and the (2,1), (1,0), (0,0), (0,1), and (1,2) bands of the $[16.3]1 – X\ ^3\Sigma^-(0^+)$ transition.

To obtain the vibrational assignments, the eight observed bands first were sorted into two vibrational progressions. Secure vibrational assignments were made based on the known vibrational constants of the $X\ ^3\Sigma^-(0^+)$ state. For each vibrational

progression, two bands were separated by 697 cm^{-1}, consistent with the $\Delta G_{1/2}$ value reported by Ng *et al*.[38] for the X $^3\Sigma^-(0^+)$ state. The four bands were correspondingly assigned as (0,0) and (0,1) bands of these two transitions, with the two (0,0) bandheads observed near 16,033 cm^{-1} and 16,327 cm^{-1}. Further vibrational assignments were thus straightforward: two bands were observed ~600 cm^{-1} higher in energy than the (0,0) bands, consistent with the vibrational frequencies predicted for the excited states of TaF,[38] and these bands were assigned as (1,0) bands; slightly weaker bands were also observed ~95 cm^{-1} to the red of the (1,0) and (0,1) bands of the 16,327 cm^{-1} system, and were assigned as (2,1) and (1,2) bands, respectively. Ta has only one major stable isotope (^{181}Ta, 99.99% abundant), and thus isotope shifts are not available to further confirm the vibrational assignments.

Each band of the 16,033 cm^{-1} system consisted of only two branches: a single P- and a single R-branch as illustrated in Figure 3.2. Combination differences between these branches in the three observed bands were in agreement with the Δ_2F'' levels from Ng *et al*.[38] for v = 0 and v = 1 of the X $^3\Sigma^-(0^+)$ state, confirming the rotational assignment and the initial vibrational assignment. The lack of a Q-branch indicates that the excited state must be $\Omega = 0^+$ in character, so the band system has been assigned as the $[16.0]0^+ – X\ ^3\Sigma^-(0^+)$ transition of TaF.

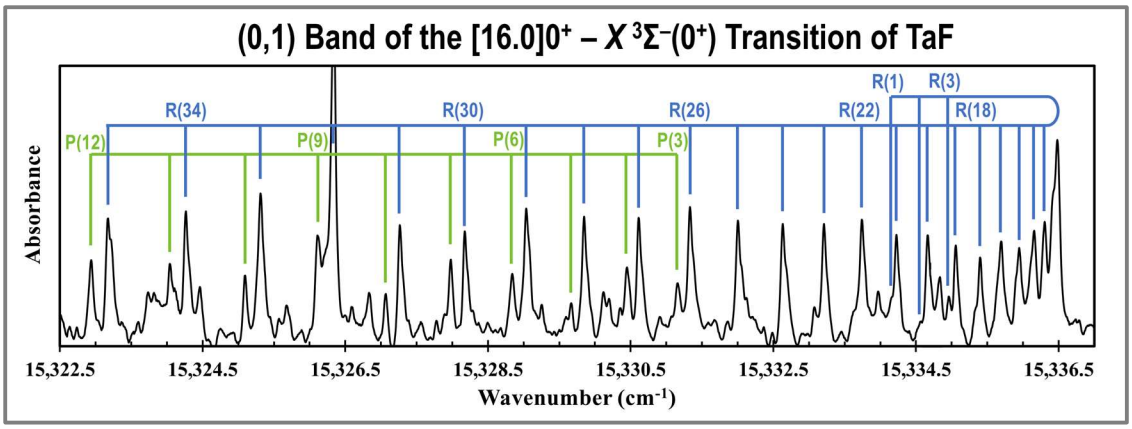

Figure 3.2: Bandhead portion of the (0,1) band of the [16.0]0^+ – X $^3\Sigma^-(0^+)$ transition of TaF, showing P- and R-branches with no Q branch indicating a $\Delta\Omega = 0$ electronic transition. Unlabeled peaks in this spectrum and in Figure 3.3 are not considered to be noise as they are reproducible. Additional lines may be high-J lines of other TaF transitions due to the energetic molecular source, or due to transitions of other species such as TaS formed in the chamber stemming from the use of SF_6 as a reagent gas.

The bands of the 16,327 cm^{-1} system consisted of a P-, a Q-, and an R-branch, as illustrated in Figure 3.3. Again, combination differences between the P- and R-branches were in agreement with the Δ_2F'' levels from Ng *et al.*[38] for v = 0, 1 and 2 of the X $^3\Sigma^-(0^+)$ state, confirming the rotational assignment and the initial vibrational assignment. The strong Q-branch indicates that the transition is $\Delta\Omega = \pm 1$, so the band system has been assigned as the [16.3]1 – X $^3\Sigma^-(0^+)$ transition of TaF.

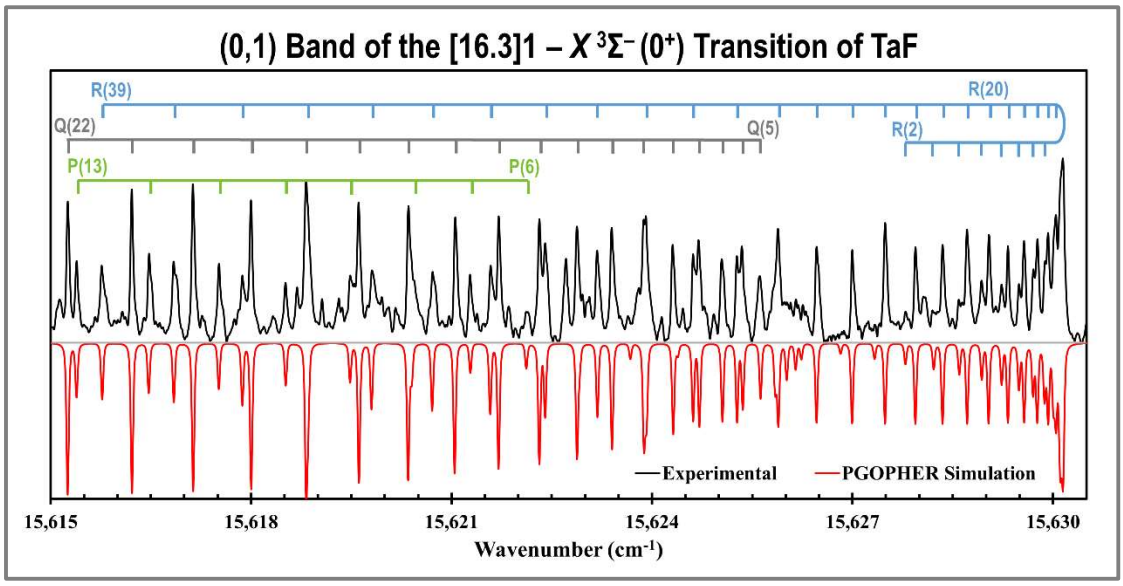

Figure 3.3: Bandhead portion of the (0,1) band of the [16.3]1 – X $^3\Sigma^-(0^+)$ transition of TaF with the experimental spectrum in black (top) and the PGOPHER simulation in red (bottom). For the simulation, the Gaussian and Lorentzian linewidths were set to 0.03 cm^{-1} with T = 500 K. The strong Q-branch is indicative of a $\Delta\Omega = \pm 1$ electronic transition.

The rotational branches were fit to a Hund's case (c) Hamiltonian using PGOPHER.[8] Line positions from five transitions observed by Ng *et al.*[38] that also originate in the X $^3\Sigma^-(0^+)$ ground state were included in the fit to minimize correlation among the fitted constants. In total, 1238 observations were fit to 50 parameters. Twenty-six of these parameters were related to the X $^3\Sigma^-(0^+)$, [16.0]0^+, and [16.3]1 states, with the remaining parameters pertaining to the previously observed excited states. The 26 parameters determined for the X $^3\Sigma^-(0^+)$, [16.0]0^+, and [16.3]1 states are given in Table 3.1. A comparison of the experimental spectrum to the PGOPHER[8] simulation of the (0,1) band of the [16.3]1 – X $^3\Sigma^-(0^+)$ transition is provided in Figure 3.3, above.

Table 3.1: Determined parameters for TaF for the X $^3\Sigma^-(0^+)$, $[16.0]0^+$, and [16.3]1 states are shown in **bold**. A comparison to parameters determined for the ground state by Ng *et al*.[38] is provided in *italics*. All values are in cm^{-1}. Uncertainties are provided as (1σ).

State	Vibrational Level	T_v	B_v	D_v x 10^6	q_v x 10^6
X $^3\Sigma^-(0^+)$	v=0	**0[a]**	**0.296036 (10)**	**0.2121 (48)**	**-**
		0	*0.2961 (1)[b]*	*0.2961 (1)[b]*	-
	v=1	**697.0511 (10)**	**0.294286 (10)**	**0.2132 (48)**	**-**
		697.02 (1)[b]	*0.2943 (1)[b]*	*0.2943 (1)[b]*	-
	v=2	**1388.0977 (26)**	**0.292518 (14)**	**0.2076 (91)**	**-**
		1388.11 (1)[b]	*0.2926 (1)[b]*	*0.2926 (1)[b]*	-
$[16.0]0^+$	v=0	**16030.1291 (10)**	**0.2709921 (96)**	**0.2291 (44)**	**-**
	v=1	**16613.0512 (16)**	**0.269303 (10)**	**0.2249 (49)**	**-**
[16.3]1	v=0	**16323.22755 (100)**	**0.273011 (11)**	**0.1883 (55)**	**1.0158 (13)**
	v=1	**16919.0076 (15)**	**0.271290 (11)**	**0.3208 (66)**	**0.9883 (13)**
	v=2	**17509.0258 (36)**	**0.269809 (22)**	**0.240 (27)**	**0.9808 (49)**

[a]Held fixed in fit.
[b]Ref. [38]

Equilibrium rotational constants (B_e) and bond lengths (R_e) were calculated for the $[16.0]0^+$ and [16.3]1 states using the determined rotational constants, B_v. Additionally, the equilibrium term energy (T_e), vibrational constant (ω_e), and anharmonicity constant ($\omega_e x_e$) were calculated for the [16.3]1 state, and $\Delta G_{1/2}$ was calculated for the $[16.0]0^+$ state. These determined equilibrium constants are given in Table 3.2.

Table 3.2: Equilibrium constants for the X $^3\Sigma^-(0^+)$, $[16.0]0^+$, and [16.3]1 states of TaF are shown in **bold.** Values predicted or observed by Ng *et al.*[38] are shown in *italics*.

State	B_e (cm^{-1})	r_e (Å)	T_e (cm^{-1})	ω_e (cm^{-1})	$\omega_e\chi_e$ (cm^{-1})	$\Delta G_{1/2}$ (cm^{-1})
X $^3\Sigma^-(0^+)$	**0.2969**	**1.817**	**0**[a]	**703.1**	**3.00**	**697.1**
{1}0^+	*0.2989*[b]	*1.811*[b]	*0*[b]	*701.3*[b]	*1.69*[b]	*697.9*[c]
[16.0]0^+	**0.2718**	**1.899**	**16090**	**-**	**-**	**582.9**
{7}0^+	*0.2694*[b]	*1.908*[b]	*16659*[b]	*573.2*[b]	*1.61*[b]	*570.0*[c]
[16.3]1	**0.2738**	**1.892**	**16374**	**601.5**	**2.88**	**595.8**
{11}1	*0.2703*[b]	*1.905*[b]	*16874*[b]	*599.7*[b]	*2.12*[b]	*595.5*[c]

[a] T_v values from Table 1 were adjusted to compensate for the zero-point energy of the ground state.
[b] Predicted value from Ref. [38].
[c] From predicted ω_e and $\omega_e x_e$ values.

The experimental molecular constants were compared to those of the computational predictions.[38] Based on symmetry (Ω value) and excited state molecular constants, the new experimentally observed excited electronic states best correlate to the {7}0^+ and {11}1 states from the computation. Neither of these excited states were used for the seven previously identified electronic states.[38] For comparison, the molecular constants from the computational work for these states are included in Table 3.2. In general, the agreement between the experimentally observed states and these predicted states is quite good.

Interestingly, the {11}1 – X $^3\Sigma^-(0^+)$ transition was predicted to have one of the largest transition dipole moments of any TaF transition at 0.476,[38] where the {11}1 state is primarily $^3\Pi_1$ in character and thus this transition is fully allowed. The observed {7}0^+ – X $^3\Sigma^-(0^+)$ transition was calculated to have a very low transition dipole moment of 0.006, and, therefore, would not be expected to be readily observable. Spectral lines corresponding to this transition were quite strong considering the low transition dipole

moment predicted; however, the difference may help to explain why fewer bands of the $[16.0]0^+ - X\ ^3\Sigma^-(0^+)$ transition were observed compared to the other transition.

3.4 Conclusions

Eight vibrational bands of two new electronic transitions of TaF have been recorded using intracavity laser absorption spectroscopy and were rotationally analyzed. Molecular constants for the $[16.0]0^+$ and [16.3]1 states are presented. Molecular constants for the $X\ ^3\Sigma^-(0^+)$ ground state have improved the accuracy of those given previously via additional high-resolution data with rotational structure extending to higher J. Transition energies for the excited states were found to be roughly 500 cm^{-1} lower than those predicted,[38] and other spectroscopic parameters agreed well with predictions. The most notable difference from the computational study was in the observed strength of the $[16.0]0^+$ transition given the very low predicted transition dipole moment.

CHAPTER 4:
TUNGSTEN SULFIDE (WS)

4.1 Introduction to WS

The electronic structure of tungsten monosulfide, WS, has become a focus of both theoretical and spectroscopic interest. Tungsten disulfide, WS_2, has been investigated as a thin film semiconductor for use in nanoelectronic devices[47] and as a window layer in solar cells, with potential to provide a low cost, nontoxic photovoltaic material.[48] A growing body of work has begun to elucidate more details of the very complex electronic structure of the W-S bond that results from the large number of unpaired electrons and accessible valence orbitals. Density functional theory (DFT) calculations were performed in 2002 by Liang and Andrews.[49] In 2017, Sevy, *et al.*[50] provided more DFT calculations and measured the bond dissociation energy of WS using resonant two-photon ionization spectroscopy. In 2019, Tsang *et al*.[39] provided a more thorough look at WS with high-level *ab initio* calculations, experimental observations using laser induced fluorescence (LIF), and analyses of several transitions. At the 74th meeting of the International Symposium on Molecular Spectroscopy (ISMS),[51] our group reported preliminary findings of the spin-spin separation of the X(0^+) and X(1) states based on observation and analysis of the [15.30]1 – X(0^+) (0,0) band with correlation to Tsang's [a+13.12]1 state. Work by Zhang *et al.*[52] incorporating single vibronic level emission (SVL) spectra as well as LIF supported our initial findings with an analysis that included several vibrational bands from transitions between the [15.10]1 and [15.30]1 excited states and both Ω-components of the X $^3\Sigma^-$ ground state. Our research group has published two recent papers (Harms *et al*.[53,54]) that report the observation of new

electronic transitions that connect to the $X(0^+)$ ground state. Most recently, a paper by Zhang *et al*.[55] reported the identification of seven low-lying Ω states observed by dispersed fluorescence, and included the rotational analysis of the (0,0) bands of additional electronic transitions observed using LIF. Some transitions observed strongly in the LIF spectrum were ‘‘quasi-forbidden” by the computational model implemented by Tsang *et al.*,[39] motivating a reexamination of the relativistic corrections to hopefully bring theory and experiment into closer alignment.[55] The spin–orbit matrix was calculated at a higher level of theory, and transition dipole moments (TDMs) were calculated from the resulting Hund’s case (c) Ω-states. These TDMs were used to correlate the experimental electronic states observed by LIF to the *ab initio* Ω-states, providing some insight into the underlying Λ-S character of those spectroscopic states.

This chapter focuses on work with four excited states of WS. The first, $[15.05]0^+$, was observed for the first time using ILS-FTS.[56] Three bands were analyzed and identified as the (0,0), (1,0), and (2,0) bands of the $[15.05]0^+ – X(0^+)$ transition. With the availability of high-resolution spectra, data for all four abundant isotopologues of WS, $^{182}W^{32}S$, $^{183}W^{32}S$, $^{184}W^{32}S$, and $^{186}W^{32}S$, are included in the analysis, which is discussed in Section 4.2.

As mentioned above, our initial work with the [15.30]1 state was initially presented at ISMS in 2019;[51] however, the discovery of irregularities in the spectra significantly delayed completion of the analysis. It was later found that the v = 2, 3, and 4 vibrational levels of the $[14.26]0^+$ state were very near the v = 0, 1, and 2 levels of the [15.30]1 state, resulting in significant mass- and J-dependent perturbations. The

first reporting by Harms, *et al.* on the [14.26]0^+ – X(0^+) transition[54] incorporated ILS-FTS data from our lab[53] as well as LIF data from two transitions observed by Tsang *et al*.[39] to conduct a comprehensive fit of the data to a mass-independent Dunham model[5] to characterize the ground state, with a band by band fit of v = 0 and v = 1 of the [14.26]0^+ state. Rotational and vibrational parameters from the band-by-band fit were used to predict the parameters for v = 2 of the state to begin the deperturbation analysis of the [15.30]1 and [14.26]0^+ states,[57] which will be the subject of Section 4.3.

Another previous Harms *et al.*[53] paper studied the v = 1 vibrational level of the [13.10]1 state. The v = 0 level was part of a newer analysis involving WS transitions near 13,100 cm^{-1}, where the (0,0) bands of the [15.30]1 – X(1) and [13.10]1 – X(0^+) transitions were analyzed and are discussed in Section 4.4.

4.2 The [15.05]0^+ State

In this work, we have observed several new vibrational bands of a new electronic transition of WS using ILS-FTS. Three bands were analyzed and identified as the (0,0), (1,0), and (2,0), bands of the WS [15.05]0^+ – X(0^+) transition. The determined molecular constants are presented here. This work was published in the Journal of Molecular Spectroscopy.[56]

4.2.1 Experimental Methods

The spectra used for analysis were collected in the visible region (14,985 – 16,100 cm^{-1}) using the DL ILS-FTS system. The ILS component used DCM laser dye. WS molecules were produced within the resonator cavity of the ILS laser in a plasma discharge created when a radio frequency-pulsed DC current of 0.50 – 0.60 A or a DC

current of 0.05 – 0.15 A was applied by an ENI RPG50 Pulsed DC plasma generator (now MKS RPDG 5 kW pulsed DC Plasma Generator) to a 25 mm long tungsten-lined copper hollow cathode. The total pressure within the reaction chamber was approximately 1 torr attained by gas flows of approximately 70% Ar and 30% H_2, with a trace of CS_2, regulated by three mass flow controllers. An estimated plasma temperature of 500 K and a molecular mass of 216 amu ($^{184}W^{32}S$) predicts a full width half maximum (FWHM) Doppler linewidth of 0.017 cm^{-1}.[4] For this study, spectra were acquired at a resolution of 0.01 cm^{-1} and 4–6 scans of the FT spectrometer were coadded to produce each spectrum. Acquisition of each ~ 40 cm^{-1} wide plasma spectrum was followed by collection of a background spectrum with identical instrument settings. The two spectra were divided using the spectrum calculator function in OPUS, and only the most intense central portion (~20 cm^{-1}) of each Gaussian laser output profile was used.

Six rotational bands were identified in the region investigated that have been assigned to the (2,0), (3,1), (1,0), (2,1), (0,0), and (1,1) bands of the $[15.05]0^+ – X(0^+)$ transition of WS. Each band spanned ~ 100 cm^{-1} (~5 adjacent/overlapping ILS profiles) before signal-to-noise became too low to provide additional insight. Power supply and ILS settings were optimized for each band system prior to collection. While the alteration of conditions prevents direct comparison of relative intensity, the (0,0) band was the strongest of those studied, appearing at very ‘‘gentle” discharge conditions (50 mA DC) and short generation times (effective pathlength, $L_{eff} < 200$ m). The (1,0) band was slightly weaker, requiring a higher current discharge, and the (2,0) band was significantly weaker than the other two, requiring both a longer generation

time (L_{eff} ~ 500 m), as well as a higher current. For the (2,0) band, all plasma spectra and all background spectra were added together before division to enhance the signal-to-noise ratio. Using PGOPHER,[8] a smooth baseline correction was applied to compensate for any shift in laser profile position between collection of plasma and background spectra. Each baseline-corrected spectrum was converted to an absorbance spectrum. The spectra were calibrated to an accuracy of 0.001 cm^{-1} using observed Ar I line positions reported by Kerber *et al*.[44] The (0,0), (1,0), and (2,0) bands were then rotationally analyzed using PGOPHER,[8] with a total of 1,118 lines included in the fit. Molecular constants determined by Harms *et al*.[54] for the ground state were used and held fixed in the fit.

4.2.2 Description and Identification of Spectra

Three prominent, red-degraded bands were observed in the visible region at Doppler-limited resolution. The bandheads appeared at approximately 15,051, 15,574, and 16,093 cm^{-1}, and were analyzed and identified, respectively, as the (0,0), (1,0), and (2,0) bands of the $[15.05]0^+ – X(0^+)$ transition of WS. Weaker bandheads were observed 33 – 40 cm^{-1} to the red of each of the main bandheads, appearing at 15,018, 15,537, and 16,053 cm^{-1}, and were identified as the (1,1), (2,1), and (3,1) bands. These bands were not rotationally analyzed as they were significantly weaker and obscured by overlapping lines of the stronger bands. The (1,1) band was considerably weaker than both the (2,1) and (3,1) bands, which were quite strong. A strong vibrational progression generally indicates a change in bond length upon excitation.

Each band consisted of one P- and one R-branch for each of the four prominent isotopologues, ^{182}WS, ^{183}WS, ^{184}WS, and ^{186}WS, as illustrated in Figure 4.1. The lack

of an observable Q-branch indicates the transition is of $\Delta\Omega = 0$ symmetry. Combination differences confirmed the lower state is the previously observed[39] $X(0^+)$ ground state of WS, and thus the new [15.05] excited state of WS conclusively is assigned to be of $\Omega = 0^+$ symmetry. At low J, the vibrational separation of isotopologues is fairly consistent with what is expected to be seen for the (0,0), (1,0), and (2,0) bands. The clear isotope separation at high J in the P-branch of the (0,0) band is illustrated in Figure 4.2.

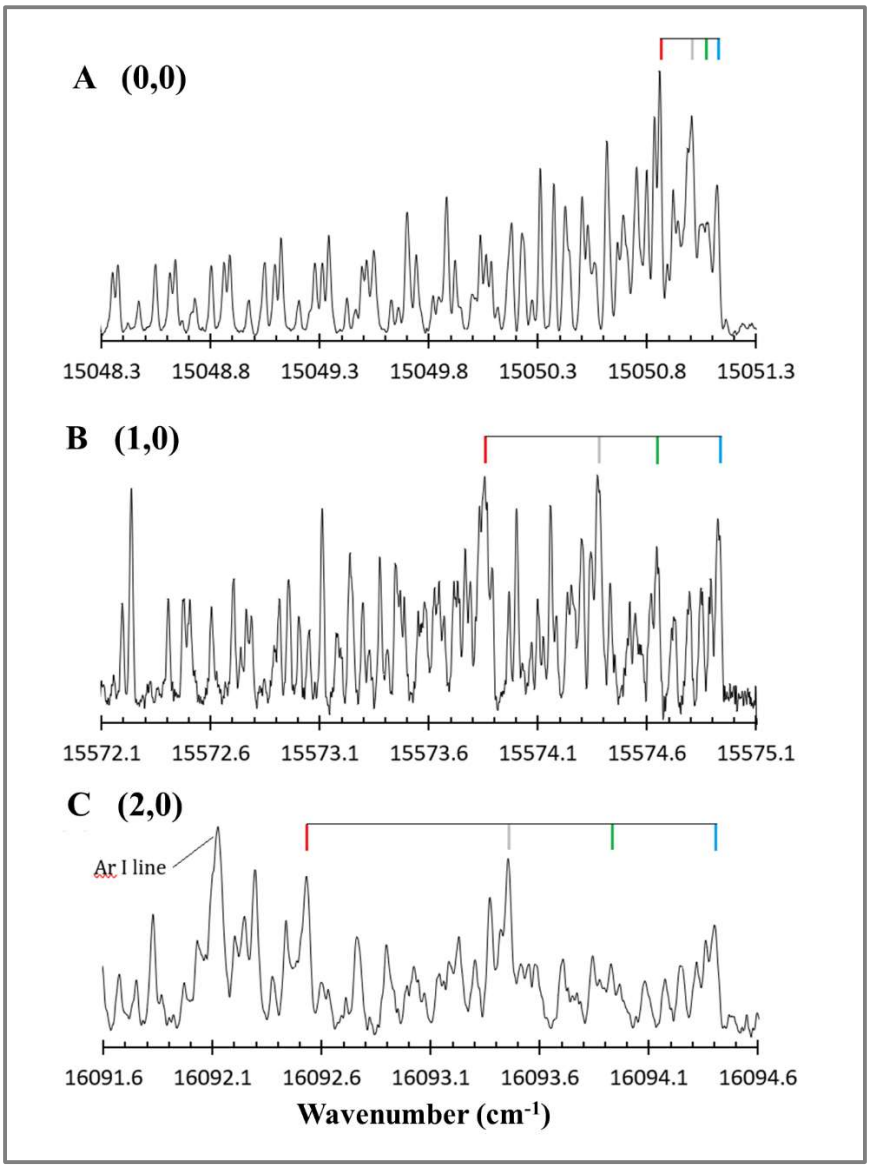

Figure 4.1: Bandhead positions of the ^{182}WS, ^{183}WS, ^{184}WS, and ^{186}WS isotopologues, shown by the upper color-coded tie lines, highlighting the vibrational shifts observed in the **A** (0,0) band, **B** (1,0) band, and **C** (2,0) band. Energy differences between the ^{182}WS and ^{186}WS bandheads for the (0,0), (1,0), and (2,0) bands are 0.262, 1.076, and 1.873 cm^{-1}, respectively.

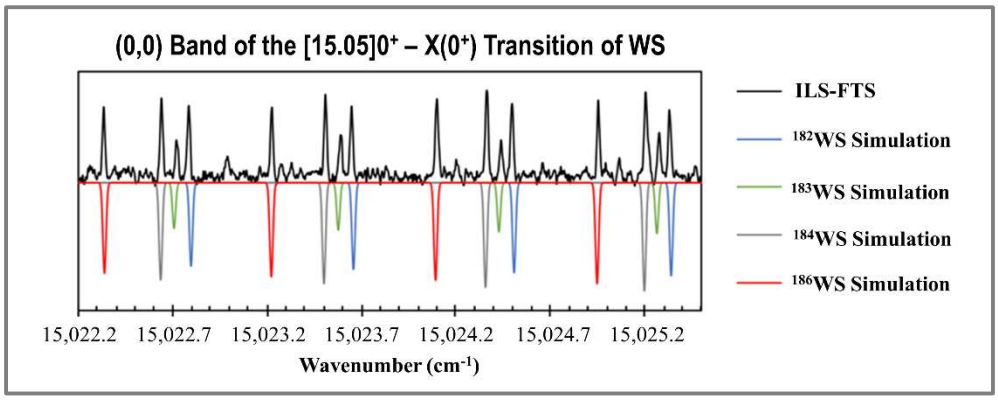

Figure 4.2: Illustration of clear separation of ^{182}WS, ^{183}WS, ^{184}WS, and ^{186}WS isotopologues in the (0,0) band of the [15.05]0^+ – X(0^+) transition of WS. Lines shown are P-branch lines with J = 41–44 (from right to left).

4.2.3 Analysis and Results

Lines with J values up to ~80 were identified for many branches, which were fit in PGOPHER[8] as Hund's case (c) $\Omega = 0^+$ states. Parameters for the X(0^+) ground state have been well defined and were held fixed to values given in Harms *et al.*[54] A significant perturbation was seen at high-J in the (0,0) band. The perturbation is strongly J-dependent and mass-dependent. For example, the perturbation appears at much lower J for the ^{186}WS isotopologue (J ~ 45) than for the ^{182}WS isotopologue (J ~ 55). Figure 4.3 illustrates the fit residuals (obs-calc) for the P-branches of the (0,0) band at J > 40. The residuals for the R-branches show a very similar pattern. In the final fit, a higher order rotational parameter, H_0, was included in the excited state, and higher-J lines that could not be fit were excluded. Because the (0,0) band was perturbed, a Dunham-type analysis of the excited state was not attempted. A total of 1,118 observations were fit to 40 parameters, which are given in Table 4.1. A comparison of the ILS spectrum with the final PGOPHER[8] simulation is given as Figure 4.4.

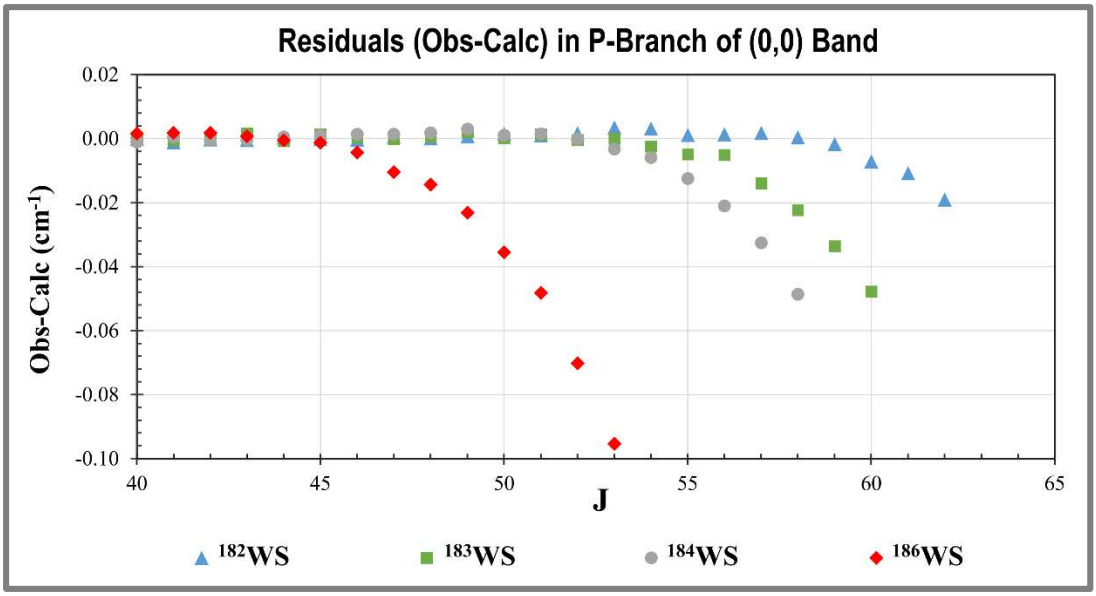

Figure 4.3: Fit residuals (obs-calc) for P-branches in the (0,0) band of the $[15.05]0^+ - X(0^+)$ transition of WS of ^{182}WS, ^{183}WS, ^{184}WS, and ^{186}WS isotopologues. Calculated line positions are extrapolated from fit of lines with J < 45.

Table 4.1: Molecular constants for the $[15.05]0^+$ state of WS. All values reported in cm^{-1}. Uncertainties are given as (1σ).

		$[15.05]0^+$			
	v	**T_v**	**B_v**	**D_v x 10^8**	**H_v x 10^{12}**
^{182}WS	0	15048.10327 (61)	0.13838887 (179)	3.422 (135)	-5.068 (277)
	1	15572.15326 (77)	0.137821552 (573)	3.3378 (92)	
	2	16091.81945 (44)	0.13734100 (33)	3.8102 (46)	
^{183}WS	0	15048.05587 (66)	0.13826939 (250)	3.849 (224)	-6.290 (543)
	1	15572.15789 (55)	0.13781848 (45)	3.2947 (78)	
	2	16091.34396 (69)	0.13723005 (55)	3.8284 (85)	
^{184}WS	0	15048.00716 (58)	0.13813558 (219)	2.964 (202)	-1.2764 (503)
	1	15571.60762 (41)	0.13761263 (31)	3.4495 (47)	
	2	16090.87761 (45)	0.13711769 (34)	3.8083 (47)	
^{186}WS	0	15047.88612 (72)	0.13786065 (358)	2.886 (447)	-3.092 (152)
	1	15571.08895 (41)	0.13740351 (34)	3.4950 (56)	
	2	16089.95185 (46)	0.13689934 (36)	3.8433 (51)	

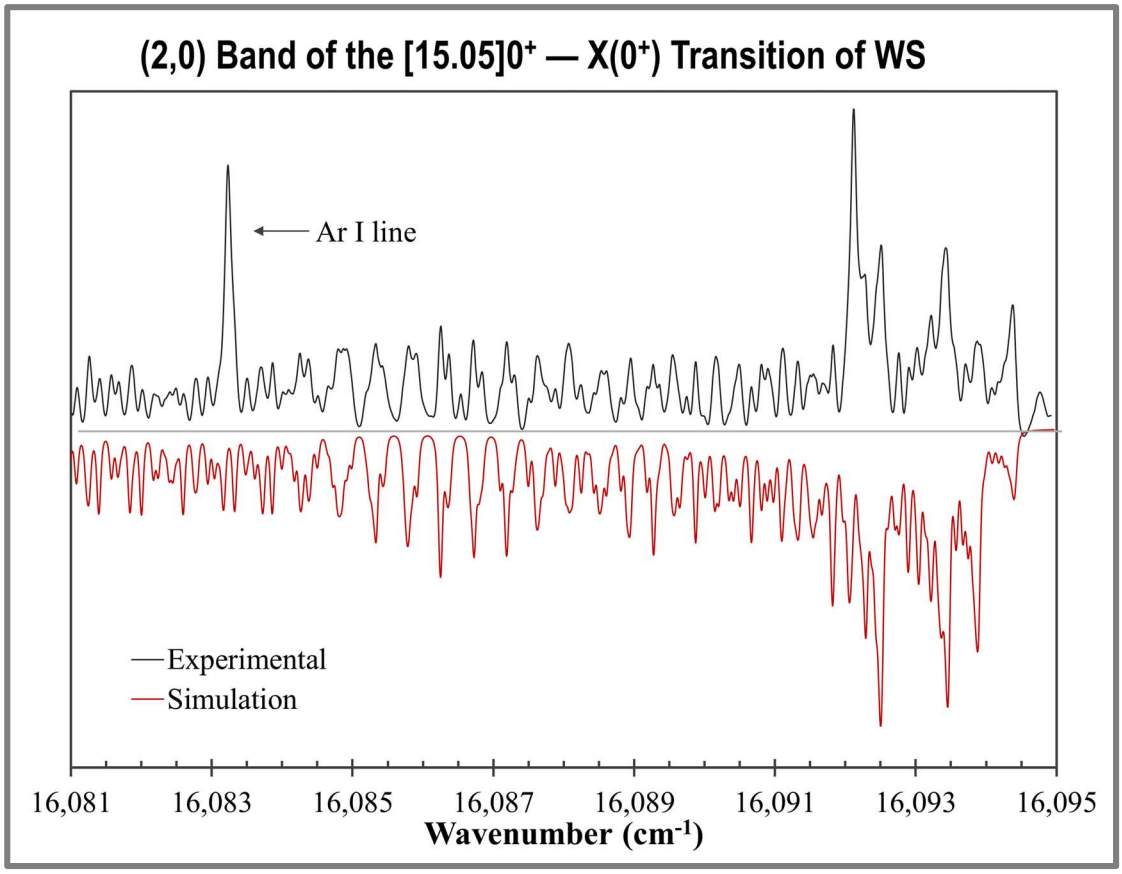

Figure 4.4: Comparison of the experimental spectrum and PGOPHER simulation of the (2,0) band of the $[15.05]0^+ - X(0^+)$ transition of WS.

Several inferences regarding the perturbing state can be made based on the observed spectra. Firstly, because the perturbed lines appear at lower energy than the extrapolated positions, i.e., obs–calc < 0, we know that the perturbing state is higher in energy than the $[15.05]0^+$ state. The observation of a nearby [15.07]1 state recently reported by Zhang *et al.*[55] initially was a candidate for the cause of this perturbation; however, comparison of B values shows that the new [15.07]1 state at higher-energy has a larger B value, and thus the rotational levels of the [15.07]1 and $[15.05]0^+$ states do not approach with increasing J. Secondly, the mass-dependence of the perturbation

suggests that the perturbing state has $v > 0$. Since the perturbed state is $v = 0$, there is minimal separation between isotopologues. The larger isotope separation inherent in higher vibrational levels would likely cause the interaction to take place at different J, as we see in the spectra. Finally, the absence of a perturbation in $v = 1$ and $v = 2$ indicates that the perturbing state must have a significantly different vibrational frequency, else the higher vibrational levels would be similarly affected.

Using the molecular constants given in Table 4.1, equilibrium constants for the ^{184}WS isotopologue were calculated, including rotational constant (B_e), bond length (r_e), term energy (T_e), vibrational constant (ω_e), and anharmonicity constant ($\omega_e x_e$). These calculated values are presented in Table 4.2. The experimental results from the ^{184}WS isotopologue also are compared to the theoretical predictions given by Tsang *et al*.[39] (and Zhang *et al*.[55]) for their calculated $\{7\}0^+$ state. There, the 7 in {} indicates that this state is the 7th *ab initio* $\Omega = 0^+$ state in terms of relative energy. It is worth noting that this computational correlation contradicts Table 3 from Zhang *et al*.,[55] in which the $[17.25]0^+$ state is correlated to the $\{7\}0^+$ state. Their study of WS has been concurrent with our own, and they were unaware of the $[14.26]0^+$ and $[15.05]0^+$ states observed with ILS-FTS in our previous work[54] and this work. Simple energy ordering would suggest this reassignment, but the correlation can be further justified by examining the predicted TDMs of Zhang *et al*.[55] and the experimental transitions observed by ILS-FTS[53,54] and by LIF.[39,52,55]

Table 4.2: Equilibrium constants for $^{184}W^{32}S$ determined by **this work (bold)** and by *computational prediction[39] (italics)*.

^{184}WS	B_e (cm^{-1})	r_e (Å)	T_e (cm^{-1})	ω_e (cm^{-1})	$\omega_e\chi_e$ (cm^{-1})
[15.05]0^+	**0.1384**	**2.115**	**14785**	**528**	**2.2**
{7}0^+	*0.1373*[a]	*2.123*[a]	*16850*[a]	*530*[a]	*3.4*[a]

a – From Ref. [39]

ILS-FTS is a direct absorption technique – ground state (or low-lying) WS molecules are excited by a single photon. This type of measurement requires a large TDM between the initial state and an excited state that occurs in the visible (or near-IR). LIF, on the other hand, is a multi-photon measurement technique – a photon is absorbed, exciting the WS molecule, then the photon is emitted and detected using a photomultiplier tube. Laser scatter precludes detection at the excitation wavelength, and cutoff filters introduce a minimum separation between the excitation energy and the detection energy of the involved photons. As such, LIF transitions are expected to be strong when an excited state has a large transition dipole moment with at least two low-lying states – one for excitation and one for detection. This may explain why the [15.05]0^+ – X(0^+) transition was not observed by Zhang *et al.*:[55] the transition dipole moments from the {1}0^+ ground state (in a.u.) are 0.021, 0.190, 0.122 and 0.097 to the {5}0^+, {6}0^+, {7}0^+, and {8}0^+ states, respectively. These *ab initio* states correlate most closely to the [14.26]0^+, [14.76]0^+, [15.05]0^+, and [17.25]0^+ states: transitions involving the [14.26]0^+ and [15.05]0^+ states have not been reported by LIF, but vibrational progressions involving these states and the X(0^+) state have now been extensively recorded using ILS-FTS. While the {6}0^+ and {8}0^+ states have transition dipole moments of 0.208 and 0.118 a.u. to the X(1) state (and reasonable TDMs to the Ω sub-states of the low-lying $^5\Pi$ state), the TDMs from the {5}0^+ and {7}0^+ states are

only 0.005 and 0.072 a.u. to the X(1) state (with negligible dipole moments to the $^5\Pi$ Ω sub-states) and would be much more difficult to observe in fluorescence.

4.2.4 Conclusions

Six new bands of WS have been observed using ILS-FTS, and have been assigned as the (0,0), (1,0), (2,0), (1,1), (2,1), and (3,1) bands of the $[15.05]0^+ - X\ ^3\Sigma^-(0^+)$ transition. Rotational analyses of the three strongest bands used Doppler-limited line positions of the four major isotopologues. The ground state constants were held fixed to those previously determined.[54] A perturbation with a large J-dependence was observed in v = 0 of the new $[15.05]0^+$ state that is absent for v = 1 and v = 2. The new electronic state is tentatively assigned to the $\{7\}0^+$ state as calculated by Tsang *et al*.[39]

4.3 Deperturbation of the [15.30]1 and [14.26]0⁺ states

The $[15.30]1 - X(0^+)$ transition was first reported in the literature with a study that used LIF spectra collected from a molecular beam. The low temperature of that technique inherently limits observation of rotational structure to low-J transitions. This differs significantly from the spectra obtained using a hollow cathode discharge: in many cases, rotational branches extend to $J'' > 100$ when observed in absorption using ILS. Additionally, that initial analysis only determined parameters for the most abundant isotopologue, $^{184}W^{32}S$, because the isotopologue structure could not be resolved for low-J lines in the (0,0) band. This structure is more apparent in the high-J transitions observed at Doppler-limited resolution using ILS-FTS: rotational structure for each abundant isotopologue of WS has been observed and identified in absorption using ILS-FTS.

In this work, the (0,0), (1,1), (1,0), (2,1), and (2,0) bands of the [15.30]1 – X(0^+) transition were recorded by ILS-FTS and rotationally analyzed using PGOPHER.[8] Rotational transitions were observed to very high J (J″>100) where isotopologue structure due to W could be clearly identified. A heterogenous perturbation[6] was observed in the P- and R-branches of each of these transitions. The strong Q-branch of each band was quite regular in appearance from low to high J. The observed perturbation is J-dependent: this dependence varies slightly for each isotopologue, perturbing the heaviest isotopologue (^{186}WS) at the lowest J-value. It is believed that the perturbing levels originate from excited vibrations of the [14.26]0^+ state, which was characterized by our group previously.[54] Newly measured lines for the (2,0) and (3,0) bands of the [14.26]0^+ – X(0^+) transition were added to this fit and used to assist in a deperturbation analysis of the [15.30]1 state. The X(0^+), [15.30]1, and [14.26]0^+ states were fit to a mass-independent Dunham model[5] using a constrained variables approach.[9] The vibrational dependence of the X(0^+) and [14.26] 0^+ states was determined by including line positions of the (1,0), (0,1), and (1,2) bands of the [14.26]0^+ – X(0^+) transition from our previous analysis.[54] The Dunham[5] model required slight corrections to the vibrational term energies for each isotopologue. In general, these corrections are quite small (<0.5 cm^{-1}), especially if one considers that the Dunham model is only appropriate for a "smooth" potential, and that the [14.26]0^+ and [15.30]1 states are known to interact. The final fit included line positions from Harms *et al.*[54] and Tsang *et al.*[39] of transitions involving the X(0^+) state to minimize correlation of parameters between all three states. The deperturbation analysis of the [15.30]1 state's v = 0 and v = 1 vibrational levels was previously published in the

Journal of Molecular Spectroscopy.[57] Results for the addition of the v = 2 level are being prepared for submission.

4.3.1 Experimental Methods

Experimental spectra were collected using the DL ILS-FTS system. Target molecules were produced in the plasma discharge created by applying an electrical current of 0.15 A to a 25 mm W-lined copper hollow cathode, in the presence of approximately 70% Ar, and 30% H_2, with a trace amount of CS_2. In this gas mixture, Ar is used as a sputter gas to vaporize W molecules from the surface of the cathode, and CS_2 provided sulfur for the reaction. The addition of H_2 has been found to increase the intensity of the transition, though the specific catalytic mechanism is unknown. The total pressure in the reaction chamber was about 1 torr.

In these experiments, t_g values of 25 – 90 μsec were used, corresponding to effective pathlengths of 0.2 – 0.7 km. A resolution of 0.01 cm^{-1} was used for collection of spectra via FTS, corresponding to the calculated Doppler width of WS lines of 0.017 cm^{-1} (assuming a plasma temperature of approximately 500 K),[4] and each spectrum was composed of four coadded FTS scans. Spectra collected during operation of the plasma discharge were followed by collection of a background spectrum with no discharge present. Each experimental spectrum was divided by the corresponding background spectrum using Bruker's OPUS (v.8.5.29) software. For the weaker (1,0) band, a series of 20 partially overlapping experimental spectra were added together to increase the signal to noise ratio, then divided by the corresponding series of coadded background spectra, to give one continuous spectrum. All resultant experimental spectra were

baseline corrected, then calibrated as follows using the appropriate functions in PGOPHER.[8]

A beamsplitter allows dispersed ILS and ILS-FTS measurements to be recorded simultaneously. The line positions for the dispersed ILS measurements were verified to 0.005 cm^{-1} accuracy by collecting spectra from an extracavity I_2 cell at each monochromator location and calibrating those spectra using the data from Salami and Ross.[41,26] In the absence of suitable Ar I[44] or H_2O[43] lines typically used to calibrate ILS-FTS spectra, these ILS-FTS spectra were calibrated using unblended plasma lines identified in both the Dispersed ILS and ILS-FTS spectra. The internal precision of the ILS-FTS measurements is estimated to be near 0.001 cm^{-1}: as such, the wavenumber accuracy of the measurements is limited to the 0.005 cm^{-1} uncertainty of the reference I_2 data, but the fitting uncertainty is expected to be somewhat lower.

4.3.2 Analysis and Results

Prominent red-degraded bandheads were observed at approximately 15,303 and 15,822 cm^{-1}. A much weaker bandhead was observed near 16,340 cm^{-1}. The band at 15,303 cm^{-1} was consistent with that observed previously by Zhang, *et al.*,[52] and the three bands were thus identified as the (0,0), (1,0), and (2,0) bands of the [15.30]1 – $X(0^+)$ transition. Weaker bandheads within the (0,0) and (1,0) bands appeared at 15,265 and 15,784 cm^{-1} and were identified as belonging to the (1,1) and (2,1) bands, respectively. Due to lower signal to noise in the (2,0) band and congestion in the (2,1) band, v = 2 was not included in the initial analysis,[57] but after the (2,0) band was later collected with greater transition intensity, it was added to the fit. The prominent bands consisted of P-, Q-, and R-branches, consistent with a transition with $\Delta\Omega = \pm 1$

symmetry. Upon initial inspection, the (0,0) band showed a single, regular Q-branch and a single bandhead with no observable separation of abundant isotopologues, as expected. However, portions of the P- and R-branches were oddly irregular. Initial fitting of the Q-branch in PGOPHER[8] and comparison with simulations using previously determined parameters[54] suggested that higher J P- and R-lines were perturbed, resulting in an appreciable isotopologue shift that was fully resolved at Doppler limited resolution, as shown in Figure 4.1. Here, the Fortrat diagram of the PGOPHER[8] simulation, which illustrates branch structure by plotting line positions as J″ vs. wavenumber (cm^{-1}), indicates potential perturbations in the R-branch lines from roughly J′ = 30 to J′ = 60, with isotopologues widely separated in this region. At higher and lower values of J, the P- and R lines for each isotopologue are of nearly identical transition energy. Λ-doubling in the [15.30]1 state is observed indirectly in the spectrum since the P- and R-branches have *e* symmetry, while the Q-branch has Q_{fe} symmetry for the [15.30]1 – X(0^+) transition.

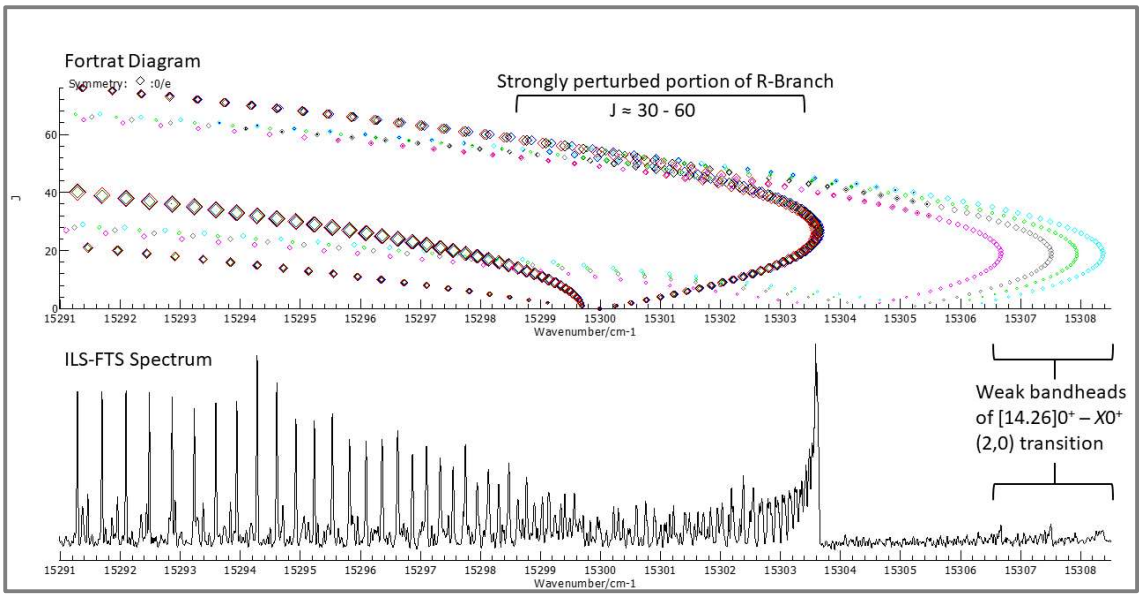

Figure 4.5: Fortrat diagram (upper panel) corresponding to the origin and bandhead regions of the (0,0) band of the [15.30]1 – X $^3\Sigma^-(0^+)$ transition with energy levels for v = 2 of the [14.26]0^+ state included to illustrate the isotopologue-dependent perturbation observed in the R-branch of the experimental spectrum (lower panel). In contrast to this highly irregular portion, the left side of the figure shows the very regular and unperturbed portion of the P branch below J = 20, and the Q branch below J = 40, with lines for each isotopologue stacked together in this region. A temperature of 600 K was used for the PGOPHER simulation.

The perturbation in the rotational structure can be quite informative. Only P- and R-branches are affected in the [15.30]1 excited state and the ground state is 0^+; thus, the *e*-levels of the [15.30]1 state are being perturbed. This indicates that the perturbing state has symmetry $\Omega=0^+$. As found in the spectrum, the perturbation initially lowers the energy of the rotational levels as J increases, then suddenly raises the energy of rotational levels of the [15.30]1 state. This indicates that the perturbing state must be higher in energy and have a smaller rotational constant, B, to produce rotational energy levels that are initially higher than those of the [15.30]1 state then become lower in energy as J increases. The crossover point in the perturbed branches occurs between J′=35-50, with the exact J-value of the crossing dependent upon the isotopologue, as

can be seen in Figure 4.7. The reduced energy level diagrams illustrate how the levels cross, including the specific J-value for the crossing point of each isotopologue. The perturbation interaction is strongest at these crossing points, producing large deviations from "regular" rotational structure. The vibrational constants are mass dependent, with the ^{186}WS isotopologue of lowest energy, and the ^{182}WS isotopologue of highest energy. The separation of these isotopologues will depend on Δv for a given transition. Generally, as Δv increases, the magnitude of the observed isotopologue shift will increase, with ^{186}WS moving lower and lower in energy compared to ^{182}WS. If Δv is negative, ^{182}WS will be lowest in energy and the magnitude of the shift is proportional to the magnitude of Δv. The magnitude of shift in J between isotopologues indicates that there must be a change in vibrational levels between the two interacting states. Consequently, the state(s) perturbing the [15.30]1 state must have $v > 0$.

In previous work with the WS molecule,[54] a Dunham-like model was used to describe the (1,0), (0,1), and (1,2) bands of the $[14.26]0^+ - X(0^+)$ transition. The (2,1) band of that transition was very strong, but a rotational assignment could not be secured due to overlap with the (1,0) band and some irregularity in branch structure. The clear irregularity in rotational structure seen in Figure 4.5 prompted the question: are these two excited states, $v = 2$ of $[14.26]0^+$ and $v = 0$ of [15.30]1, interacting with each other, complicating observed rotational structure and making branches difficult to track? The weak bandheads observed on the right side of Figure 4.5 are consistent in energy with the (2,0) band of the $[14.26]0^+ - X(0^+)$ transition predicted by the Dunham-like model. The simulated branch structure in the Fortrat diagram clearly illustrates a crossing of these two states between J=30-60. The perturbations in the (0,0) and (1,0) bands of the

[15.30]1 transition were subsequently treated as interactions with the nearby v = 2 and v = 3 (respectively) levels of the [14.26]0^+ state of WS. An energy level diagram illustrating the proximity of the vibrational levels of the interacting states is given as Figure 4.6.

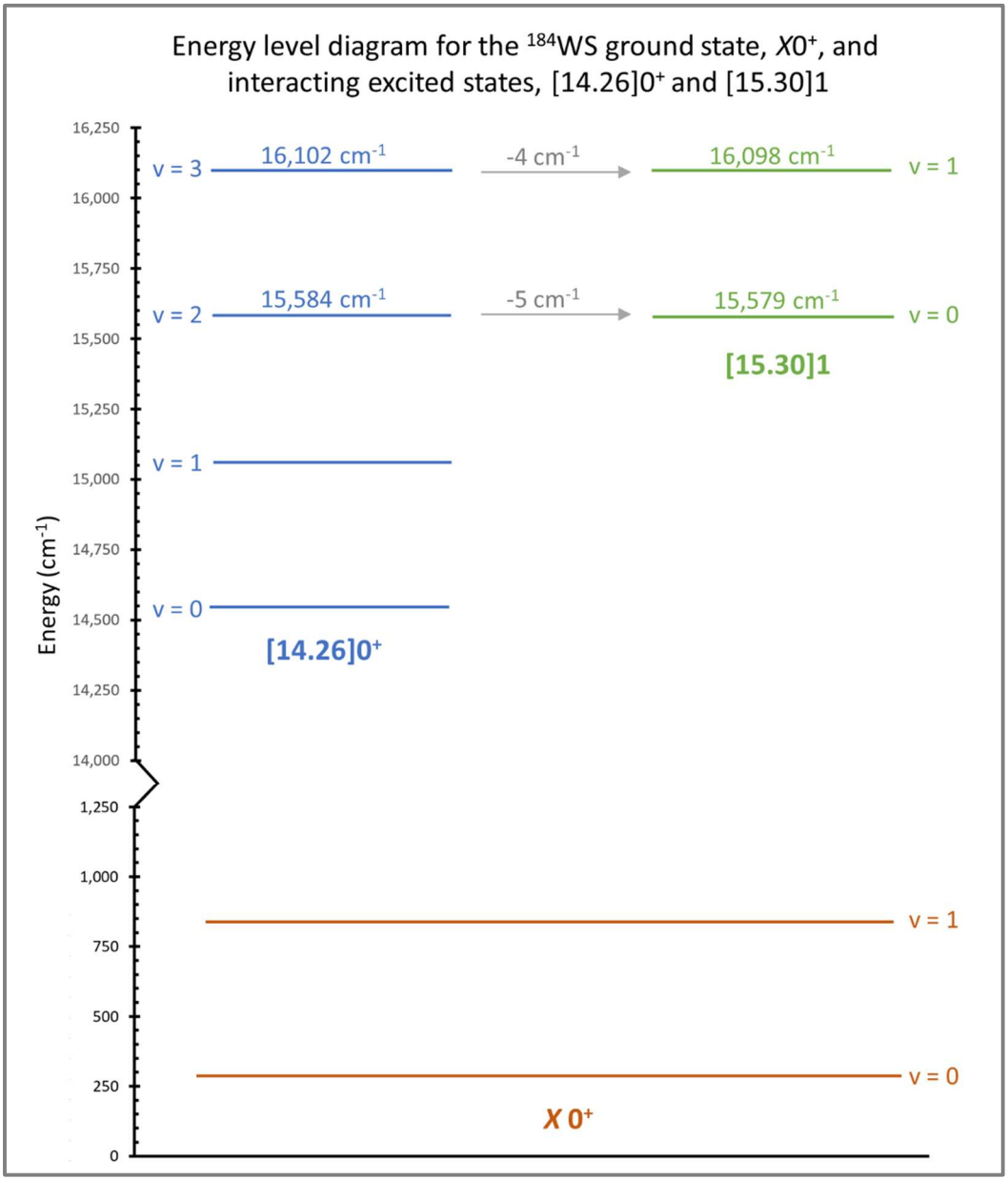

Figure 4.6: Simple energy level diagram showing relative energies of the vibrational levels of the X $^3\Sigma^-(0^+)$, [14.26]0^+, and [15.30]1 states of ^{184}WS. The origins of v = 2 of [14.26]0^+ and v = 0 of [15.30]1 are separated by only 5 cm^{-1}, while [14.26]0^+ v = 3 and [15.30]1 v = 1 are separated by 4 cm^{-1}.

The L-uncoupling operator was used to model the perturbation interaction in PGOPHER.[8] As described by Lefebvre-Brion and Field,[6] the L-uncoupling operator is relevant in cases where there is a heterogeneous electronic-rotational perturbation between two states with $\Delta S = 0$, $\Delta\Omega = \pm 1$ and $\Delta\Lambda = \pm 1$. A heterogeneous interaction produces the previously described effects to the energy levels of the interacting states, which are also illustrated in panel B of Figure 4.7. The symmetrized matrix element is given by $\langle J, \Lambda=0, \Omega=0 \mid J+L- \mid J, \Lambda=1, \Omega=1 \rangle = \sqrt{J(J+1)}$. The L-uncoupling value determined by PGOPHER is a numerical multiplier of the matrix elements and is thus unitless.[8]

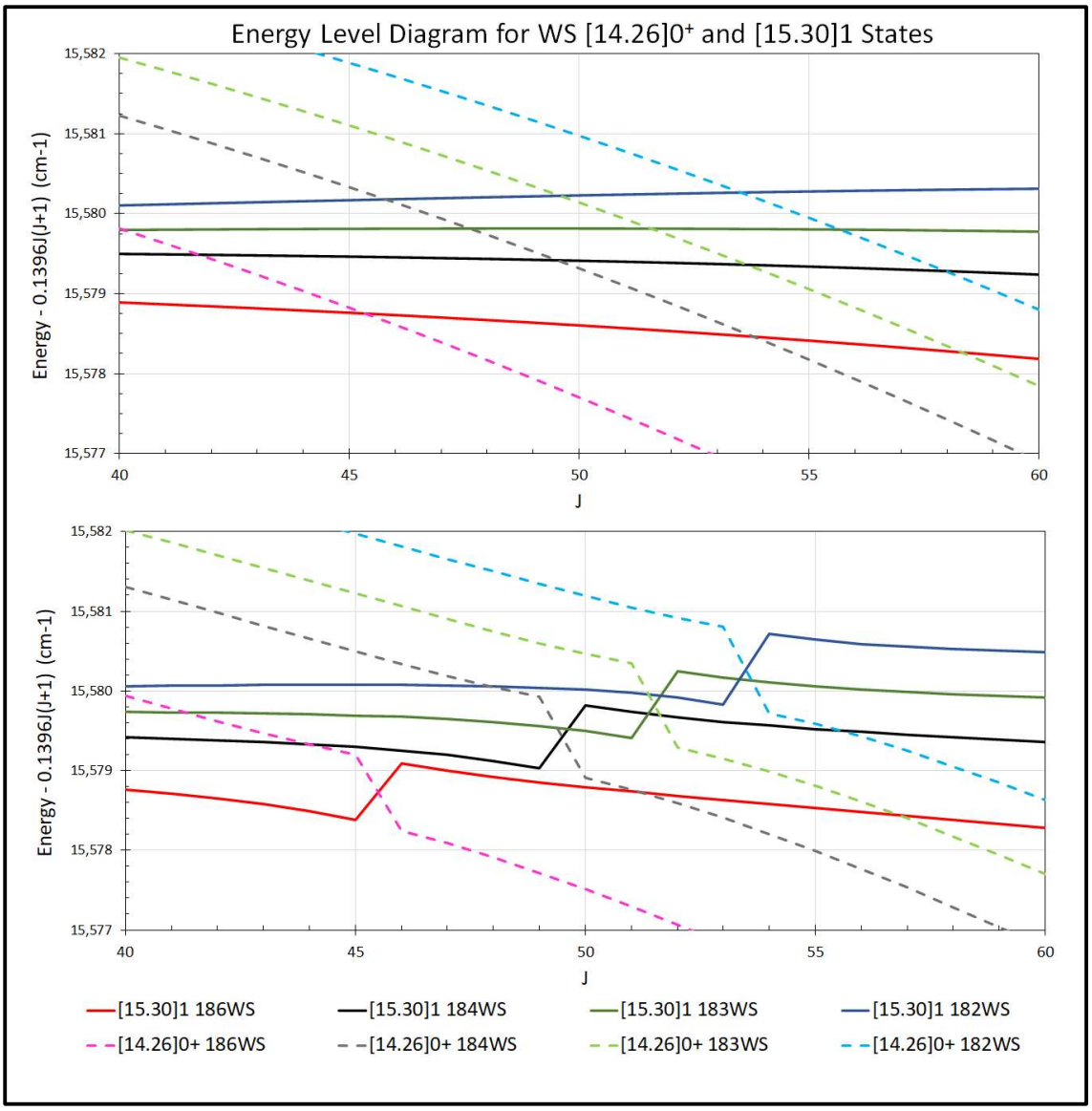

Figure 4.7: Reduced energy level diagram showing the energy level crossing region of v = 2 of $[14.26]0^+$ and v = 0 of [15.30]1 states of WS. The ^{186}WS isotopologue energy levels cross at J″ = 45, whereas the ^{182}WS isotopologue levels cross at J″ = 53. The top panel (A) shows the level crossing with no perturbation effect simulated, while the bottom panel (B) illustrates the effect of the perturbation on the energy levels of each state. The approximate B value of the v = 0 of [15.30]1 state, 0.1396 cm^{-1}, multiplied by J(J+1) is subtracted from the overall energy of each state to allow easier visualization of the interactions.

Initial fitting of the perturbation was done on a band-by-band basis, with each isotopologue fit independently to its own set of parameters for each of the two electronic states. Included in the fit were lines from the (0,0), (1,0) and (1,1) bands of

the [15.30]1 – X(0^+) transition, as well as lines from the (1,0), (0,1), (1,2), (2,0), (2,1), and (3,0) bands of the [14.26]0^+ – *X*(0^+) transition. The (1,0), (0,1), (1,2) band lines from the [14.26]0^+ transition were taken from the previous analysis.[54] Line positions from our analysis of the (1,0) band of the [13.10]1 – X(0^+) transition[53] as well as LIF line positions for the [12.37]1 – X(0^+) and [13.10]1 – X(0^+) transitions provided by Tsang *et al.*[39] were included to aid fitting accuracy of the ground state. Line assignments in the heavily perturbed portions of the spectrum were made with the aid of PGOPHER[8] models, and assignments were verified using Δ_2F values.[4] Because the upper state J′ of any line R(J″) is the same as that of P(J″+2), an R-branch line will be perturbed in the same direction and with the same magnitude as its corresponding P-branch line at J″+2. Using this concept, all assignments for perturbed lines were made in pairs, with corresponding lines compared to the expected unperturbed location from the initial PGOPHER[8] simulation. This was particularly important in the heavily congested R-branch portion of the spectrum, where a corresponding P line (which was in a much less congested area of the spectrum) was required to verify line assignments. Also identified were 428 line positions from the perturbing [14.26]0^+ state, further supporting the assignments.

Following successful band-by-band fitting of the experimental data, a fully mass-independent Dunham[5] fit was attempted. The constrained variables approach introduced by Breier and coworkers[9] and used by our group to model the *X*(0^+) ground state of WS,[54] was used here for the ground state as well as the [14.26]0^+ and [15.30]1 states. The reference isotopologue in this analysis was the central $^{184}W^{32}S$, with the $Y_{l,m}$

Dunham parameters for the other three abundant species calculated from the central isotopologue using the relevant mass scaling.[9,54,58]

With a working Dunham model in place, parameters for the two interacting states could be extrapolated to attempt to include the v = 2 vibrational level of [15.30]1. The (2,0) band of the [15.30]1 – X(0^+) transition appears as a set of irregular and relatively weak bandheads appear in the spectrum near 16,340 cm^{-1}. The bandhead portion of the spectrum is shown in Figure 4.8. A similar set of bandheads is located within the spectrum of the (1,0) band near 15,784 cm^{-1} and corresponds to the (2,1) band. The irregular appearance of the bandheads does not follow the expected evenly spaced four-bandhead cluster associated with the four abundant WS isotopologues, indicating further perturbation by the [14.26]0^+ state, this time by v = 4. The modified Dunham[5] model previously used to describe the two electronic states aided in the deperturbation of the (2,0) band by providing a reasonable prediction of the parameters associated with the two vibrational levels involved. In the initial fit, deviation from the Dunham[5] model was allowed via ΔT parameters used to independently adjust the term energies of each isotopologue, so determination of the term energies for the new vibrational levels provided the greatest challenge. Fortunately, strong, unperturbed Q-branches of both the (2,0) and (2,1) bands provided a reliable reference for the origins of the four isotopologues of the [15.30]1 state, however, the exact band origins of the isotopologues in v = 4 of the [14.26]0^+ state must be determined through characterization of the effects of the perturbation.

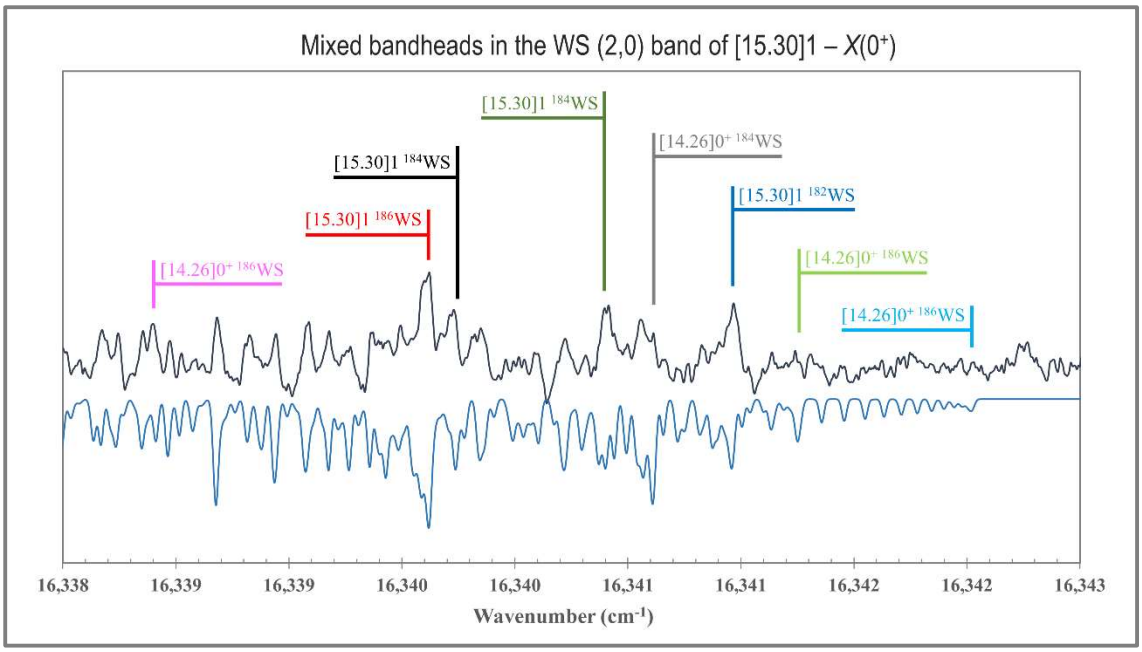

Figure 4.8: Irregularly spaced bandhead positions for the four abundant isotopologues of WS in the perturbed (2,0) band of the [15.30]1 – X(0^+) transition, with the experimental ILS-FTS spectrum in black, and the PGOPHER simulation in blue, below. The bandheads for ^{182}WS and ^{186}WS in the [14.26]0^+ – X(0^+) transition are much weaker and less visible in the spectrum due to having a smaller perturbation effect at the rotational levels associated with the bandhead region, and the bandhead for ^{183}WS, while more heavily perturbed, is barely visible due to a lower natural abundance of the ^{183}WS isotopologue.

Upon initial fitting of the Q-branch, the predicted R-branch bandhead for an unperturbed ^{186}WS appeared in the simulated PGOPHER[8] spectrum approximately 0.15 cm^{-1} lower in energy than the observed bandheads in both the (2,0) and (2,1) bands. An L-uncoupling interaction results in the higher energy level being pushed up, while the lower energy level is pushed down until the two levels cross, where the effect is reversed. Therefore, the perturbing ^{186}WS v = 4 of [14.26]0^+ must be lower in energy and pushing lines for v = 2 of [15.30]1 to slightly higher energy. However, the initial simulated bandhead for ^{182}WS appeared at higher energy than what was observed in the experimental spectrum, indicating that for this isotopologue, the perturbing state is

higher in energy than the [15.30]1 state. The difference in apparent perturbation effect among isotopologues shows that the origins of the vibrational levels of the two states are very similar in energy, and that the levels cross near or on opposite sides of the ~R(20) bandhead position. The final analysis shows that for the ^{186}WS isotopologue, the energy levels of the two states do not cross at all, and v = 4 of [14.26]0^+ has an origin just below that of v = 2 of the [15.30]1 state. The larger spacing among isotopologues of the v = 4 perturber leads to v = 4 of [14.26]0^+ of ^{182}WS lying higher in energy than the [15.30]1 v = 2, resulting in an energy level crossing near J′ = 27. The intertwined energy levels of the two states are illustrated in the reduced energy level diagram shown as Figure 4.9. From the figure, we see that the ^{183}WS and ^{184}WS isotopologues show an energy level crossing at J′ = 23 and J′ = 18, respectively, which is very near the rotational level at which the R-branch turns back to produce a distinct bandhead. The effect of an L-uncoupling perturbation is strongest for rotational levels near the crossing point,[59] and part of the effect is a mixing of transition intensities. This gives enhanced intensity to heavily perturbed lines from the (4,0) band of the [14.26]0^+ – X(0^+) transition which would be too weak to observe. Thus, because the energy level crossings for the ^{183}WS and ^{184}WS isotopologues occur near the J′ of the R-branch bandheads, the bandheads appear to be split in the spectrum, with a weak bandhead appearing for each of the transitions.

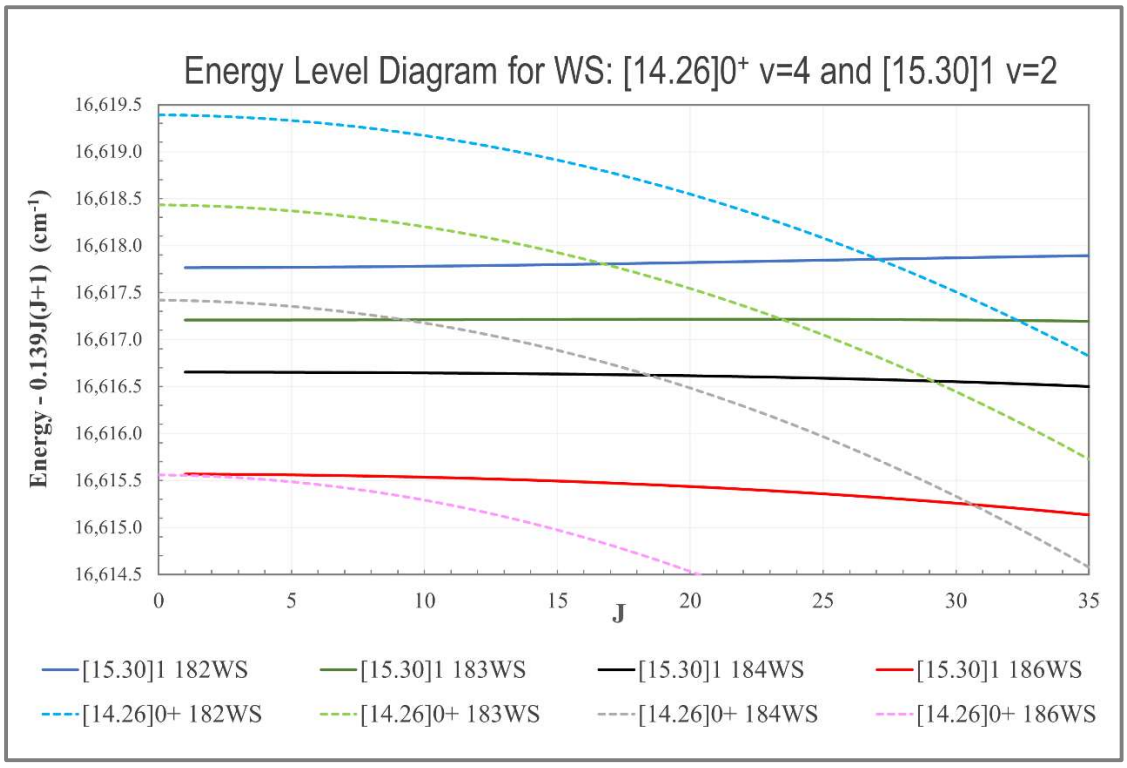

Figure 4.9: Reduced energy level diagram showing the relative positions of the origins and energy level crossings of each isotopologue for [14.26]0^+ v = 4 and [15.30]1 v = 2, with no perturbation effect added.

Due to small but significant deviations in the expected vibrational term energies, ΔT parameters were incorporated into the fitting model to decouple the isotopologue-dependent T_v values from the Dunham expansion. These take the form:

$$\mathrm{Origin_v} = Y_{00} + Y_{10} + Y_{20} + \ldots + \Delta T_\mathrm{v} \tag{4.1}$$

$$\mathrm{B_v} = Y_{01} + Y_{11} + Y_{21} + \ldots \tag{4.2}$$

$$\mathrm{D_v} = Y_{02} + Y_{12} + Y_{22} + \ldots \tag{4.3}$$

where the Y_{lm} are the traditional Dunham parameters that fit the form

$$\mathrm{Y}^{\mathrm{i}}_{l,m} = \mathrm{Y}^{\mathrm{p}}_{l,m}\left(\frac{\mu_\mathrm{p}}{\mu_\mathrm{i}}\right)^{\frac{l}{2}+m} \tag{4.4}$$

which allows for mass-scaling as was described in Section 1.2. These parameters describe the rovibrational structure of an ideal potential energy curve according to

$$T_{vJ}^{i} = Y_{lm}^{i}\left(\mathrm{v}+\frac{1}{2}\right)^{2}[\mathrm{J}(\mathrm{J}+1)]^{m} \tag{4.5}$$

The ΔT_{v} parameter in Equation 4.1 indicates the magnitude of the deviation from the expected mass scaling shown in Equation 4.4. These ΔT parameters decouple the isotopologue specific T_{v} values from the mass-dependent scaling of the vibrational Y_{10}, Y_{20}, … parameters predicted by the Dunham model. Consequently, they can be used to evaluate how well the Dunham model describes the "unperturbed" state, with an ideal state having ΔT values near 0. The ΔT parameters used with the Dunham[5] model in our previous work[57] have been mass-constrained to reduce the number of required parameters. For the [15.30]1 state's v = 0–2 and the [14.26]0^{+} v = 0–3, the central ^{184}WS isotopologue was constrained with $\Delta T = 0$, so that the Origin parameter for this isotopologue is determined by the Dunham[5] model. The ΔT parameters for the other three isotopologues were constrained to expected mass relationships. The ΔT parameter for ^{182}WS (ΔT_{182}) was allowed to float in the fit, while ΔT for ^{183}WS and ^{186}WS were constrained as:

$$\Delta T_{183} = (0.50)\Delta T_{182} \tag{4.6}$$

$$\Delta T_{186} = (-0.979)\Delta T_{182} \tag{4.7}$$

The coefficients in Equations 4.6 and 4.7 are added to the ΔT parameter according to the expected proportion and direction of the vibrational isotopologue shift from the central reference isotopologue, and are determined as in Equation 4.8:

$$\frac{(1-\rho_{186})}{(1-\rho_{182})} = -0.979 \tag{4.8}$$

where ρ is the square root of the reduced mass of the reference isotopologue divided by the reduced mass of the minor isotopologue denoted by the number in the subscript and $(1-\rho)$ gives the expected vibrational shift of each minor isotopologue from the reference isotopologue. In this way, the central isotopologue is fixed to the Dunham[5] model, while the term energies of the other three isotopologues are evenly spread from that central position. However, due to the greater uncertainty in term energies for [14.26]0^+ v = 4 caused by a limited number of observable line positions, all four isotopologues for this vibrational level were decoupled from the Dunham[5] model with independent ΔT parameters for each.

Λ-doubling parameters for the [15.30]1 state, q_v and q_{Dv} were incorporated into the Dunham model. They were constrained to follow the known mass relationships:[58]

$$q_v^i = q_v^p \left(\frac{\mu_p}{\mu_i}\right)^2 \tag{4.9}$$

$$q_{D_v}^i = q_v^p \left(\frac{\mu_p}{\mu_i}\right)^3 \tag{4.10}$$

where the superscript *i* refers to a minor isotopologue, and the superscript *p* refers to the reference isotopologue, $^{184}W^{32}S$, and μ is the reduced mass.

The bandhead region of the experimental spectrum for the perturbed (1,0) band of the [15.30]1 – X(0^+) transition, along with the PGOPHER[8] simulation, is shown in Figure 4.10. The final fit resulted in an average error of 0.004 cm^{-1} for 6,175 total line positions fit to 65 parameters, which included the states analyzed in Section 4.4. The

determined Dunham fit parameters for the $X0^+$, $[14.26]0^+$, and [15.30]1 states, L-uncoupling values, and the ΔT and Λ-doubling parameters, are given in Table 4.3 - Table 4.6, with Table 4.3 including a comparison of values for the current analysis to the previous set of Dunham parameters determined for the ground state.[54]

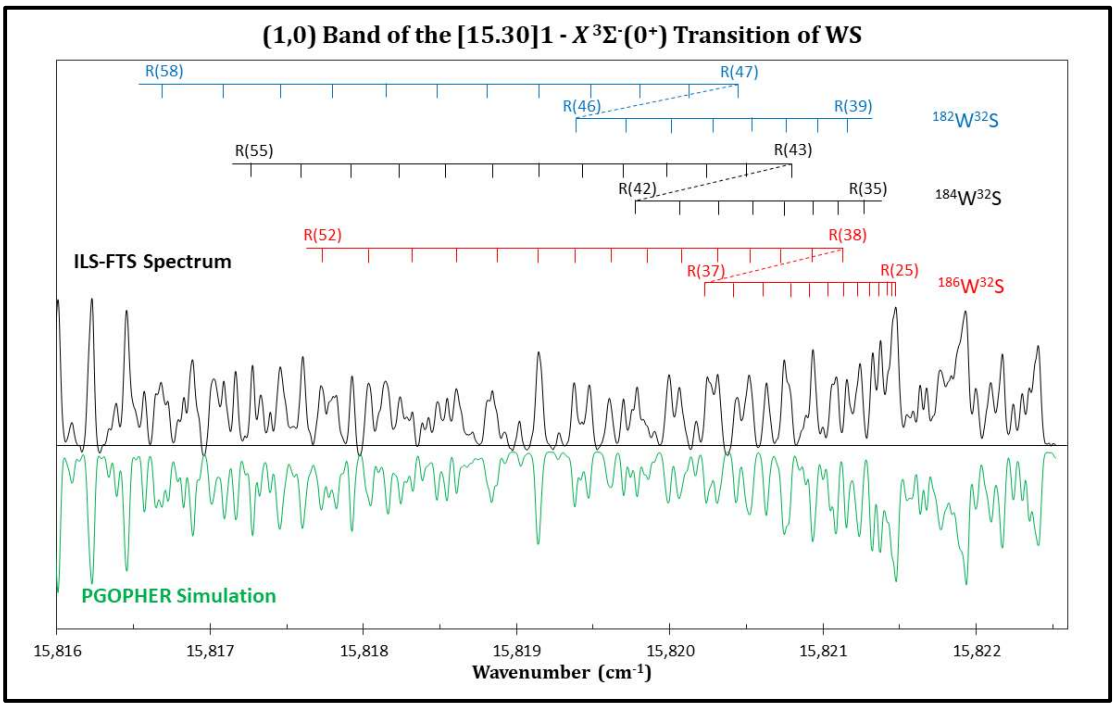

Figure 4.10: A portion of the experimental ILS-FTS spectrum for the (1,0) band of the [15.30]1 – $X(0^+)$ transition (black), with inverted PGOPHER simulation (green) for comparison. A temperature of 600 K and a Gaussian linewidth of 0.025 cm^{-1} were used in the simulation. At the right side of the figure, four distinct bandheads are observable, due to the vibrational shift among the four major isotopologues: $^{186}W^{32}S$, $^{184}W^{32}S$, $^{183}W^{32}S$, and $^{182}W^{32}S$, with the bandhead corresponding to $^{182}W^{32}S$ appearing furthest to the right. Also shown are line positions for the perturbed R-branch of each of the three most abundant isotopologues in the region where energy levels for the two interacting [15.30]1 and $[14.26]0^+$ states cross and cause a sudden shift to higher energy within the branch.

Table 4.3: Dunham parameters for the X $^3\Sigma^-(0^+)$ state of WS. Parameters from this work are presented in regular typeface and parameters from our previous work are presented in *red italics*. Uncertainties are provided as (1σ). Here, the fitting uncertainty applies to $^{184}W^{32}S$, and the uncertainties for the other isotopologues are determined from those values. All values are in cm^{-1}.

$X\ ^3\Sigma^-(0^+)$	$^{182}W^{32}S$	$^{183}W^{32}S$	$^{184}W^{32}S$	$^{186}W^{32}S$
Y_{00}	0[a]	0[a]	0[a]	0[a]
Y_{10}	560.87203 (64) *560.92910 (28)*	560.64242 (64) *560.69947 (28)*	560.41552 (64) *560.47255 (28)*	559.96833 (64) *560.02531 (28)*
Y_{20}	-1.84375 (25) *-1.87292 (14)*	-1.84224 (25) *-1.87139 (14)*	-1.84075 (25) *-1.86987 (14)*	-1.83781 (25) *-1.86689 (14)*
Y_{01}	0.1452877 (14) *0.14529778 (79)*	0.1451688 (14) *0.14517884 (79)*	0.1450513 (14) *0.14506135 (79)*	0.1448199 (14) *0.14482994 (79)*
$Y_{11} \times 10^3$	-0.53139 (31) *-0.5572 (18)*	-0.53073 (31) *-0.5565 (18)*	-0.53009 (31) *-0.5558 (18)*	-0.52882 (31) *-0.5545 (18)*
$Y_{21} \times 10^3$	- *0.00826 (61)*	- *0.00825 (61)*	- *0.00824 (61)*	- *0.00821 (61)*
$Y_{02} \times 10^6$	-0.03904 (20) *-0.037964 (88)*	-0.03897 (20) *-0.037902 (87)*	-0.03891 (20) *-0.037841 (87)*	-0.03879 (20) *-0.037720 (87)*
$Y_{12} \times 10^9$	-0.318 (62) *-0.152 (16)*	-0.318 (62) *-0.152 (16)*	-0.317 (62) *-0.152 (16)*	-0.316 (62) *-0.151 (16)*
$Y_{03} \times 10^{12}$	0.0062 (98) *-0.0263 (68)*	0.0062 (98) *-0.0262 (67)*	0.0062 (98) *-0.0261 (67)*	0.0062 (98) *-0.0260 (67)*

[a]Held fixed in the fit.

Table 4.4: Dunham parameters for the [14.26]0^+ and [15.30]1 states of WS. Fitting uncertainties are provided as (1σ), and uncertainty applies to ^{184}WS. Uncertainties for the remaining isotopologues are determined from those values. All values are in cm^{-1}.

[14.26]0^+	**^{182}WS**	**^{183}WS**	**^{184}WS**	**^{186}WS**
Y_{00}	14,282.22104 (51)	14,282.22104 (51)	14,282.22104 (51)	14,282.22104 (51)
Y_{10}	523.566380 (60)	523.352045 (60)	523.140235 (60)	522.722788 (60)
Y_{20}	-0.86794 (34)	-0.86723 (34)	-0.86653 (34)	-0.86515 (34)
Y_{30}	-0.01255 (11)	-0.01254 (11)	-0.01252 (11)	-0.01249 (11)
Y_{01}	0.1389637 (15)	0.1388500 (15)	0.1387376 (15)	0.1385163 (15)
$Y_{11} \times 10^3$	-0.42976 (70)	-0.42923 (70)	-0.42871 (70)	-0.42768 (70)
$Y_{21} \times 10^6$	-1.12 (15)	-1.12 (15)	-1.12 (15)	-1.12 (15)
$Y_{02} \times 10^9$	-40.73 (20)	-40.67 (20)	-40.60 (20)	-40.47 (20)
$Y_{12} \times 10^9$	1.409 (98)	1.406 (98)	1.403 (98)	1.397 (98)
[15.30]1	**^{182}WS**	**^{183}WS**	**^{184}WS**	**^{186}WS**
Y_{00}	15,320.13528 (54)	15,320.13528 (54)	15,320.13528 (54)	15,320.13528 (54)
Y_{10}	519.08156 (85)	518.86907 (85)	518.65907 (85)	518.24520 (85)
Y_{20}	-0.01938 (33)	-0.01937 (33)	-0.01935 (33)	-0.01932 (33)
Y_{01}	0.1400362 (15)	0.1399215 (15)	0.1398083 (15)	0.1395853 (15)
$Y_{11} \times 10^3$	-0.33252 (50)	-0.33211 (50)	-0.33171 (50)	-0.33092 (50)
$Y_{21} \times 10^6$	-11.65 (18)	-11.63 (18)	-11.61 (18)	-11.57 (18)
$Y_{02} \times 10^9$	-30.65 (21)	-30.60 (21)	-30.55 (21)	-30.45 (21)
$Y_{12} \times 10^9$	-1.659 (31)	-1.655 (31)	-1.652 (31)	-1.645 (31)
$Y_{03} \times 10^{12}$	-0.030 (11)	-0.030 (11)	-0.030 (11)	-0.030 (11)

Table 4.5: Magnitude of ΔT parameters for the [14.26]0^+ and [15.30]1 states of WS. For v = 4 of [14.26]0^+, the vibrational energy is completely decoupled from the Dunham model and the ΔT for each isotopologue in that vibrational level is fit independently with no mass constraint. For all vibrational levels, the central isotopologue, ^{184}WS, is fit to the Dunham model, with ΔT values of minor isotopologues indicating a deviation from the Dunham model. All values are in cm^{-1}.

[14.26]0^+	**^{182}WS**	**^{183}WS**	**^{184}WS**	**^{186}WS**
v = 0	0.03972 (44)	0.01986 (22)	-	-0.03889 (43)
v = 1	0.03291 (27)	0.01646 (14)	-	-0.03222 (26)
v = 2	0.03080 (44)	0.01540 (22)	-	-0.03015 (43)
v = 3	0.0221 (15)	0.01103 (74)	-	-0.0216 (15)
v = 4	-0.151 (14)	-0.162 (17)	-0.235 (15)	-0.247 (14)
[15.30]1	**^{182}WS**	**^{183}WS**	**^{184}WS**	**^{186}WS**
v = 0	0.03162 (27)	0.01581 (14)	-	-0.03095 (27)
v = 1	0.04612 (29)	0.02306 (14)	-	-0.04515 (28)
v = 2	0.05375 (63)	0.02687 (31)	-	-0.05262 (62)

Table 4.6: L-uncoupling operator values for the interactions between WS states [15.30]1 and [14.26]0^+. These values were constrained in the fit to give a single value for all four isotopologues for each pair of vibrational levels.

Interacting States	L-uncoupling Value
[15.30]1 v=0 / [14.26]0^+ v=2	0.0063796 (55)
[15.30]1 v=1 / [14.26]0^+ v=3	0.0102362 (74)
[15.30]1 v=2 / [14.26]0^+ v=4	0.013542 (57)

4.3.3 Discussion

The deperturbation analysis of the (0,0), (1,0), and (2,0) bands of the [15.30]1 – X(0^+) transition was able to model the isotopologue dependent rovibrational structure quite effectively. Experimental observations of the perturbed rotational branches are reproduced by the simulation to experimental accuracy. The Dunham-like model used in the final fit of the observed transitions serves as a second check for the effectiveness of the deperturbation analysis. If the perturbation is modeled effectively, the "ideal" potential energy curves for the interacting states can be approximated. The Dunham model applies to smooth potential energy surfaces, such as those for isolated electronic states. While the electronic structure of WS is quite dense and Hund's case (c) is certainly applicable, if the primary interaction results from only two states then a successful deperturbation should result in potential energy curve that could be well modeled by a Dunham expansion.[5]

A Dunham-like model was used describe the three electronic states involved in the observed transitions: X0^+, [14.26]0^+, and [15.30]1. The obtained parameters are presented in Table 4.3 for the X(0^+) state and Table 4.4 for the excited states. These tables can be used to evaluate the legitimacy of the obtained Dunham potentials. For a given series of Y_{lm} values, we see a sharp decrease in magnitude as l increases, which is

expected for a Taylor series expansion. For example, there are 3 orders of magnitude differences between Y_{01} and Y_{11}, with a further 2 orders of magnitude differences between Y_{11} and Y_{21} for the [14.26]0^+ state. This suggests that the expansion of B_v is converging to zero and that the Dunham parameters are modeling the vibrational dependence of the rotational constant effectively. We can also evaluate whether known relationships between other parameters are preserved. The Kratzer relationship[4] shown as Equation 1.12, can be rewritten to give the expected relationship between Y_{02}, Y_{01}, and Y_{10}:

$$D = \frac{4B^3}{\omega_e{}^2} \rightarrow Y_{02} = \frac{4Y_{01}^3}{Y_{10}^2} \tag{4.11}$$

Calculating an expected Y_{02} from experimentally determined values of Y_{01} and Y_{10} for $^{184}W^{32}S$ of the [14.26]0^+ state, we find a value of -3.89×10^{-8} cm^{-1}, which compares to the fit Y_{02} parameter of -3.87×10^{-8} cm^{-1}. A similar comparison for the [15.30]1 state finds a calculated Y_{02} value of -4.06×10^{-8} cm^{-1} and a fit value of -2.97×10^{-8} cm^{-1}. While there is a larger discrepancy between these two latter values, the difference is reasonable due to the slightly larger uncertainty in the Y_{10} value. Because the v = 4 level of [14.26]0^+ is fit largely by means of observation of the perturbation, a change in the magnitude of the perturbation would affect the term energy of the [14.26]0^+ vibrational level, term energy of the [15.30]1 vibrational level and the perturbation, adding some uncertainty to all three values. A similar comparison may be made using the Pekeris relationship[4]

$$Y_{20} = -Y_{01}\left(\frac{-Y_{11}Y_{10}}{6Y_{01}^2} + 1\right)^2 \quad \rightarrow \quad \omega_e\chi_e = B_e\left(\frac{\alpha_e\omega_e}{6B_e^2} + 1\right)^2 \tag{4.12}$$

where the calculated value for Y_{20} of –1.15 cm^{-1} compares quite favorably to the fitted value of –1.18 cm^{-1}. These relationships indicate that the deperturbation analysis was quite effective in producing "ideal" unperturbed potential energy wells of the two interacting states.

The initial experimental analysis of the [14.26]0^+ state by our group described the v = 0 and v = 1 vibrational levels[54] and was extremely valuable in providing accurate predictions for parameters of the v = 2 vibrational level. This deperturbation analysis would have been difficult if not impossible without these initial values which were used early in the analysis to model perturbation effects and assist with line assignments in the heavily perturbed regions. Extrapolating from the v = 0 and v = 1 levels provided a T_2 value roughly 1 cm^{-1} from the experimentally determined value, and a provisional B_2 value that was within 2×10^{-5} cm^{-1} of the determined value. The consistency observed here provides further validation that the assignment of the perturbing states are correct.

The earlier analysis of the [15.30]1 transition by Zhang, *et al.*[52] was limited by the low experimental temperature used in LIF measurements which allowed inclusion of only low-J lines. This limitation prevented observation of the perturbation at higher J and only one isotopologue, $^{184}W^{32}S$, was able to be characterized. However, our results do show good agreement to the previous findings, with our T_0 and B_0 values falling within their experimental error. The main difference between the two studies' findings is in the determination for D_0, in which the previously determined value[52] is negative. Our positive D_0 value is more plausible, as D is the centrifugal distortion constant and is used to account for the increase in bond length and moment of inertia experienced by

the molecule as rotational velocity increases. A negative D value would suggest a decreasing bond length with increasing rotational energy.

Additional comparisons can be made to the *ab initio* results given by Tsang *et al.*[39] Predicted equilibrium constants are compared to the corresponding experimentally determined values for the central $^{184}W^{32}S$ isotopologue from the current work in Table 4.7. Here, the label given to the *ab initio* electronic states is determined by rank of a given Ω-value, i.e., $\{5\}0^+$ is fifth highest $\Omega=0^+$ state predicted. Correlation between experimental and *ab initio* states is based heavily upon B_e and ω_e values due to the difficulty in prediction of term energy (T_e) among a dense population of states. While the relative ordering of the levels tends to be well-predicted, a somewhat regular correction to the energy value must often be applied. Previous works[39,54,55] have correlated the $[14.26]0^+$ state to the *ab initio* $\{5\}0^+$ state, however, we find that aside from a larger discrepancy in T_e, the $\{6\}0^+$ state is a better fit for all other determined constants. In addition, this work has the added benefit of giving more insight into the Λ-S character of the involved states due to the selection rules associated with perturbation effects. As previously mentioned, an L-uncoupling interaction requires that the two perturbing states have $\Delta S=0$, $\Delta\Omega=\pm1$ and $\Delta\Lambda=\pm1$. The $[15.30]1$ state, correlated to the *ab initio* $\{10\}1$, is expected to be predominantly $^3\Sigma^-$ (55%) in character, while $\{5\}0^+$ and $\{6\}0^+$ are predicted to be $^5\Delta$ (76%) and $^3\Pi$ (85%), respectively.[39] Re-assigning the $[14.26]0^+$ state to $\{6\}0^+$ would satisfy the selection rules for the perturbation which allow interaction to occur.

Table 4.7: Equilibrium constants for $^{184}W^{32}S$ determined by this work (regular typeface) and by *computational prediction*[39] *(red italics)*. While previous works correlated the $[14.26]0^+$ state to $\{5\}0^+$, we suggest a re-assignment to $\{6\}0^+$.

$^{184}W^{32}S$	T_e (cm^{-1})	B_e (cm^{-1})	r_e (Å)	ω_e (cm^{-1})	$\omega_e\chi_e$ (cm^{-1})
$[14.26]0^+$	14,282	0.1387	2.112	523	1.2
{5}0^+	*14,464* [a]	*0.1339* [a]	*2.152* [a]	*506* [a]	*7.7* [a]
{6}0^+	*15,269* [a]	*0.1375* [a]	*2.122* [a]	*526* [a]	*2.3* [a]
[15.30]1	15,320	0.1398	2.104	519	-
{10}1	*17,108* [a]	*0.1380* [a]	*2.116* [a]	*559* [a]	*5.7* [a]

[a] Ref [39]

4.3.4 Conclusions

Although both states have been described previously in the literature, the availability of high-resolution spectra at sufficient temperature for observation of high J lines has allowed this analysis to provide a significant addition to our understanding of the $[14.26]0^+$ and [15.30]1 states of WS. Lines from all four abundant isotopologues of WS were observed in the (0,0) and (1,0) bands of the [15.30]1 – $X(0^+)$ transition, which were rotationally analyzed using PGOPHER.[8] Because these bands were significantly perturbed by a nearby electronic state, this analysis also provides insight into the interaction of two states in an electronically complex molecule. The two bands were shown to be perturbed by the v = 2 and v = 3 vibrational levels of the $[14.26]0^+$ state, of which the v = 0 and v = 1 levels were analyzed by our group in a prior work.[54] Parameters predicted from the previous work, as well as lines observed for the (2,0), (2,1), and (3,0) bands of the $[14.26]0^+$ – $X(0^+)$ transition aided in completion of a deperturbation analysis. This resulted in the determination of an L-uncoupling parameter for each interaction. The deperturbation analysis used the constrained-variables approach from Breier *et al.*[9] to fit the [15.30]1, $[14.26]0^+$, and $X(0^+)$ states to

a mass-independent Dunham[5] model in PGOPHER.[8] An additional parameter, labeled ΔT, was included as needed to decouple the vibrational energies of the minor isotopologues of the [15.30]1 state and all isotopologues of the [14.26]0^+ state from the Dunham model. Finally, examination of equilibrium constants as well as the predicted Λ-S character of the two perturbed states resulted in a re-assignment of the [14.26]0^+ state to the *ab initio* $\{6\}0^+$ state.

4.4 Transitions of the [13.10]1 and [15.30]1 States Near 13,000 cm^{-1}

With the completion of the deperturbation analysis of the [15.30]1 state, we were able to finally complete the analysis of the (0,0) band of the [15.30]1 – X(0^+) transition, which had begun four years prior, to determine the spin-spin splitting of the X $^3\Sigma^-$ ground state. The analysis of the new transition, observed using ILS-FTS and analyzed using PGOPHER,[8] supports further the validity of the prior deperturbation analysis. The high resolving power, rotationally excited populations of molecules observed, and the comprehensive modeling of rotational structure give a more precise value for the origin of the X(1) state. In addition, this work includes analysis of the nearby (0,0) band of the [13.10]1 – X(0^+) transition, originally reported by Tsang *et al*.[39] Results for this study have been submitted to the Journal of Molecular Spectroscopy.

4.4.1 Experimental Methods

The experimental spectra were collected using the ILS-FTS system. Spectra in the visible region (15,750 – 16,350 cm^{-1}) were collected via the dye laser ILS system,[20] using DCM laser dye, while those in the near-IR region (12,980 – 13,130 cm^{-1}) were collected using the Ti:Sapphire ILS system.[53] Due to the presence of very strong O_2

lines in the near-IR region of interest, the chamber housing a large portion of the resonance cavity of the Ti:Sapphire system was brought under vacuum and back-filled with Ar to 760 torr immediately prior to data collection to reduce the intensity of the observed O_2 lines to below the point of saturation. The target WS molecules were produced in a reaction chamber located within the resonator cavity of the ILS laser by applying an RF-pulsed DC current of 0.5 – 0.8 A from an ENI RPG-50 plasma generator to a 25 mm (visible region) or 50 mm (NIR region) W-lined Cu hollow cathode in the presence of Ar (70-90%), H_2 (10-30%), and CS_2 (0.1%) gases at a total pressure of 1-2 torr. Specific gas flow composition and plasma discharge currents are varied to maximize the intensity of the observed transition. An ILS generation time (t_g) of 40-90 μsec was used, corresponding to effective pathlengths of at least 0.3 - 1.4 km.

For each transition, a set of FTS scans was collected using a Bruker IFS 125 M Fourier-transform spectrometer at a scan rate of 5-20 kHz and an instrument resolution of 0.01-0.02 cm^{-1}. For each laser profile position, a set of 4 coadded FTS scans was collected in the presence of the plasma discharge, and another set of background spectra was collected with no discharge present. The partially overlapping experimental spectra were coadded, as were the background spectra, to obtain a single experimental spectrum and a single background. The summative experimental spectrum was then divided by the corresponding background spectrum. Division of the experimental spectrum by a background was particularly important in the case of the near-IR spectrum near 13,100 cm^{-1} to minimize interference by the previously mentioned O_2 transitions. Addition and division of spectra was accomplished using Bruker's OPUS (v.8.5.29) software. Experimental spectra were baseline corrected and calibrated to

known Ar I[45] and O_2[43] lines using PGOPHER,[8] with final line position uncertainties estimated to be less than 0.002 cm^{-1}.

4.4.2 Analysis and Results

In the near-IR region, a prominent red-degraded bandhead was observed near 13,105 cm^{-1} with a weaker bandhead located near 13,122 cm^{-1}. The bands were consistent with the previously identified (0,0) band of the [13.10]1 – X(0^+) transition[39] and the (0,0) band of the [15.30]1 – *X*(1) transition,[52] respectively. While lines for the [13.10]1 – X(0^+) transition are clearly present to J > 100, with clear separation among the four abundant isotopologues appearing at high J, the weaker band becomes mixed with and partially obscured by the stronger transition beginning at P(30) and R(86). Due to the overlap of spectra, the stronger [13.10]1 – X(0^+) transition was fit with PGOPHER[8] first to verify line positions and assignments, which allowed the remaining lines in this region to be assigned to the [15.30]1 – X(1) transition. The bandhead position of this transition, shown in Figure 4.11, is somewhat camouflaged in our spectra. While the apex of the bandhead is expected to be near 13,122.55 cm^{-1} according to the fit, a predicted Ar I transition[60] appears with relatively high intensity in the spectrum at 13,122.60 cm^{-1}, blending with the edge of the bandhead.

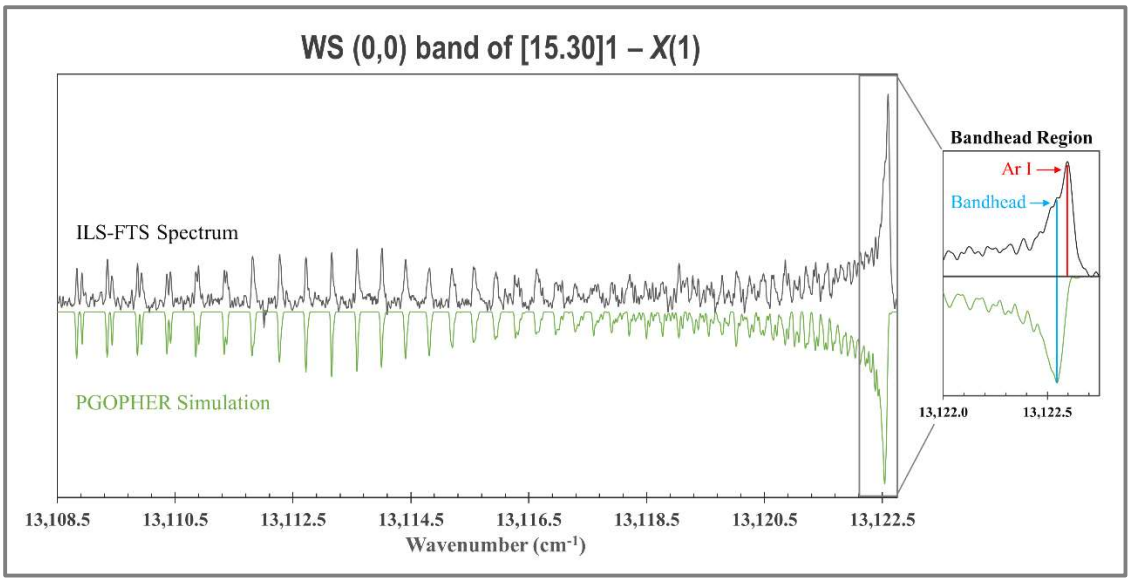

Figure 4.11: The (0,0) band of the [15.30]1 – X(1) transition of WS, with enlarged bandhead region showing overlapping Ar I transition line.

The transition, upon initial inspection, seems to show very distinct Λ-doubling in the P-branch. However, it became clear upon fitting that the unique appearance of the band could be modeled as a perturbation in v = 0 of the [15.30]1 state by the [14.26]0^+ state, which by symmetry can affect only the *e*-levels of the [15.30]1 state. As discussed in Section 4.3, after the energy levels of the two states cross at J′ ~ 50, the [14.26]0^+ state lies lower in energy than the [15.30]1 state, so *e*-levels of the latter are pushed to higher energy, while *f*-levels are unaffected. In the (0,0) band of the [15.30]1 – X(1) transition, the observable effect is that R_e and R_f levels overlap for J′ = 65 – 80 as the rotational energy levels move away from the most heavily perturbed region between J′ = 45 – 55. The apparent doublets in the spectrum are actually due to overlapping P- and R-branches, as shown in Figure 4.12, with some separation of the two P-branches beginning to become apparent at P(29), just before the band is obscured by the neighboring band. Some P-lines of higher J are visible, however, within the [13.10]1 –

$X(0^+)$ transition band, and separate P_e and P_f lines are distinguishable up to $J' \approx 65$ to validate high-J R_e and R_f assignments. The parameters for both the [13.10]1 and X(1) states were fit using a constrained variables approach[9] in PGOPHER,[8] with values for the ^{182}WS, ^{183}WS, and ^{186}WS isotopologues constrained to the determined fit parameters of the central ^{184}WS isotopologue by expected mass relationships. A ΔT parameter was added for each state to fit the vibrational shift in term energy for each isotopologue according to the constraints:

$$T_{v,182} = T_{v,184} + \Delta T \tag{4.13}$$

$$T_{v,183} = T_{v,184} + (0.50)\Delta T \tag{4.14}$$

$$T_{v,186} = T_{v,184} - (0.979)\Delta T \tag{4.15}$$

In Equation 4.13, ΔT gives the deviation (in cm^{-1}) of the origin of the minor isotopologue, $T_{v,182}$, from the origin of the central isotopologue, $T_{v,184}$. The coefficients in Equations 4.14 and 4.15 are added to the ΔT parameter according to the expected proportion and direction of the vibrational isotopologue shift from the central reference isotopologue, and are determined as in Equation 4.16:

$$\frac{(1-\rho_{186})}{(1-\rho_{182})} = -0.979 \tag{4.16}$$

where ρ is the square root of the reduced mass of the reference isotopologue divided by the reduced mass of the minor isotopologue denoted by the number in the subscript, as described in section 4.3.2. The coefficient of 0.50 was determined for the ^{183}WO isotopologue by replacing ρ_{186} in Equation 4.16 with ρ_{183}.

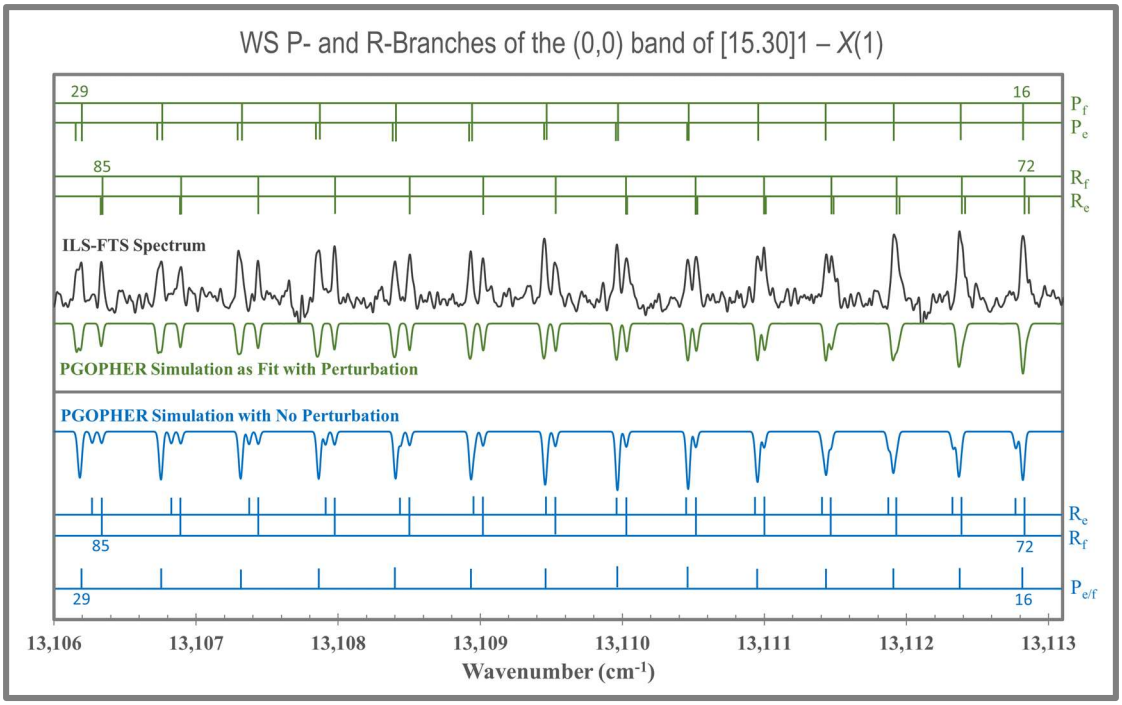

Figure 4.12: P- and R-branch region of the (0,0) band of the WS [15.30]1 – X(1) transition. The experimental ILS-FTS spectrum is in black. Shown in green is the PGOPHER[8] simulation as fit with the L-uncoupling perturbation effect, with line positions marked for P_e, P_f, R_e, and R_f branches. Below, in blue, is the PGOPHER[8] simulation with the L-uncoupling interaction set equal to 0, illustrating the visual effect of the perturbation in the spectrum, with line positions again marked for the four branches. Note that P_f and R_f lines are in the same positions in both simulations since only the *e*-levels are involved in the perturbation.

In total, 486 lines were fit for the (0,0) band of the [15.30]1 – X(1) transition, and 1,163 lines were included in the fit for the (0,0) band of the [13.10]1 – X(0^+) transition. The full data set also included the final fit for the deperturbation analysis in Section 4.2, with ILS line positions from the (0,0), (1,0), (1,1), (2,0), and (2,1) bands of the [15.30]1 – X(0^+) transition, the (1,0) band of the [13.10]1 – X(0^+) transition, and the (1,0), (0,1), (1,2), (2,0), (2,1), (3,2), and (3,0) bands of the [14.26]0^+ – X(0^+) transition, with an average error of 0.004 cm^{-1} for 6,175 total line positions fit to 65 parameters. The parameters determined for the X(1) and [13.10]1 states are given in Table 4.8 and Table 4.9.

Table 4.8: Molecular constants for v = 0 of the X(1) state of WS. Uncertainties given as (1σ). All values are in cm^{-1}.

X(1)	^{182}WS	^{183}WS	^{184}WS	^{186}WS
v = 0				
T_0[a]	2461.1359 (11)[b]	2461.0216 (11)[b]	2460.9073 (11)	2460.6835 (11)[b]
B_0	0.1449104 (16)	0.1447920 (16)	0.1446749 (16)	0.1444444 (16)
D_0 x 10^6	0.04151 (19)	0.04145 (19)	0.04138 (19)	0.04125 (19)
q x 10^3	0.01376 (28)	0.01374 (28)	0.01372 (28)	0.01368 (28)

[a] The minimum of the Dunham potential was set to zero in the fit; thus, all excitation energies include the zero-point energy of each isotopologue.
[b] The T_0 for the ^{184}WS isotopologue was allowed to float in the fit, while the T_0 values for the other three isotopologues were constrained according to Equations 1-3, with a fit ΔT of 0.22860 (69) cm^{-1}.

Table 4.9: Molecular constants for v = 0 and v = 1 of the [13.10]1 state of WS. Uncertainties given as (1σ). All values are in cm^{-1}.

[13.10]1	^{182}WS	^{183}WS	^{184}WS	^{186}WS
v = 0				
T_0[a]	13382.07101 (46)[b]	13381.94778 (46)[b]	13381.82455 (46)	13381.58327 (46)[b]
B_0	0.1383006 (14)	0.1381876 (14)	0.1380758 (14)	0.1378558 (14)
D_0 x 10^6	0.0599 (37)	0.0598 (37)	0.0597 (37)	0.0595 (37)
H_0 x 10^{12}	0.363 (11)	0.362 (11)	0.361 (11)	0.359 (11)
q x 10^3	0.05758 (36)	0.05748 (36)	0.05738 (36)	0.05721 (36)
q_D x 10^9	-1.835 (97)	-1.830 (97)	-1.826 (97)	-1.817 (97)
q_H x 10^{12}	0.0850 (63)	0.0847 (63)	0.0844 (63)	0.0839 (63)
v = 1				
T_1[a]	13813.40469 (52)[b]	13813.12599 (52)[b]	13812.84729 (52)	13812.30160 (52)[b]
B_1	0.1376631 (23)	0.1374383 (23)	0.1372160 (23)	0.1369974 (23)
D_1 x 10^6	0.0595 (18)	0.0593 (18)	0.0592 (18)	0.0590 (18)
H_1 x 10^{12}	-17.52 (49)	-17.47 (49)	-17.43 (49)	-17.35 (49)
q x 10^3	0.0259 (22)	0.0258 (22)	0.0258 (22)	0.0257 (22)
q_D x 10^9	-5.4 (27)	-5.4 (27)	-5.4 (27)	-5.4 (27)
q_H x 10^{12}	28.90 (81)	28.87 (81)	28.85 (81)	28.67 (82)

[a] The minimum of the $X(0^+)$ Dunham potential was set to zero in the fit; thus, all excitation energies include the ground state zero-point energy of each isotopologue.

[b] The T_0 for the ^{184}WS isotopologue was allowed to float in the fit, while the T_0 values for the other three isotopologues were constrained according to Equations 1-3, with a fit ΔT of 0.24646 (23) cm^{-1} for v = 0, and 0.55740 (22) cm^{-1} for v = 1.

4.4.3 Conclusions

This new analysis of the [13.10]1 – X(0^+) and [15.30]1 – X(1) transitions, collected at high temperature within a plasma discharge, allows inclusion of lines from much higher rotational energy levels and offers a more precise characterization of the Ω=1 component of the WS ground state. The inclusion of Dunham models and mass-dependent constraints to fit minor isotopologues adds validity to the fit by minimizing the number of parameters required to describe the states. As expected, we see a large decrease in the magnitude of higher order terms, such as D and H, further increasing confidence in the analysis. In addition, our determined constants compare favorably with those of previous works. For example, our value for the spin-spin splitting in the X $^3\Sigma^-$ ground state of 2,181.1527 cm^{-1} for ^{184}WS agrees with the previously determined value[52] of 2181.10 cm^{-1} within experimental error.

Previous characterizations of v = 0 of the [13.10]1 state and the X(1) state were accomplished using spectra collected at low temperatures[39,52,55] and were thus limited to lines with J < 40, but with inclusion of higher-J lines, our analysis has provided for the first time accurate values for higher order rotational constants and the Λ-doubling constant, q, as well as a more precise value for the spin-spin splitting in the X $^3\Sigma^-$ ground state.

CHAPTER 5:
TUNGSTEN OXIDE (WO)

5.1 Introduction to WO

Tungsten oxides continue to draw research interest in a wide variety of fields due to a host of interesting properties. The electrochromic effect discovered in WO_3 has led to its use in "smart windows" as an energy-saving measure.[61] The conductive properties of nanostructured WO_3 have led to investigation of its use in solar cells and as a photo- and electrocatalyst,[62] and WO_3 nanowires have been used to create gas sensors.[63] In conjunction with the uses of WO_3 as a bulk or nanostructured material, the diatomic WO is an interesting spectroscopic target due to the complex electronic structure of the transition metal bond, as this type of investigation can increase our understanding of the properties of the W-O bond at a fundamental level as well as aid in future computational work by providing benchmark data.

Several previous spectroscopic works on WO have been completed. Weltner and McLeod[64] observed and proposed vibrational assignments for several bands in the 17,000 – 27,000 cm^{-1} range. They also implemented the A-G labeling scheme for the 7 associated excited electronic states that has since been widely used. Samoilova *et al.*[65] provided the first rotational analyses for WO spectra in 1981, and in 1997, Kuzyakov *et al.*[66] suggested corrections to the earlier vibrational assignments for bands in the A1 – $X0^+$ transition. Ram *et al.*[67] determined in 2001 that the WO ground state is $^3\Sigma^-$, then followed that work with perhaps the most comprehensive study to date in 2009[68] with rotational analyses of many bands observed in the 4,000 – 35,000 cm^{-1} region, as well as *ab initio* calculations of low-lying electronic states. A common theme throughout

these previous works is a discussion on the heavily perturbed nature of many of the excited electronic states of WO and particularly between the A1 and B1 states, with anomalous isotope shifting causing disagreement in the A1 – $X0^+$ vibrational band assignments.

In this work we have used spectra collected using intracavity laser absorption spectroscopy (ILS) to improve upon the previous rotational analyses[65-68] of the (0,0) and (0,1) bands of the A1 – $X0^+$ and B1 – $X0^+$ transitions by incorporating all four abundant W isotopologues: $^{182}W^{16}O$ (26.5%), $^{183}W^{16}O$ (14.3%), $^{184}W^{16}O$ (30.6%), and $^{186}W^{16}O$ (28.4%). The rotational analysis was done using a constrained-variables approach in PGOPHER[8] to maintain expected mass relationships among rotational parameters, and an avoided crossing interaction between the A1 and B1 states has been modeled with homogeneous perturbations. The deperturbation analysis significantly decreases the overall number of rotational parameters required to describe the two states. The results of this analysis are being prepared for submission to the Journal of Molecular Spectroscopy.

5.2 Experimental Method

The spectra used for this analysis were collected using the DL ILS system. The (0,0) bands near 17,100 cm^{-1} were collected using Rhodamine-6G laser dye and Dispersed ILS[18] with a resolution of roughly 0.035 cm^{-1}. The (0,1) bands near 16,100 cm^{-1} were collected using DCM laser dye and ILS-FTS,[20] with the instrument resolution set to 0.015 – 0.03 cm^{-1} depending upon the level of congestion among lines in each portion of the spectrum. Target molecules were produced via plasma discharge

in a reaction chamber within the resonance cavity of the ILS dye laser by applying an RF-pulsed DC current of 0.40 – 0.80 A from an ENI RPG-50 plasma generator to a tungsten-lined copper hollow cathode in the presence of Ar (90%), H_2 (10%), and O_2 (trace) at a total pressure of 1.25 torr. The spectra collected using Dispersed ILS were calibrated by collecting a spectrum of I_2 from an extra-cavity cell at each monochromator position, immediately following the experimental spectrum (plasma discharge on) and a background spectrum (no plasma discharge). The experimental and I_2 spectra were divided by the background spectra, and each I_2 spectrum was then calibrated to reference data from Salami and Ross[41] to an estimated wavenumber accuracy of ±0.005 cm^{-1}, with the same calibration then being applied also to the experimental spectra. The (0,1) bands, collected using the ILS-FTS system, were calibrated to Ar I lines[44,60] with an estimated accuracy of ±0.002 cm^{-1}.

5.3 Analysis and Results

Both the (0,0) and (0,1) bands of the A1 – $X0^+$ and B1 – $X0^+$ transitions appeared in the spectra with good intensity, with the A1 transition bands overlapped by the B1 bands. Both also show clear lines up to $J'' \geq 50$, with lines for the unobstructed A1 transitions distinguishable to much higher J. Also observed in the spectra are the peculiar isotope shifts noted in previous works[64-68] which have been the cause of much disagreement regarding vibrational assignments of the bands associated with the A1 state. Figure 5.1 (A) shows the bandhead region of the (0,0) band of the A1 transition, with a ~0.6 cm^{-1} shift between ^{182}WO-^{184}WO-^{186}WO, while Figure 5.1 (B) shows the (0,0) band of the B1 transition, with a corresponding bandhead shift of ~0.8 cm^{-1}. It also was noted that

in the most recent set of rotational parameters determined by Ram *et al.*,[68] the values for v = 0 of the A1 and B1 states were intriguingly odd in that the D values were significantly larger than for other determined states and were not consistent with the Kratzer relation.[6] The D_0 for A1 was large and positive, while the D_0 for B1 was large and negative. Additionally, many higher order parameters were required to fit a relatively modest number of rotational levels, reinforcing suggestions by Ram[68] and others[64-66] that the states interact and that fit parameters did not give a true representation of the nature of the electronic states. Thus, the aim of this work was to perform a deperturbation analysis of the A1 and B1 states to obtain a more reasonable set of parameters.

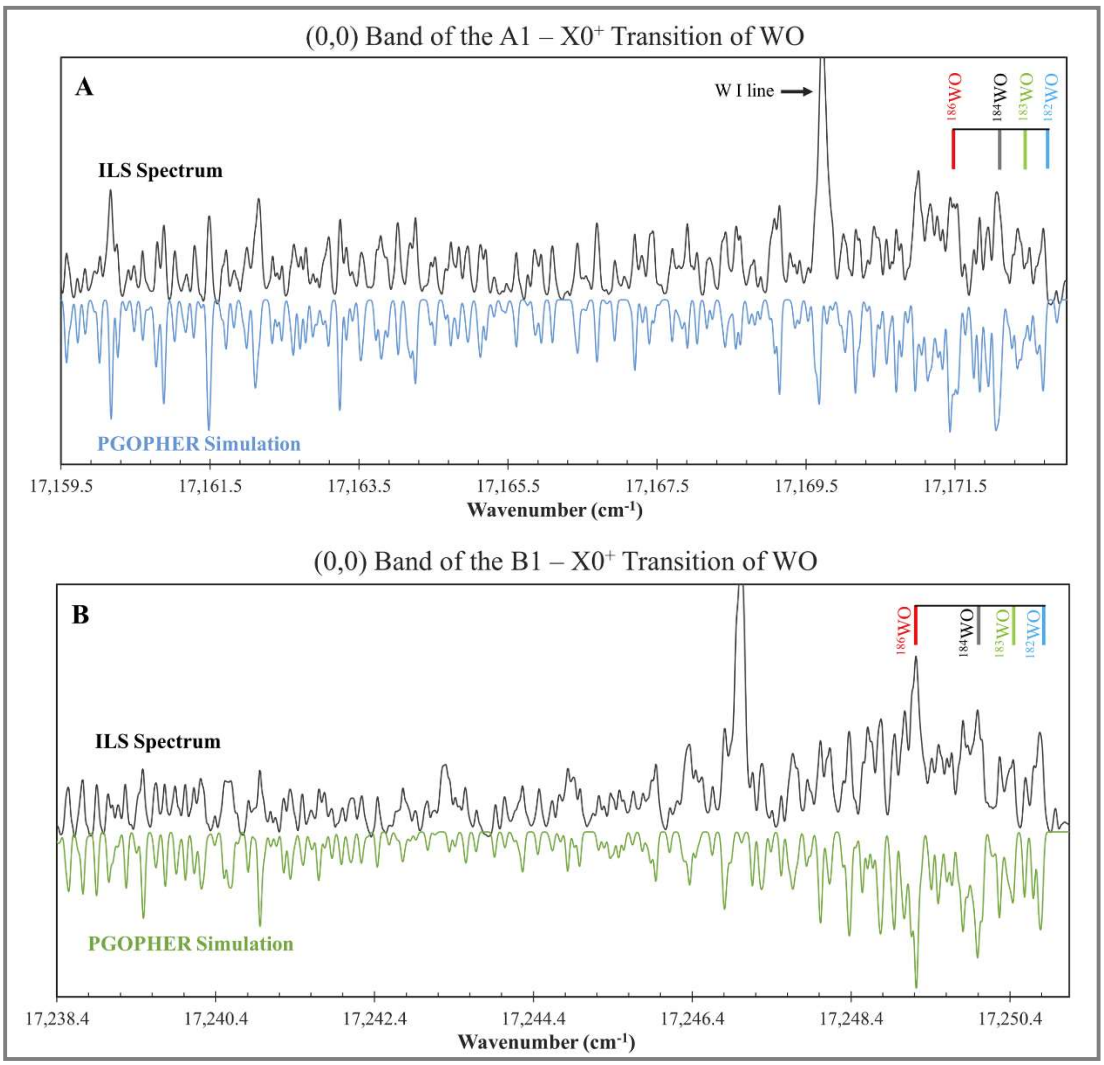

Figure 5.1: Bandhead regions of the (0,0) bands of the WO B1 – $X0^+$ transition (A) and the WO A1 – $X0^+$ transition (B), showing unusual isotope shifts in the bandhead positions. In both panels, the experimental ILS spectrum is shown in black, with the PGOPHER simulation of the final fit directly underneath in blue (A) or green (B). Bandhead positions for each of the four abundant isotopologues are marked in each spectrum.

Observed line positions for all four abundant isotopologues were fit using PGOPHER[8] with a constrained-variables method to maintain expected isotope relationships[2] for each fit parameter. The central ^{184}WO isotopologue was used as a reference with parameters allowed to float in the PGOPHER[8] fit, while constants for the other three isotopologues were calculated from the reference. For each isotopologue, T_0 for the

$X0^+$ ground state was held fixed to 0 cm^{-1}, while the remaining term energy values were constrained to fit using ΔT parameters such that the origin of the reference isotopologue, $T_{v,184}$, was allowed to float, while the remaining term energies were constrained in the same manner as described in Equations 4.13, 4.14, and 4.15. In this way, we maintain expected mass relationships while allowing for deviations in isotope shift related to vibrational frequency and vibrational level. A separate ΔT value was determined for T_1 of the $X0^+$ ground state, and T_0 for each of the A1 and B1 excited states.

Both the A1 and B1 states have $\Omega = 1$ symmetry, which satisfies the requirement of a homogeneous avoided crossing interaction to have $\Delta\Omega=0$. In this type of perturbation, the two involved states effectively "trade places" at J greater than the avoided crossing, with each state taking on the properties (i.e., rotational constants) of the opposing state. The interaction was modeled in PGOPHER[8] using a homogeneous perturbation operator, which required higher-J lines above the avoided crossing to be labeled as the state whose constants were in effect. This means that high-J lines for each A1 transition were re-labeled as lines for the corresponding B1 transition and vice versa. During initial fitting, a section of lines near the J at which crossing was expected was left out of the fit to allow the exact crossing point to be determined by the fitting process. An additional N^2 homogeneous operator was added to introduce a small J-dependence due to the continued observation of systematic and symmetric deviations in the residuals when only the main J-independent homogeneous operator was used. The symmetrized matrix elements are given by <J, Λ=1, Ω=1 || J, Λ=1, Ω=1> = 1 and <J, Λ=1, Ω=1 |N^2| J, Λ=1, Ω=1> = J(J+1) for the J-independent, and J-dependent

operators, respectively. Because there is a relatively small but significant J-dependence to the magnitude of the perturbation, the line positions fit for the A1 and B1 states were limited to those with J-values that were observable in both states. Therefore, because lines for the A1 state were only readily observed to $J' \leq 50$, lines fit for the B1 state were limited to $J' \leq 50$ as well. In the final fit, 1,783 lines were fit to 25 parameters with an average error of 0.006 cm^{-1}. Fit parameters for the three electronic states are given in Table 5.1 and Table 5.2, while the values for the perturbation operators are given in Table 5.3.

Table 5.1: Molecular constants for the X $^3\Sigma^-(0^+)$ state of WO. Uncertainties are given as (1σ). All values are in cm^{-1}.

X $^3\Sigma^-(0^+)$	**^{182}WO**	**^{183}WO**	**^{184}WO**	**^{186}WO**
v = 0				
T_0	0[a]	0[a]	0[a]	0[a]
B_0	0.4159058 (69)	0.4157217 (69)	0.4155399 (69)	0.4151818 (69)
D_0 x 10^6	0.2588 (21)	0.2585 (21)	0.2583 (21)	0.2579 (21)
v = 1				
T_1[b]	1,058.03078 (69)	1,057.80017 (69)	1,057.56957 (69)	1,057.11805 (69)
B_1	0.4138942 (68)	0.4137110 (68)	0.4135301 (68)	0.4131737 (68)
D_1 x 10^6	0.2629 (20)	0.2626 (20)	0.2624 (20)	0.2619 (20)

[a] Held fixed in fit.
[b] The fit ΔT parameter for v = 1 was 0.46121 (41) cm^{-1}.

Table 5.2: Molecular constants for the A1 and B1 states of WO. Uncertainties are given as (1σ). All values are in cm^{-1}.

A1	**^{182}WO**	**^{183}WO**	**^{184}WO**	**^{186}WO**
T_0[a]	17,201.189665 (23)	17,200.534862 (23)	17,199.880060 (23)	17,198.597957 (23)
B_0	0.4036150 (82)	0.4034364 (82)	0.4032599 (82)	0.4029123 (82)
D_0 x 10^6	0.2961 (24)	0.2959 (24)	0.2956 (24)	0.2951 (24)
q x 10^3	0.05487 (97)	0.05482 (97)	0.05477 (97)	0.05468 (97)
B1	**^{182}WO**	**^{183}WO**	**^{184}WO**	**^{186}WO**
T_0[b]	17,207.1683 (12)	17,207.1374 (12)	17,207.1065 (12)	17,207.0460 (12)
B_0	0.3808028 (83)	0.3806343 (83)	0.3804678 (83)	0.3801399 (83)
D_0 x 10^6	0.1449 (25)	0.1447 (25)	0.1446 (25)	0.1444 (25)
q x 10^3	7.5756 (18)	7.5689 (18)	7.5623 (18)	7.5493 (18)
q_D x 10^6	-0.22771 (74)	-0.22741 (74)	-0.22711 (74)	-0.22652 (74)

[a] The fit ΔT parameter for A1 v = 0 was 1.3096 (35) cm^{-1}.
[b] The fit ΔT parameter for B1 v = 0 was 0.0618 (35) cm^{-1}.

Table 5.3: Perturbation operator values for homogeneous and N^2 interactions between WO A1 v=0 and B1 v=0.

	^{182}WO	**^{183}WO**	**^{184}WO**	**^{186}WO**
<A1 v=0||B1 v=0>	38.43895 (55)	38.39163 (60)	38.34692 (51)	38.26011 (61)
<A1 v=0|N^2|B1 v=0>	0.0016587 (14)	0.0016563 (12)	0.0016546 (10)	0.0016483 (13)

5.4 Discussion

This new deperturbation analysis of the (0,0) and (0,1) bands of the A1 – $X0^+$ and B1 – $X0^+$ transitions allows us to look at the two excited states under a new lens. The previous analysis[68] included lines to slightly higher J, but required higher order centrifugal distortion constants to H (for the B1 state) and L (for the A1 state), while this analysis requires only D. In addition, this analysis no longer includes a negative D value for the B1 state, which paradoxically suggests a decrease in the length of the bond with increasing rotational energy. An expected value for D can be estimated using the Kratzer relationship:[6]

$$D_e = \frac{4{B_e}^3}{{\omega_e}^2} \tag{5.1}$$

Using the rotational constant, B, and the vibrational frequency, ω_e, determinations by Ram *et al.*[68] we find an estimated D on the order of 0.25×10^{-6} cm^{-1} for each state. The newly determined values for ^{184}WO of 0.14×10^{-6} cm^{-1} for B1 and 0.30×10^{-6} cm^{-1} for A1 are much more closely aligned with this estimate, reinforcing the viability of the deperturbation analysis. Finally, the values determined for the perturbation interactions are largest for the ^{182}WO isotopologue, with values decreasing slightly with mass, giving ^{186}WO the smallest perturbation value. In the final fit, the unperturbed origins of ^{182}WO A1 and B1 are closest in energy, and thus would be expected to interact slightly more strongly than the other isotopologues.

The constants determined for ^{184}WO from this analysis are compared with those determined previously[66,68] in Table 5.4. Here, we can also see that the constants determined for v = 0 and v = 1 of the $X0^+$ ground state agree rather well, considering the differences in available spectral resolution and fitting methods between 1997, 2009, and 2023, suggesting that discrepancies are in fact due to complexities in the A1 and B1 states. The difference in B values across the three studies is also interesting, as those initially determined by Kuzyakov[66] for A1 and B1 are nearly opposite those determined in this work. While there is no line list available from the earlier determination, it is possible that the lower resolution available from the early spectra led to a reliance on higher-J lines that were more easily distinguished. This could lead to a characterization of the opposite state than that which was intended, since a homogeneous interaction results in higher-J energy levels that exchange characteristics after the avoided crossing.

Our analysis has determined the crossings for each isotopologue occur at $J < 22$, thus if most line positions used in an analysis were of higher J, the determined values would describe the opposing state. This is illustrated in Figure 5.2, which shows a portion of the spectrum for the (0,1) band of the $A1 - X0^+$ transition in which the Q-branch lines go from having characteristics of the A1 state to those of the B1 state. Also visible and marked in the figure are low-J P-branch lines from the A1 state and high-J R-branch lines from what is now labeled as the B1 state. Because all lines in this portion of the spectrum are part of the originally described $A1 - X0^+$ transition band, the spectral lines appear to follow a continuous pattern, concealing the change in apparent parameters. This rationalization can also be applied to the B values determined by Ram *et al.*,[68] since a mixture of low and moderate J observations would result in an "averaging out" of the B values for the two states, resulting in very similar values for B for A1 and B1, and higher J lines fit through the use of many higher-order centrifugal distortion constants, as we see in the parameters from that study.

Table 5.4: Comparison of rotational constants for the $X0^+$, A1, and B1 states of ^{184}WO determined initially by Ref [66], by Ref [67], and by this work. Uncertainties are given as (1σ). All values are in cm^{-1}.

X $^3\Sigma^-(0^+)$	Ref [66]	Ref [67]	This Work
B_0	0.4153 (5)	0.4155370 (54)	0.4155399 (69)
D_0 x 10^6	0.261 (8)	0.2554 (15)	0.2583 (21)
B_1	0.4135 (5)	0.4135229 (53)	0.4135301 (68)
D_1 x 10^6	-	0.2570 (14)	0.2624 (20)
A1	Ref [66]	Ref [67]	This Work
T_0	-	17,164.9641 (14)	17,199.880060 (23)
B_0	0.38733 (15) / 0.38181 (15)[a]	0.3913397 (73)	0.4032599 (82)
D_0 x 10^6	0.270 (6) / 0.264 (9)[a]	2.1370 (60)	0.2956 (24)
H_0 x 10^{10}	-	1.881 (24)	-
L_0 x 10^{13}	-	-0.0660 (32)	-
q x 10^3	-	3.4260 (57)	0.05477 (97)
q_D x 10^6	-	1.1384 (85)	-
q_H x 10^9	-	-0.1876 (39)	-
q_L x 10^{13}	-	0.0960 (55)	-
B1	Ref [66]	Ref [67]	This Work
T_0	-	17,242.0010 (14)	17,207.1065 (12)
B_0	0.4013 (5)	0.3923935 (84)	0.3804678 (83)
D_0 x 10^6	-	-1.6677 (88)	0.1446 (25)
H_0 x 10^{10}	-	-1.593 (34)	-
q x 10^3	-	4.1865 (81)	7.5623 (18)
q_D x 10^6	-	-1.334 (14)	-0.22711 (74)
q_H x 10^9	-	0.1521 (62)	-

[a] Ref [66] assigned the current (0,1) band as (0,0), and the current (0,0) band as (1,0), and thus unknowingly reported two sets of constants for the same vibrational level.

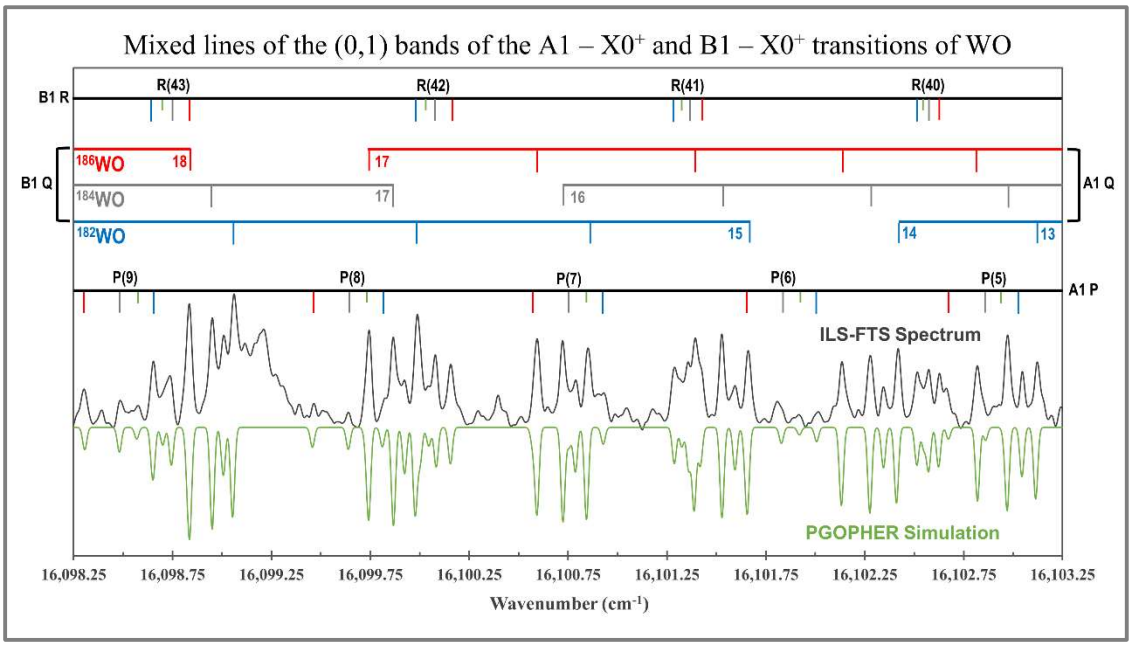

Figure 5.2: A portion of the A1 – $X0^+$ transition of WO, showing the region of the Q-branch where the rotational characteristics of the A1 state transition to those of the B1 state, though there does not appear to be any discontinuity in the spectrum. Low-J lines of the A1 P-branch and high-J lines of the B1 R-branch are also visible and marked. For clarity, the lines for the ^{183}WO isotopologue are not marked in the Q-branch, but are marked in green for the P- and R-branches. Lines for ^{182}WO are marked with blue, ^{184}WO are marked with gray, and ^{186}WO are marked with red.

The magnitudes of the ΔT parameters determined for the A1 and B1 states are also worth noting, since the discrepancy in vibrational assignments for the A1 transition are due largely to abnormal isotopic shifts. The ΔT of 1.3 cm^{-1} in the A1 state is more closely aligned with the v = 3 assignment originally given by Weltner and McLeod,[64] who made that determination based not on the separation between the ^{182}WO-^{184}WO-^{186}WO isotopologues, but on the distance between bands of the W^{16}O and W^{18}O isotopologues. A subsequent analysis[67] did not find evidence of lower vibrational levels of the A1 state where they were expected, leading to the change in vibrational assignment to the currently accepted v = 0. This deperturbation analysis gives a significantly different term energy for the v = 0 level, which may suggest that a fresh

look at previously determined vibrational parameters is warranted. It is also possible, however, that the odd behavior of the isotopic shifts is due to interaction with yet another perturbing state.

5.5 Conclusions

This deperturbation analysis of the A1 and B1 states of WO has produced a set of constants for v = 0 of each state that not only incorporates all four abundant isotopologues using a mass-constrained fit, but also significantly reduces the number of parameters required to describe each of the states. The new centrifugal distortion constants are also much more closely aligned with the expected values derived from the Kratzer relationship.[6] This work supports decades of supposition that the two states interact and gives a deeper insight into the tangled web of excited electronic states found in this complex molecule, though a full understanding remains elusive.

References

1. S.J. Ling, J. Sanny, W. Moebs. *University Physics Volume 3*. OpenStax. Houston, TX, 2016. https://openstax.org/books/university-physics-volume-3/pages/9-2-molecular-spectra (Accessed 7/26/23)
2. G. Herzberg. *Spectra of Diatomic Molecules*, 2nd ed., D. Van Nostrand Company, New York, NY, 1950.
3. T. Engel. *Quantum Chemistry & Spectroscopy*, 3rd Ed.: Pearson Education, Inc., London, England, 2012.
4. P.F. Bernath. *Spectra of Atoms and Molecules*, 3rd Ed.; Oxford University Press: New York, NY, 2016.
5. J. L. Dunham. The energy levels of a rotating vibrator. *Phys. Rev.* **41** (1932) 721–731.
6. H. Lefebvre-Brion, R.W. Field. Perturbations in the Spectra of Diatomic Molecules; Elsevier, 1986.
7. K.S.E. Eikema, W. Hogervorst, W. Ubachs. On the determination of a heterogeneous vs a homogeneous perturbation in the spectrum of a diatomic molecule: the K $^1\Sigma^+$, v=0 state of $^{13}C^{18}O$. *J. Mol. Spectrosc.***163** (1994) 19-26.
8. C. M. Western, PGOPHER, A Program for Simulating Rotational, Vibrational and Electronic Spectra. *JQSRT* **186** (2017) 221–242. doi:10.1016/j.jqsrt.2016.04.010. (version 11.0.141.0).
9. A.A. Breier, B. Waßmuth, T. Büchling, G.W. Fuchs, J. Gauss, T.F. Giesen. A mass-independent expanded Dunham analysis of aluminum monoxide and aluminum monosulfide. *J. Mol. Spectrosc.* **350** (2018) 43-50.
10. L.A. Pakhomycheva, E.A. Sviridenkov, A.F. Suchkov, L.V. Titova, S.S. Churilov. Line structure of generation spectra of lasers with inhomogenous broadening of the amplification line. *ZhETF Pis.* **12** (1970) 60–63.
11. V.M. Baev, T. Latz, P.E. Toschek. Laser intracavity absorption spectroscopy. *Appl. Phys. B.* **69** (1999) 171–202.
12. K. Singh and J.J. O'Brien. Laboratory measurements of absorption coefficients for the 727 nm band of methane at 77 K and comparison with results derived from spectra of the giant planets. *J. Quant. Spectrosc. Radiat. Transfer*. **54** (1995) 607–619.
13. A. Thompson and B.N. Taylor. *NIST Special Publication 811: Guide for the Use of the International System of Units, 2008 Ed.* [Online] National Institute of Standards and Technology, U.S. Department of Commerce; p. 27. https://physics.nist.gov/cuu/pdf/sp811.pdf (Accessed 12/9/2020).
14. F. Stoeckel, M.A. Melieres, M. Chenevier. Quantitative measurements of very weak H_2O absorption lines by time resolved intracavity laser spectroscopy. *J. Chem. Phys.* **76** (1982) 2191–2196.
15. M. Chenevier, M.A. Melieres, F. Stoeckel. Intracavity absorption line shapes and quantitative measurements on O_2. *Opt. Commun.* **45** (1983) 385–391.

16. A. Campargue, F. Stoeckel, M. Chenevier. High sensitivity intracavity laser spectroscopy: applications to the study of overtone transitions in the visible range. *Spectrochimica Acta. Rev.* **13** (1990) 69–88.

17. F. Stoeckel, G.H. Atkinson. Time evolution of a broadband quasi-cw dye laser: Limitations of sensitivity in intracavity laser spectroscopy. *Appl. Opt.* **24** (1985) 3591-3597.

18. S. Kuldip; J.J. O'Brien. Measurement of pressure-broadening and lineshift coefficients at 77 and 296 K of methane lines in the 727 nm band using intracavity laser spectroscopy. *JQSRT* **52** (1994) 75–87.

19. J.J. O'Brien, H. Cao. Absorption spectra and absorption coefficients for methane in the 750 – 940 nm region obtained by intracavity laser spectroscopy. *JQSRT* **75** (2002) 323-350.

20. L.C. O'Brien, J.C. Harms, J.J. O'Brien. W. Zou. Analysis of the $A\ \Omega=1 - X\ ^3\Sigma^-(0^+)$ transition of PtS observed by intracavity laser spectroscopy with fourier transform detection (ILS-FTS), and computational studies of electronic states of PtS. *J. Mol. Struct.* **1211** (2020) 128024.

21. E.N. Antonov, A.A. Kachanov, V.R. Mironenko, T.V. Plakhotnik. Dependence of the sensitivity of intracavity laser spectroscopy on generation parameters. *Opt. Commun.* **46** (1983) 126-130.

22. E.N. Antonov, P.S. Antsyferov, A.A. Kachanov, V.G. Koloshnikov. Parasitic selection in intracavity laser detection spectroscopy. *Opt. Commun.* **41** (1982) 131-134.

23. S.J. Harris. Intracavity laser spectroscopy: An old field with new prospects for combustion diagnostics. *Appl. Opt.* **23** (1984) 1311-1318.

24. G.O. Brink. Dye laser intracavity absorption for molecular spectroscopy. *J. Mol. Spectrosc.* **90** (1981) 533-358.

25. J.C. Harms, E.M. Grames, S. Han, L.C. O'Brien, J.J. O'Brien. Identification of two new excited electronic states of NiCl: Analyses of the (1,0) & (0,0) bands of the [13.5] $^2\Phi_{7/2}$ – [0.16] $A\ ^2\Delta_{5/2}$ and (0,0) band of the [13.8] $^2\Pi_{1/2}$ – [0.38] $X\ ^2\Pi_{1/2}$ transitions. *J. Mol. Spectrosc.* **333** (2017) 36-41.

26. J.C. Harms, J.J. O'Brien, L.C. O'Brien. The spin-forbidden $a\ ^4\Sigma^-$–X $^2\Pi_{1/2}$ transition of GeH detected in absorption using intracavity laser spectroscopy. *J. Chem. Phys.* **148** (2018) 204306.

27. J.C. Harms, L.C. O'Brien, J.J. O'Brien. Rotational analysis of the [15.1] $A'' - \tilde{X}\ ^1A'$ transition of CuOH and CuOD observed at high resolution with intracavity laser spectroscopy. *J. Mol. Spectrosc.* **362** (2019) 8-13.

28. J.C. Harms, E.M. Grames, S. Yun, B. Ahmed, L.C. O'Brien, J.J. O'Brien. Mass-independent Dunham analysis of the [7.7] $Y\ ^2\Sigma^+ - X\ ^2\Pi_i$ and [16.3] $A\ ^2\Sigma^- - X\ ^2\Pi_i$ transitions of copper monoxide, CuO. *J. Mol. Spectrosc.* **363** (2019) 111173.

29. E. Tiemann, H. Knöckel, and J. Schlembach. Influence of the finite nuclear size on the electronic and rotational energy of diatomic molecules. *Ber. Bunsenges. Phys. Chem.* **86(9)** (1982) 821-824.

30. H. Knöckel and E. Tiemann. Isotopic field shift in the transition A 0^+ – X $^1\Sigma^+$ of PbS. *Chem. Phys*. **68** (1982) 13-19.

31. J. Schlembach and E. Tiemann. Isotopic field shift of the rotational energy of the Pb-chalcogenides and Tl-halides *Chem. Phys.*, **68** (1982) 21-28.

32. H. Knöckel, T. Kröcketskothen, and E. Tiemann. Molecular-beam-laser studies of the states $X\ ^1\Sigma^+$ and $A0^+$ of PbS. *Chem. Phys.*, **93** (1985) 349-358.

33. H. Knöckel, U. Lindner, and E. Tiemann. High resolution laser excitation spectroscopy of the $B1 - X\ ^1\Sigma^+$ transition of PbS. *Mol. Phys.* **61** (1987) 351-358.

34. R.J. Le Roy. Improved Parameterization for Combined Isotopomer Analysis of Diatomic Spectra and Its Application to HF and DF *J. Mol. Spec*. **194** (1999) 189-196.

35. J.C. Harms, L.C. O'Brien, J.J. O'Brien. Identification and characterization of two new electronic states of PtF: Analysis of the (2,1), (1,0), (0,0), (0,1), (1,2), and (0,2) bands of the $[15.8 + x]\ \Omega = 5/2 - B\ ^2\Delta_{5/2}$ transition. *J. Mol. Spec*. **35** (2019) 101-108.

36. J.C. Harms, L.C. O'Brien, J.J. O'Brien. Mass-independent Dunham analysis of the known electronic states of platinum sulfide, PtS, and analysis of the electronic field-shift effect. *J. Chem. Phys.* **151(9)** (2019) 094303.

37. J.C. Harms, J. Wu, S. Mian, L.C. O'Brien, J.J. O'Brien. Mass-independent Dunham analysis of the $[13.8]\ \Omega = 3/2 - X\ ^2\Pi_{3/2}$ transition of platinum monochloride, PtCl, observed by intracavity laser spectroscopy: Periodic trends in the M^+X^- bonding model (M = Ni, Pt; X = F, Cl). *J. Mol. Spectrosc.* **359** (2019) 6-15.

38. K.F. Ng, W. Zou, W. Liu, A.S.-C. Cheung. Electronic transitions of tantalum monofluoride. *J. Chem. Phys*. **146** (2017) 094308.

39. L.F. Tsang, M.-C. Chan, W. Zou, A.S.-C. Cheung. Electronic transitions of tungsten monosulfide. *J. Mol. Spectrosc*. **359** (2019) 31.

40. A. Charvát, A.A. Kachanov, A. Campargue, D. Permogorov, F. Stoeckel. High sensitivity intracavity absorption spectroscopy of CHD_3 in the near infrared with a titanium:sapphire laser. *Chem. Phys. Lett.* **214** (1993) 495–501.

41. H. Salami, A.J. Ross. A molecular iodine atlas in ascii format. *J. Mol. Spectrosc*. **223** (2005) 157–159.

42. J.C. Harms. High resolution near-infrared/visible Intracavity Laser Spectroscopy of small molecules (2019). Dissertations. 816. https://irl.umsl.edu/dissertation/816

43. I.E. Gordon, L.S. Rothman, C. Hill, *et al.* The HITRAN2016 molecular spectroscopic database. *JQSRT* **203** (2017) 3–69.

44. F. Kerber, G. Nave, and C.J. Sansonetti. The spectrum of Th-Ar hollow cathode lamps in the 691-5804 nm region: Establishing wavelength standards for the calibration of infrared spectrographs. Astrophys. *J., Suppl. Ser.* **178** (2008) 374–381.

45. C. Lovis and F. Pepe. A new list of thorium and argon spectral lines in the visible. *Astron. Astrophys.* **468** (2007) 1115–1121.

46. K.N. Bales, J.C. Harms, L.C. O'Brien, J.J. O'Brien. Identification of two new electronic transitions of TaF using intracavity laser spectroscopy. *J. Mol. Spectrosc.* **365** (2019) 111208.

47. B. Grovem, M. Heyne, A.N. Mehta, H. Bender, T. Nuytten, J. Meersschaut, T. Conard, P. Verdonck, S. Van Elshocht, W. Vandervorst, S. De Gendt, M. Heyns, I. Radu, M. Caymax,

and A. Delabie. Plasma-enhanced atomic layer deposition of two-dimensional WS_2 from WF_6, H_2 Plasma, and H_2S *Chem. Mater*. **29** (2017) 2927-2938.

48. M.K.S. Bin Rafiq, N. Amin, H.F. Alharbi, M. Luqman, A. Ayob, Y. S. Alharthi, N.H. Alharthi, B. Bais, and M. Akhtaruzzaman. WS_2: A new window layer material for solar cell application. *Sci. Rep.* **10** (2020) 771.

49. B. Liang and L. Andrews, J. Infrared spectra and density functional theory calculations of group 6 transition metal sulfides in solid argon. *Phys. Chem. A.* **106** (2002) 6945-6951.

50. A. Sevy, R.F. Huffaker, M.D. Morse. Bond dissociation energies of tungsten molecules: WC, WSi, WS, WSe, and WCl. *J. Phys. Chem. A*. **121** (2017) 9446–9457.

51. K.N. Bales, J.C. Harms, L.C. O'Brien, and J.J. O'Brien. Talk WJ05, 74th International Symposium on Molecular Spectroscopy (2019) (http://hdl.handle.net/2142/104311). 10.15278/isms.2019.WJ05.

52. J. Zhang, F. Fang, L. Zhang, D. Zhao, X. Ma, J. Yang. Spin-orbit splitting in the ground state of tungsten monosulfide. *J. Mol. Spectrosc*. **366** (2019) 111223.

53. J.C. Harms, B.M. Ratay, K.N. Bales, J.J. O'Brien, L.C. O'Brien. Intracavity laser spectroscopy with Fourier-transform detection of tungsten sulfide, WS: Analysis of the (1,0) band of the [13.10] $\Omega = 1 - X\ ^3\Sigma^-0^+$ transition. *J. Mol. Spectrosc*. **372** (2019) 111349.

54. J.C. Harms, K.N. Bales, J.J. O'Brien, L.C. O'Brien. Observation and analysis of a new $[14.26]0^+ - X\ ^3\Sigma^-0^+$ transition of WS, observed using intracavity laser spectroscopy with Fourier-transform detection. *J. Mol. Spectrosc.* **374** (2020) 111378.

55. J. Zhang, W. Zou, L. Zhang, D. Zhao, X. Ma, J. Yang. The electronic structure of WS molecule below 21,500 cm^{-1}. *JQSRT* **256** (2020) 107314.

56. K.N. Bales, J.C. Harms, J.J. O'Brien, L.C. O'Brien. Analysis of the newly observed $[15.05]0^+ - X\ ^3\Sigma^-(0^+)$ transition of WS observed using intracavity laser spectroscopy with Fourier-transform detection. *J. Mol. Spectrosc.* **377** (2021) 111430.

57. K.N. Bales, J.C. Harms, J.J. O'Brien, L.C. O'Brien. Rotational and deperturbation analysis of the (0,0) and (1,0) vibrational bands of the $[15.30]1 - X\ ^3\Sigma^-(0^+)$ transition of WS. *J. Mol. Spectrosc.* **389**, (2022) 111702.

58. J.M. Brown, E.A. Colburn, J.K.G. Watson, F.D. Wayne. An effective Hamiltonian for diatomic molecules: Ab initio calculations of parameters of HCl^+. *J. Mol. Spectrosc*. **74** (1979) 294-318.

59. H. Lefebvre-Brion, R.W. Field, *Perturbations in the Spectra of Diatomic Molecules*, Elsevier, 1986.

60. Kramida, A., Ralchenko, Yu., Reader, J., and NIST ASD Team (2022). NIST Atomic Spectra Database (ver. 5.10), [Online]. Available: https://physics.nist.gov/asd [2023, May 18]. National Institute of Standards and Technology, Gaithersburg, MD. DOI: https://doi.org/10.18434/T4W30F

61. S.K. Deb. Opportunities and challenges in science and technology of WO_3 for electrochromic and related applications. *Sol. Energy Mater. Sol. Cells.* **92** (2008) 245-258.

62. H. Zheng, J.Z. Ou, M.S. Strano, R.B. Kaner, A. Mitchell, K. Kalantar-Zadeh. Nanostructured tungsten oxide–Properties, synthesis, and applications. *Adv. Funct. Mater.* **21** (2011) 2175–2196.

63. P. Thi Hong Van, N. Hoang Thanh, V. Van Quang, N. Van Duy, N. Duc Hoa, N. Van Hieu. Scalable fabrication of high-performance NO2 gas sensors based on tungsten oxide nanowires by on-chip growth and RuO2-functionalization. *ACS Appl. Mater. Interfaces*. **6 (**2014) 12022–12030.

64. W. Weltner, D. McLeod. Spectroscopy of tungsten oxide molecules in neon and argon matrices at 4° and 20°K. *J. Mol. Spectrosc.* **17** (1965) 276-299.

65. A.N. Samoilova, Yu.M. Efremov, L.V. Gurvich. Electronic spectrum of the $^{186}W^{16}O$ molecule. *J. Mol. Spectrosc.* **17** (1981) 1-15.

66. Yu. Ya. Kuzyakov, E.N. Moskvitina, E.N. Filippova. Intracavity electronic absorption spectra of MoO and WO molecules in the visible region. *Spectroscopy Lett.* **30(6)**, (1997) 1057-1066.

67. R. Ram, J. Liévin, G. Li, T. Hirao, and P.F. Bernath. The X $^3\Sigma^-$ ground state of WO. *Chem. Phys. Lett.* **343** (2001) 437-445.

68. R. Ram, J. Liévin, and P.F. Bernath. Fourier transform emission spectroscopy and *ab initio* calculations on WO. *J. Mol. Spectrosc.* **256** (2009) 216.